

MAGNETIC FORCE MICROSCOPY STUDIES OF
UNCONVENTIONAL SUPERCONDUCTORS:
SINGLE VORTEX MANIPULATION AND MAGNETIC
PENETRATION DEPTH MEASUREMENTS

A DISSERTATION
SUBMITTED TO THE DEPARTMENT OF PHYSICS
AND THE COMMITTEE ON GRADUATE STUDIES
OF STANFORD UNIVERSITY
IN PARTIAL FULFILLMENT OF THE REQUIREMENTS
FOR THE DEGREE OF
DOCTOR OF PHILOSOPHY

Lan Luan
March 2011

Preface/Abstract

Superconductivity is among the most fascinating properties that a material can have. Below the transition temperature T_c , electrons condensate into a macroscopic quantum mechanical state and flow without dissipation. The quantum nature of the superconducting state also manifests in its magnetic properties. Superconductors fully expels magnetic field in a weak applied field, referred as Meissner effect. In an intermediate field, superconductors often contain microscopic whirlpools of electrons that carry quantized magnetic flux, called vortices. In this thesis, I present magnetic-force-microscopy (MFM) studies of unconventional superconductors both in the Meissner state and in the mix state. We extend the application of MFM beyond the conventional imaging mode and use it for quantitative analysis. In the mix state, we use MFM manipulating individual vortices with a high level of control and a known force to study the mechanics and dynamics of a single vortex in cuprate superconductors. In the Meissner state, we establish MFM as a novel local technique to measure the magnetic penetration depth λ and implement it to study the pairing mechanism of iron-pnictide superconductors.

Chapter 1 contains a brief introduction of MFM and its conventional application of imaging. We demonstrate high-spatial resolution images of isolated superconducting vortices. We show that by integrating images of isolated vortices at consecutive heights we are able to reconstruct the force between the MFM tip and vortices. We can also obtain the force by using a tip-vortex model. The two methods agree and both allow us to obtain the force used in vortex manipulation discussed in Chapter 2 and Chapter 3.

Chapter 2 discusses the behavior of individual vortices in fully doped $\text{YBa}_2\text{Cu}_3\text{O}_{7-\delta}$

when subject to a local force. Because the anisotropy of fully doped $\text{YBa}_2\text{Cu}_3\text{O}_{7-\delta}$ is moderate, the vortex motion can be well described as an elastic string moving through a uniform three dimensional pinning landscape. We find an unexpected and marked enhancement of the response of a vortex to pulling when we wiggle it transversely. In addition, we find enhanced vortex pinning anisotropy that suggests clustering of oxygen vacancies in our sample. We demonstrate manipulation at the nanoscale with a level of control far beyond what has been reported before. We show that a dragged vortex can be used to probe deep into the bulk of the sample and to interact with microscopic structures much smaller than the tip size.

Chapter 3 shows the vortex behavior in another limit. In an very underdoped $\text{YBa}_2\text{Cu}_3\text{O}_{6+x}$ single crystal, a cuprate superconductor with strong anisotropy, a vortex can be regarded as a stack of two-dimensional pancakes with weak interlayer Josephson coupling. We use the MFM tip to split the pancake stacks composing a single vortex and to produce a kinked structure. Our measurements highlight the discrete nature of stacks of pancake vortices in layered superconductors. We also measure the required force in the process, providing the first measurement of the interlayer coupling at the single vortex level.

The discovery of iron-pnictide superconductors in 2008 motivates my efforts to locally measure the magnetic penetration depth λ , one of the two fundamental length scales in superconductors and known to be difficult to measure. Chapter 4 discusses the methodology of measuring λ by MFM, which is based on the time-reversed mirror approximation and an analytical model of the MFM tip-superconductor interaction in the Meissner state. A calibration run was performed on $\text{YBa}_2\text{Cu}_3\text{O}_{6+x}$ single crystals with known λ . The same time-reversed mirror approximation can be applied to scanning SQUID susceptometry (SSS) to measure the temperature variation of penetration depth $\Delta\lambda(T) \equiv \lambda(T) - \lambda(0)$.

Chapter 5 includes brief introduction of the iron-pnictide superconductors. The multiple conduction bands and the vicinity of the superconducting phase to magnetic phase give additional challenges in λ measurements. We demonstrated in this chapter on single crystals of $\text{Ba}(\text{Fe}_{0.95}\text{Co}_{0.05})_2\text{As}_2$ that MFM can measure the absolute value of λ , as well as obtain its temperature dependence and spatial homogeneity. We observe

that $\Delta\lambda(T)$ varies 20 times slower with temperature than previously reported by bulk techniques, and that $\rho_s(T)$ over the full temperature range is well described by a clean two-band fully gapped model, consistent with the proposed $s\pm$ pairing symmetry.

Chapter 6 extends the measurements of $\rho_s(T)$ to the family $\text{Ba}(\text{Fe}_{1-x}\text{Co}_x)_2\text{As}_2$ with Co doping level x across the superconducting dome. We observe systematic evolution of $\rho_s(T)$ with x that can be summarized as three main trends. First, $\rho_s(0)$ falls more quickly with T_c on the underdoped side of the dome than on the overdoped. Second, the temperature variation of $\rho_s(T)$ at low temperature increases away from optimal doping. Third, $\rho_s(T)$ increases sharply with cooling through the superconducting transition temperature T_c of both optimally doped and underdoped compounds. These observations hint an interplay between magnetism and superconductivity.

Acknowledgement

First of all, I would like to thank my advisor Kam for her insightful and valuable scientific guidance, for the tremendous trust and encouragement she gave, and for the independence and confidence she managed to build in me throughout my years of graduate school. She has been a role model for me not only as a great physicist, but also as a very considerate, open-minded person and leader. She always puts my education and career development the highest priority. It has been a real pleasure working with her.

I can hardly imagine to have better colleagues than what I have been having in Moler lab. Besides enjoying the friendship with them, I would like to especially thank the senior graduate students and postdocs in the lab during my junior years in helping my scientific development. Ophir Auslaender taught me MFM, lead me to the studies of single vortex mechanics and showed me how to carry out research projects through daily interaction over the three years we shared the same instrument. I would not have been able to carry out the research reported in this thesis without the extensive knowledge and experience I inherited from him. Cliff Hicks initiated the studies of the pnictide, which motivated my effort on establishing MFM as a new technique to measure the penetration depth. He gave me the first introductory lecture on the pnictides, and constantly brought in thoughtful comments. Hendrik Bluhm is full of passion and ideas, and always offers valuable help in almost all aspects. I also enjoyed so many late-night conversations with him especially in my struggling time of graduate school.

I would like to thank Tom Lippman, Julie Bert and Beena Kalisky for their help in running SQUID scanning systems; and Nick Koshnick, Zhifeng Deng, Lisa Qian,

Anand Natarajan and Hanshen Zhang for their help and support. It was very fortunate for me to have great predecessors on the MFM project: Eric Straver took all the credit for building such reliable instrument, which served me very well in the past five years. His thesis, and the very informative manual Jenny Hoffman wrote, were great resources for me.

I would like to thank my collaborators. It was a great pleasant to work with John Kirtley on a few modeling projects. I wish I had more opportunities to work with him and learn from him. The YBCO single crystals studied in this thesis were provided by Doug Bonn, Ruixing Liang and Warter Hardy at University of British Columbia. The work would have been impossible without such pristine crystals. The pnictide projects were in close collaboration with Jiun-Haw Chu, James Analytis and Ian Fisher at Stanford. They not only made great efforts in providing us high-quality crystals in a timely manner, but also contributed significantly to the physics.

Finally, I would like to thank my family. It was my parents emphasis on education, motivation and persistence that brought me to Stanford and encouraged me to march through the Ph.D program. I feel really lucky having my husband Chong Xie on the same journey of graduate school. He shared my up and downs and always held my hands tight especially in the dark time. His enthusiasm in science and engineering provides me with more inspiration and motivation. He also always encourages me to look for the best opportunities for myself even if it means he has to sacrifice. I am really thankful for all of his support.

Contents

Preface/Abstract	v
Acknowledgement	viii
1 Introduction of magnetic force microscopy	1
1.1 Fundamentals of magnetic force microscopy	1
1.2 Brief Instrumentation	4
1.2.1 Two imaging modes of MFM	4
1.2.2 Scanner calibration	6
1.3 Applications of MFM imaging	7
1.3.1 Imaging individual superconducting vortices	8
1.3.2 Two approaches of force reconstruction from vortex images . .	11
1.3.3 Simultaneous MFM and electric force microscopy	13
2 Mechanics of individual vortices in a cuprate superconductor $\text{YBa}_2\text{Cu}_3\text{O}_{7-\delta}$ with moderate anisotropy	15
2.1 Introduction	16
2.2 Experiments and discussions	17
2.2.1 Wiggling effect along the slow scan direction	17
2.2.2 Exponential T dependence of the depinning force	19
2.2.3 Force and direction dependence dragging along the fast scan direction	22
2.3 Conclusion	32

3	Magnetic force microscopy study of interlayer kinks in individual vortices in the underdoped cuprate superconductor $\text{YBa}_2\text{Cu}_3\text{O}_{6+x}$	34
3.1	Introduction	34
3.2	Sample and technique	37
3.3	Experiment and discussion	38
3.4	Conclusions	44
4	Determining the penetration depth λ by Meissner repulsion	46
4.1	Introduction	46
4.2	Sample and technique	47
4.3	Model the Meissner response	48
4.3.1	Truncated cone model	49
4.4	Results and error analysis	50
4.5	Additional discussions of the model	54
4.5.1	Sharp cone model	54
4.5.2	Other approximations of the truncated cone model	55
4.5.3	Possible future improvement	57
4.6	Time-reversed mirror approximation	57
4.6.1	$\Delta\lambda$ measurements by MFM and scanning SQUID susceptometry	57
4.6.2	Errors at large λ limit	58
4.6.3	Validity in fully anisotropic materials	59
4.6.4	λ_c mixing in in the presence of topography	60
4.7	Estimate λ by imaging individual vortices	61
5	Local measurement of the penetration depth in the pnictide superconductor $\text{Ba}(\text{Fe}_{0.95}\text{Co}_{0.05})_2\text{As}_2$	64
5.1	Brief introduction of iron-pnictide superconductors	65
5.2	Measurement of $\rho_s(T)$ in $\text{Ba}(\text{Fe}_{0.95}\text{Co}_{0.05})_2\text{As}_2$	69
5.3	Vortex images as quantitative measure of $\rho_s(T)$ inhomogeneity	74
5.4	Conclusion	76

6	Local measurement of the superfluid density in the pnictide superconductor $\text{Ba}(\text{Fe}_{1-x}\text{Co}_x)_2\text{As}_2$ across the superconducting dome	78
6.1	Introduction	79
6.2	Experiments: three observations	80
6.3	Spatial and sample variation in $\Delta\lambda$	84
6.4	Discussion	86
6.5	Speculations	88
6.5.1	$\rho_s(0)$ of cuprates and pnictides	88
6.5.2	Disparity of gap structures in the pnictides	90

List of Tables

1.1	Sensitivities and spatial resolutions of MFM, scanning SQUID microscopy (SSM) and scanning Hall microscopy (SHM) when the field source is spin (dipole), magnetic flux (monopole) and line of current. We assume $z = 15$ nm for MFM and z is 0.1 of sensor size for SSM and SHM.	4
1.2	Calibration values for the piezotubes at various temperature. Also listed is the time till when the tubes were used. x and y here denote to the fast scan direction and slow scan direction respectively.	7
1.3	cantilever parameters	13
4.1	reference of λ measurements in $\text{YBa}_2\text{Cu}_3\text{O}_{6+x}$ ($x \approx 0.56$) ortho-II de-twinning crystals	48
5.1	The literature on penetration depth measurement taken on single-crystal pnictide superconductors before Sep. 2009.	69
6.1	Fit parameters for curves in Fig. 6.1 and 6.4, for the two-gap (Eq. 2) and power-law (Eq. 3) models.	83
6.2	$\rho_s(0)$ of $\text{Ba}(\text{Fe}_{1-x}\text{Co}_x)_2\text{As}_2$, $\text{YBa}_2\text{Cu}_3\text{O}_{6+x}$ and $\text{La}_{2-x}\text{Sr}_x\text{CuO}_4$	89
6.3	The up-to-date literature on penetration depth measurement taken on single-crystal pnictide superconductors	91

List of Figures

1.1	The microscope head	5
1.2	Field cooled vortices in a $\text{YBa}_2\text{Cu}_3\text{O}_{7-\delta}$ (YBCO) single crystal (fully doped, $T_c = 88$ K) at $T = 6$ K (A), and the Fourier transform of the vortex locations (B), from which we identify the crystal axes and obtain the in-plane anisotropy.	9
1.3	The flux front structure in the fully doped YBCO single crystal at $T = 5$ K.	10
1.4	An example of force reconstruction for the fully doped $\text{YBa}_2\text{Cu}_3\text{O}_{7-\delta}$ (YBCO) single crystal	12
1.5	$\partial F_z/\partial z$ as a function of tip-sample voltage V_{dr} at height $z = 80$ nm. The value of V_{dr} that minimized $\partial F_z/\partial z$ gives the contact potential difference between the tip and the sample. Data taken on the fully YBCO single crystal.	14
2.1	MFM imaging and manipulation of individual vortices in fully doped YBCO at $T = 22.3$ K	18
2.2	MFM image and line scans at $T = 20$ K, showing how wiggling enhances dragging along the slow direction.	20
2.3	Test of transverse agitation at $T = 20$ K	21
2.4	Distribution and the mean value of the depinning forces, F_0 , vs. temperature T	23
2.5	Extracting the dragging distance w at an arbitrary scan angle φ	24
2.6	Force dependence of the dragged distance, w , along the fast axis.	25

2.7	Cartoon showing crystal axes, vortex axis, the clusters and the angles used in the equations, θ and φ	27
2.8	Images and analysis showing the anisotropy of dragging when the fast axis is along the a axis and when it is along the b axis.	29
2.9	Distance moved, w , measured at the maximum lateral force, versus scan angle φ	31
3.1	MFM images on strongly underdoped YBCO single crystal showing the annihilation and creation of kinked stacks of pancake vortices, which appear as pairs of sub- Φ_0 , isolated features.	36
3.2	Scans (a,c) and fits (b,d) of vortices before and after manipulation.	40
3.3	Creating kinks from a straight stack.	42
3.4	Calibration of the tip to extract $F_{lat}^{max}(z)$, the maximum lateral force exerted on a vortex during a scan at height z	43
4.1	Measuring λ and $\Delta\lambda$ by MFM in the Meissner state using time-reversed mirror approximation.	51
4.2	The fit quality of the truncated cone model and SEM images of the MFM tips used in the measurement.	52
4.3	The time reversed mirror approximation for MFM and Scanning SQUID, using which we measure $\Delta\lambda$ independent of modeling.	58
4.4	The estimated error in $\Delta\lambda$ from time-reversed mirror approximation	59
4.5	Extracting an estimate of λ from images of individual vortices.	63
5.1	Crystallographic (a) and magnetic structures (b) of the iron-base superconductors.	65
5.2	Experimental phase diagrams of the BaFe ₂ As ₂ system (a) and fluorine-doped 1111 system (b)	67
5.3	The Fermi surface structure and superconducting OP symmetry of 122 iron-pnictides.	67
5.4	Technique to measure λ and $\Delta\lambda$ by MFM from Meissner repulsion (a) and vortex imaging (b,c).	71

5.5	Normalized superfluid density $\rho_s(T)/\rho_s(0) \equiv \lambda_{ab}(0)^2/\lambda_{ab}(T)^2$ vs. T and $\Delta\lambda_{ab}$ vs. T at low T	72
5.6	Spatial uniformity of λ_{ab} extracted from peak curvature of individual vortices at 5 K.	77
5.7	Vortex clusters and widely distributed pinning force suggesting Inhomogeneous vortex pinning.	77
6.1	The temperature dependence of $\rho_s(T) \equiv 1/\lambda_{ab}(T)^2$ and $\Delta\lambda_{ab}(T)$ in $\text{Ba}(\text{Fe}_{1-x}\text{Co}_x)_2\text{As}_2$ shows three systematic trends with x	81
6.2	The fit parameters from Fig 6.1(a) and temperatures of structural, magnetic and superconducting transitions	82
6.3	Sample and position variations of $\Delta\lambda_{ab}(T)$	85
6.4	Inhomogeneity in $\Delta\lambda_{ab}(T)$ observed in an $x = 11\%$ sample	87
6.5	$\rho_s(0)$ vs. T_c of cuprates and pnictides, and the phase fluctuation temperature in both 2D and 3D limit.	89

Chapter 1

Introduction of magnetic force microscopy

1.1 Fundamentals of magnetic force microscopy

Magnetic force microscopy (MFM) is an imaging technique based on atomic force microscopy. A sharp magnetic tip scans over a sample surface and images sample's magnetic structure. Since the magnetic force has longer range than the atomic force, MFM often uses non-contact mode. It is not sensitive to surface contamination and can be performed at ambient conditions.

MFM measures a derivative of the vertical component of the force \vec{F} between the sample and the tip. The motion of the cantilever follows the equation of motion for a damped harmonic oscillator:

$$m \frac{d^2 z}{dt^2} + \Gamma \frac{dz}{dt} + k(z - z_0) = F_{ex}(t) + F_z(z), \quad (1.1)$$

where m is the mass of the cantilever, Γ is the damping coefficient, $F_{ex}(t)$ is the sinusoidal driving force, z is the separation between the tip apex to the sample surface, \hat{z} is normal to both surface and cantilever, z_0 is the cantilever equilibrium position in absence of a force, and $F_z(z)$ is the vertical component of force between the cantilever and the sample. We consider only magnetic force here, therefore $F(z)$ must

be integrated over the total magnetic volume on the tip and the cantilever:

$$F_z = \frac{\partial}{\partial z} \int_{tip} dV \mu_0 (\vec{m}_{tip} \cdot \vec{H}) \quad (1.2)$$

where \vec{m} is the magnetic moment of the tip and \vec{H} is the stray field from the sample.

Assuming F_z is small, the Taylor expansion of Eq. 1.1 gives:

$$m \frac{d^2 z}{dt^2} + \Gamma \frac{dz}{dt} + k(z - z_0) = F_{ex}(t) + F_z(z = z_0) + \left. \frac{dF_z}{dz} \right|_{z=z_0} (z - z_0) \quad (1.3)$$

We define $k_{eff} \equiv k - dF_z/dz$, Eq. 1.3 can be rewritten as:

$$m \frac{d^2 z}{dt^2} + \Gamma \frac{dz}{dt} + k_{eff}(z - z_0) = F_{ex}(t) + F_z(z = z_0), \quad (1.4)$$

The cantilever resonant frequency in the presence of a force gradient is given by

$$f'_0 = \frac{1}{2\pi} \sqrt{\frac{k_{eff}}{m}} \quad (1.5)$$

Taylor expands the right hand side of Eq. 1.5 in the limit of $dF_z/dz \ll k$, we get:

$$\frac{\partial F_z}{\partial z} = \frac{2k}{f_0} \Delta f \quad (1.6)$$

where $\Delta f \equiv f' - f_0$ and f_0 is the natural resonant frequency of the cantilever.

The force gradient can be measured either in the static mode (slope detection) or AC mode (frequency modulation). In the static mode [1], one measures the change of the cantilever's amplitude or/and phase. This mode is widely used in commercial room temperature MFM. Improving the quality factor Q of the cantilever will increase the detection sensitivity at the expense of reducing measurement bandwidth. The AC mode with frequency modulation (FM) technique [2] gets around of the bandwidth limit of high Q cantilevers. In AC mode, one uses positive feedback to oscillate the cantilever at its resonant frequency and measure Δf , often by a laser interferometer.

The minimum detectable force gradient for thermally limited measurements is [2]:

$$\frac{dF}{dz}_{min} = \frac{1}{A} \sqrt{\frac{4kk_bTBW}{\omega_0Q}}, \quad (1.7)$$

where BW is the measurement bandwidth, $\omega \equiv 2\pi f_0$ and A is the amplitude of oscillation of the cantilever.

For cantilevers with high quality factors at low T , noise from the deflection sensor will likely dominate the measurement. let $n_{\Delta x}$ be the cantilever deflection sensor noise density, which yields a minimum detectable force gradient of [2]

$$\frac{dF}{dz}_{min} = \frac{2k}{\sqrt{3}\omega_0} \frac{n_{\Delta x}}{A} BW^{3/2}. \quad (1.8)$$

Note that in both limits, increasing the oscillation amplitude A and using softer cantilever (smaller k) will improve the detection sensitivity. However, large A will affect the accurate determination of z and softer cantilever may snap into the sample. Typically, we set $A \lesssim 10$ nm and use cantilevers with $50 \text{ kHz} < f_0 < 100 \text{ kHz}$ and $2 \text{ N/m} < k < 5 \text{ N/m}$.

The magnetic sensitivity of MFM depends not only on the the minimum detectable force gradient, but also on the tip shape and the magnetic field source. We use commercial AFM cantilevers and evaporate a thin layer of Fe film on the tip. For some applications, we model the tip as a magnetic monopole by assuming the tip is a infinitely long and narrow cylinder with axis and magnetization along \hat{z} . The effective position of the monopole depends on the magnetic field profile from the sample, and usually a few hundreds of nm away from the tip apex. The MFM sensitivity is calculated using the monopole model for different field source. Table 1.1 [3] lists the sensitivities and spatial resolutions of MFM, scanning SQUID microscopy (SSM) and scanning Hall microscopy (SHM). When the tip of MFM gets sufficiently close to the sample (we use $z = 15$ nm in table 1.1), MFM is expected to have at least as good spin sensitivity as SSM and much better spatial resolution.

Table 1.1: Sensitivities and spatial resolutions of MFM, scanning SQUID microscopy (SSM) and scanning Hall microscopy (SHM) when the field source is spin (dipole), magnetic flux (monopole) and line of current. We assume $z = 15$ nm for MFM and z is 0.1 of sensor size for SSM and SHM.

	Dipole		Monopole		Line of current	
	$N(\mu_b\sqrt{Hz})$	$\Delta x(nm)$	$\Phi(\Phi_0\sqrt{Hz})$	$\Delta x(nm)$	$I(A\sqrt{Hz})$	$\Delta x(nm)$
MFM	23	9	3.4×10^{-5}	10	2.6×10^{-5}	11
SHM	4.5×10^4	100	3.0×10^{-3}	108	1.2×10^{-4}	118
SSM	78	600	8.8×10^{-7}	650	5.5×10^{-9}	710

1.2 Brief Instrumentation

The research of this thesis was performed on a variable temperature MFM constructed by previous student Eric Straver using Dan Rugar's design. The physical structure of the microscope is a long metal tube under vacuum, inside of which is the microscope head (more details of the microscope head see Fig. 1.1). The vacuum tube is inserted into a liquid helium dewar with a superconducting magnet for experiments at low temperatures up to 5 T along the vacuum tube direction. The dewar is supported on an optical table mounted on air legs, with the dewar descending below floor level into a concrete pit. The insert can be raised and lowered in and out of the dewar using an electric chain hoist mounted on a uni-strut assembly above the optical table. The hoist can also slide away from the table to allow the microscope insert to be lowered onto a shelf for ease of making adjustments to the microscope. More details of the instrumentation can be found in Eric's thesis, chapter 3. In this section, I discuss the aspects that are directly relevant to the experiments performed in the thesis.

1.2.1 Two imaging modes of MFM

We perform magnetic imaging in either of the two modes, constant frequency mode or constant height mode.

Constant frequency (CF) mode uses a proportional-integral (PI) controller to control the piezotube z voltage and maintain a constant frequency shift. A DC voltage,

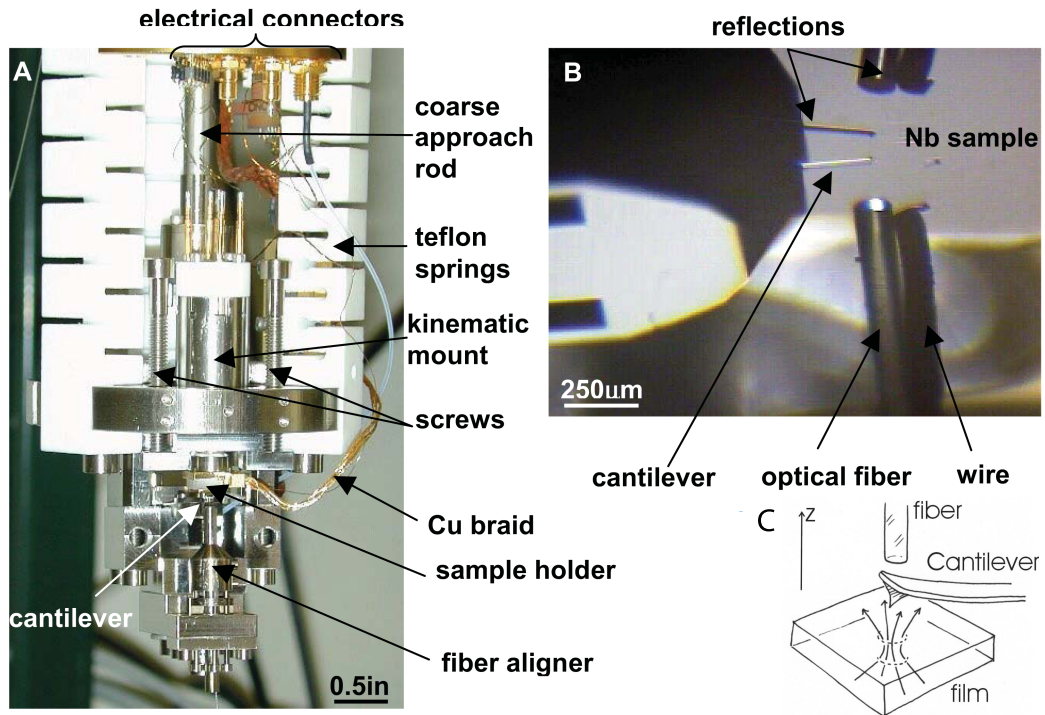


Figure 1.1: The microscope head. **A:** The piezotube is mounted on a kinematic mount supported by three screws, one of which can be turned in vacuum using a stepper motor and rotary vacuum feedthrough to enable coarse approach of the sample and the cantilever. The cantilever is mounted below the piezotube. A mechanical apparatus is used to align the optical fiber with the cantilever, and a piezostack is used to fine-tune the fiber-cantilever separation at variable temperatures. **B:** An optical microscope image of a cantilever near the surface of a sample. The reflections of the cantilever and optical fiber are visible in the sample surface. Also visible in this picture is a wire, which at one point in time was used to capacitively drive the cantilever. This wire is no longer in place however. The cantilever is either driven capacitively by a voltage applied to the sample, or directly by a voltage applied to the piezostack. **C:** Cartoon of the essential part of the MFM: a magnetic tip sitting at the end of a flexible cantilever, in vicinity of a sample.

usually a few volts, is applied to the sample to generate an electrostatic force gradient and ensure a monotonic force gradient as a function of z between the sample and cantilever. The feedback gains are increased to a point at which the frequency is held constant during the scan, but V_z does not oscillate. V_z is the primary signal for the scan, which gives the z variation with a calibration constant, and Δf is also recorded as error signal.

CF mode is often used for initial scans on an unknown surface. When the feedback is well tuned, CF mode can avoid crashing onto unexpected strong topographic features. Usually there is a slope to the sample surface that dominates the raw signal. We use a quadratic equation to describe the relative position of the sample surface to the scan axes:

$$V_z = V_x \times c_x + V_x^2 \times c_{x^2} + V_y \times c_y + V_y^2 \times c_{y^2} + c_z. \quad (1.9)$$

These coefficients are used for determining the z voltage for scans at constant heights above the sample surface.

After determining the coefficients for the plane of the sample from a set of CF non-contact mode scans, we obtain magnetic images in the constant height mode. For each x and y voltage during a scan, a corresponding z voltage is calculated and output to the piezotube from the DAQ, such that the cantilever tip moves in a plane parallel to the sample surface. The frequency shift is measured as the image signal and the dissipation signal is also commonly measured, although to date we have not obtained useful information from it. In principle, when the phase of the driving force is exactly 90° from the cantilever motion, changes in Q do not affect Δf and only changes the dissipation in the tip-sample interaction, known as dissipation force microscopy.

1.2.2 Scanner calibration

The scanning piezotubes used for the experiments in this thesis were calibrated in the x and y directions using a grid of posts with a 700 nm pitch (ASM-700-2D, fabricated by Advanced Surface Microscopy). The z direction can be calibrated at every touchdown curves: when we approach the sample to the tip-fiber assembly, we

Table 1.2: Calibration values for the piezotubes at various temperature. Also listed is the time till when the tubes were used. x and y here denote to the fast scan direction and slow scan direction respectively.

	$T(K)$	$cal_x(\mu m/V_x)$	$cal_y(\mu m/V_y)$	$cal_z(\mu m/V_z)$
Tube-1	297	3.9	5	0.60
(pre-2010)	78	3.3	3.7	0.49
	5	1.70	1.73	0.19
Tube-2	297	3.4	4.9	0.62
(since-2010)	78	2.8	3.0	0.45
	5	1.37	1.45	0.19
Tube-3	297	0.99	0.97	0.12
(pre-2006)	78	1.02	1.13	0.131
	5	0.47	0.48	0.058
Tube-4	297	1.3	1.4	0.130
(calibrated 2009)	78	1.0	1.25	0.124
not used	5	0.37	0.48	0.058

obtain an interferometry pattern from the laser reflected on the sample surface, which allows us to calibrate z in-situ. The calibration of a few scanners used and prepared for this thesis is listed in table 1.2.2. The spatial range of a piezotube depends on its dimensions. Let L be the tube length, t the wall thickness and D the diameter. The scan range in x and y is proportional to L^2/Dt and the range along $z \propto L/t$. Increasing the scan range is usually at the expense of reducing rigidity and stiffness, given the space limit in the vacuum chamber of our MFM. We observed hysteresis during scans, and obtained slightly different calibration constant along the fast scan and slow scan directions, which is marked as x and y respectively in table 1.2.2.

1.3 Applications of MFM imaging

The theme of this thesis is using MFM beyond the conventional imaging mode to study unconventional superconductors. We were able to manipulate individual superconducting vortices with a level of control that had never been demonstrated before. Such capability allows us to study the mechanic of a vortex in materials with moderate anisotropy (Chapter 2) and in quasi-two-dimensional materials (Chapter

3). We were also able to quantitatively measure the magnetic penetration depth from Meissner levitation effect (Chapter 4) and implement this technique to study the pairing symmetry and pairing mechanism of $\text{Ba}(\text{Fe}_{1-x}\text{Co}_x)_2\text{As}_2$, a family of iron-pnictide superconductors (Chapter 5-6). In this session, I will give examples from my thesis research on imaging mode of MFM, which paved the road for these novel applications.

1.3.1 Imaging individual superconducting vortices

field cooled vortices We image individual superconducting vortices in constant height scans. The spatial extension of the magnetic field of a vortex, its peak intensity, and the separation between nearby vortices all depend on the magnetic penetration depth λ . In particular, the locations of vortices is determined by the interplay between pinning and vortex-vortex interaction. When pinning is weak and uniform, the distribution of vortex positions is dominated by the vortex-vortex interaction, which is set by λ . In very pristine $\text{YBa}_2\text{Cu}_3\text{O}_{7-\delta}$ (YBCO) single crystal ($T_c = 88$ K, $\delta = 0.01$, same crystal used in Chapter 2), we observed field cooled vortices forming vortex liquid. The Fourier transform of the vortex positions gives a narrow elliptical band, shown in Fig 1.2. This is because in YBCO, the penetration depth along the crystal a and b axis do not equal: $\lambda_a > \lambda_b$. The directions of the long and short axis of the ellipse correspond to the direction of the crystal a and b axis. The eccentricity of the ellipse $e = 1.31 \pm 0.05$ gives the in-plane anisotropy. This compares well with previous results [4–8].

Flux front fine structure We are able to resolve individual vortices up to field of a few hundreds of Oersted in YBCO. This capability allows us to observe the fine structure of flux front where vortices of opposite polarities meet. Previous studies of flux front was mostly carried out by magneto optical images [9], where they could cover a large scan range of a few hundreds of the microns, but not able to resolve the details at a few ten of nanometer scale.

To generate the flux front, we ramp the field from 0 Oersted to 550 Oe, then change the field back to 0 Oe and gradually ramp it to more negative values. The temperature stays at 5K for all the fields. The flux-density depends on the magnetization history.

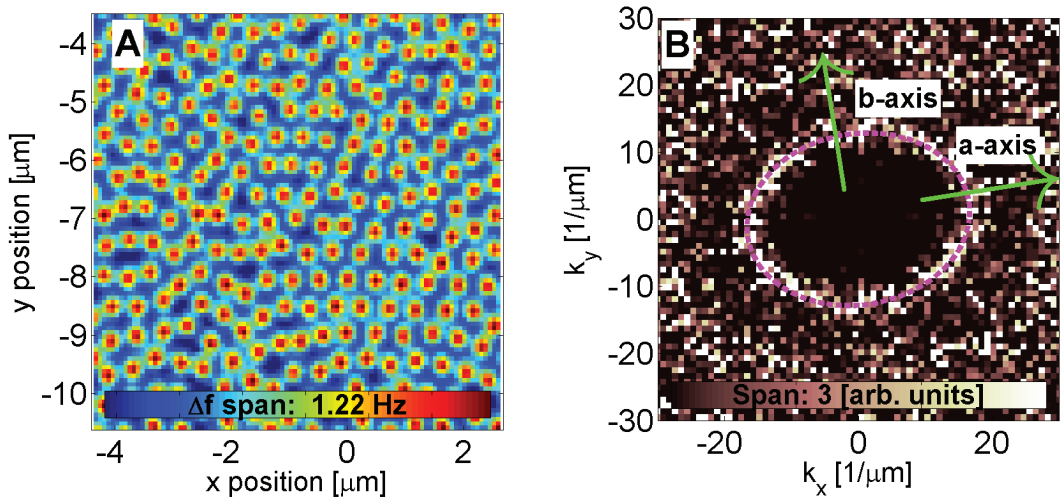


Figure 1.2: **A:** Field cooled vortices at $T = 6$ K, scan height $z = 85$ nm. **B:** Fourier transform of the vortex locations. Clearly seen is an elliptic band, also highlighted by a solid line, from which we determine that the a-axis and the b-axis are oriented $9^\circ \pm 4^\circ$ to the scan directions, as indicated by the arrows. The eccentricity of the ellipse gives the in-plane anisotropy: $\zeta = 1.31 \pm 0.05$. This result compares well with previous results [4–8].

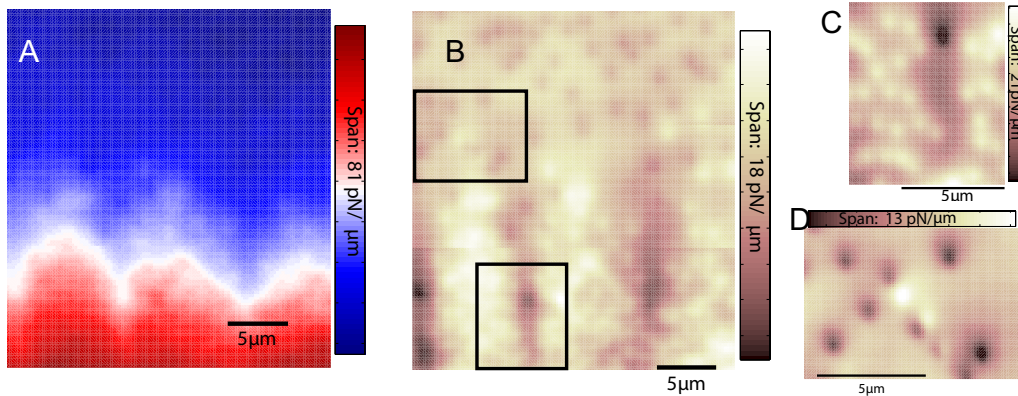


Figure 1.3: The flux front structure in a fully doped YBCO ($T_c = 88$ K) single crystal at $T = 5$ K. **A**: Raw data in constant height scan at $z = 600$ nm of the flux front. The gradient along the y direction is induced by the flux-density profile. Also shown is the corrugation pattern **B**: Removing a plane-fit from **A** to resolve individual vortices (bright dots) and anti-vortices (dark dots) as they meet. Black boxes mark the region of **C** (bottom) and **D** (upper left). **C**: image at $z = 300$ nm of the bottom region marked in **B** to show that the “finger” shaped structure in the corrugation pattern has very low local flux-density. **D**: image at $z = 300$ nm of the upper left region marked in **D** to show the existence of vortex-antivortex pairs.

When we change the field to 0 from 550 Oe, there are still a lot of flux trapped in the sample. When we flip the field direction, flux with opposite polarity comes into the sample from the edge. At certain applied field, we will see the flux-antiflux boundary in our field of view (Fig 1.3).

According to the Bean model [10], the flux-density simply has a gradient of $4\pi J_c/c$ as a function of distance from the sample edge. We observe the vortex front to be corrugated on the scale of a few microns, and a field gradient on a larger scale consistent with the Bean model (Fig 1.3). When we remove the gradient, we observe that the corrugation is caused by alternating “finger” composed of few vortices penetrating into the anti-vortex region. Some vortex-antivortex pairs are stable, while other vortices got annihilated with antivortices over time or by changing field.

1.3.2 Two approaches of force reconstruction from vortex images

Because the sample exerts a force on the magnetic tip, the tip must exert an equal and opposite force on the sample, usually considered a disadvantage. In a few chapters of this thesis, we deliberately make use of the lateral components of this force force, $F_x\hat{x} + F_y\hat{y} = \vec{F}_{lat}$, for manipulation. We magnetize the tip parallel to the vortices to give tip-vortex attraction, the magnitude of which we control by varying the tip-surface distance, z . Qualitatively, the smaller the z , the larger the applied force.

It is crucial for us to know quantitatively the value of the applied force in applications of manipulation. Although we directly measure $\partial F_z/\partial z$, we can determine the lateral force exerted on a vortex by measuring and applying either of the two analyses. They are the methods we use in chapter 2 and chapter 3 to obtain the force for manipulation.

The first approach does not require any modeling. When a vortex is stationary, \vec{F}_{lat} is given by

$$\vec{F}_{lat} = -\hat{x}\partial U/\partial x - \hat{y}\partial U/\partial y, \quad (1.10)$$

where

$$U(x, y, z) = - \int dz' \int dz'' \partial F_z(x, y, z'')/\partial z''. \quad (1.11)$$

Therefore, $U(x, y, z)$ can be obtained by taking $\partial F_z/\partial z$ images of the same area at consecutive heights z 's and integrated twice along z [11]. From $U(x, y, z)$, we take derivative along x and y to obtain F_x and F_y . An example is shown in Fig. 1.4.

The second approach does not require vortices to be stationary but uses a model. We obtain the magnitude of peaks from vortex images, from which we use a model to integrate $\partial F_z/\partial z$ to get the maximum vertical force F_z^{max} . F_{lat}^{max} is proportional to F_z^{max} up to a geometric constant: $F_{lat}^{max} = \alpha F_z^{max}$, where α depends weakly on tip shape, with $0.3 < \alpha < 0.4$ for a wide range of shapes [12, 13]. We use $\alpha = 0.35$, adding at most a 25% error to conversions from F_z^{max} to F_{lat}^{max} .

The model we use is only for convenient integrating $\partial F_z/\partial z$ to give F_z , and its detail does not affect the resultant force. For simplicity, we model the both the tip and

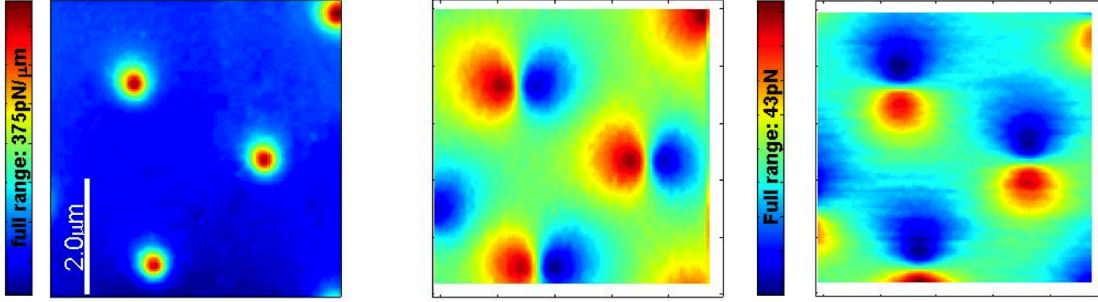


Figure 1.4: An example of force reconstruction for the $\text{YBa}_2\text{Cu}_3\text{O}_{7-\delta}$ (YBCO) single crystal. **A**: Image of static vortices acquired at $T = 5.2$ K, $z = 60$ nm. **B-C**: Reconstructed force by integrating many images including that in **(A)** taken at consecutive heights: \hat{x} (B) and \hat{y} (C) components of the attractive force between the tip and the vortex at $z = 60$ nm

the vortex as magnetic monopoles, so called monopole-monopole model. This model assumes the tip as an infinitely long and narrow cylinder with axis and magnetization along \hat{z} . When $z \gg \lambda$, the field from a vortex is well approximated by the field from a monopole residing λ below the surface of the superconductor, which is assumed to fill the half space $z \leq 0$ [12, 14]:

$$\vec{B}[\vec{R}, z] \approx \frac{\Phi_0}{2\pi} \frac{(\vec{R} + (z + \lambda)\hat{z})}{(R^2 + (z + \lambda)^2)^{3/2}} \quad (1.12)$$

The resulting force acting on the tip due to the interaction with the vortex is

$$\vec{F}(\vec{R}, z) \approx \tilde{m}\vec{B}(\vec{R}, z), \quad (1.13)$$

where \tilde{m} is the dipole moment per unit length of the tip.

The peak magnitude of the vortex is given as:

$$\max(\partial F_z / \partial z) = \frac{\tilde{m}\Phi_0}{\pi(z + h_0)^3}. \quad (1.14)$$

Here, $h_0 = \lambda + \Delta z + \delta z$, where Δz is the offset of the tip's effective monopole from the tip apex, δz is an estimate for the thickness of the non-superconducting layer at the surface of the superconductor. The typical parameters of tips and cantilevers

Table 1.3: **cantilever parameters:** d = nominal thickness of the Fe coating, f_0 = resonant frequency, k = cantilever spring constant, Q_{amb} and Q_{vac} are the quality factor of the oscillation measured in ambient conditions and at 5K at pressure $< 10^{-8}$ mbar. \tilde{m} and h_o are parameters in the monopole model of the MFM tip. \tilde{m} is the magnetic moment per unit length and h_o is the offset in tip-sample separation due to the simplification of the tip geometry in the monopole model.

Tip	d [nm]	f_0 [kHz]	k [N/m]	Q_{amb}	Q_{vac}	\tilde{m} [nAm]	h_o [nm]
A	40	51	2.3 ± 0.2	350	$> 4E5$	32 ± 1	250 ± 5
B	40	75	4.0 ± 0.1	350	$> 4E5$	28 ± 3	350 ± 20

used in the thesis, as well as \tilde{m} and h_o deduced from the monopole-monopole model, are shown in Table 1.3.2.

The maximum applied force is given by

$$F_z^{\max} = (\tilde{m}\Phi_0/2\pi)/(z + h_o)^2, \quad (1.15)$$

and $F_{lat}^{\max} = \alpha F_z^{\max}$.

This approach of reconstructing the force agrees well with the first approach. The monopole-monopole model is also sufficient to well describe the vortex peak magnitude at various heights, as shown in Chapter 2 and Chapter 3. As a result, we often use the second approach with the simple monopole-monopole model to obtain the maximum force applied in a scan.

1.3.3 Simultaneous MFM and electric force microscopy

One should be aware that a cantilever in force microscopy is sensitive to all kinds of force. To eliminate the effect of short range atomic force and van der Waals force, all of our MFM scans are performed at least 30 nm away from the surface. To minimize the long range electrostatic force, which comes from the capacitive coupling between the tip and sample, we bias the sample voltage to cancel the contact potential difference V_{cont} between the tip and the sample (usually a fraction of a volt). V_{cont} is determined by obtaining the maximum Δf (minimum $\partial F_z/\partial z$) as a function of tip-sample voltage V_{dr} , as shown in Fig. 1.5.

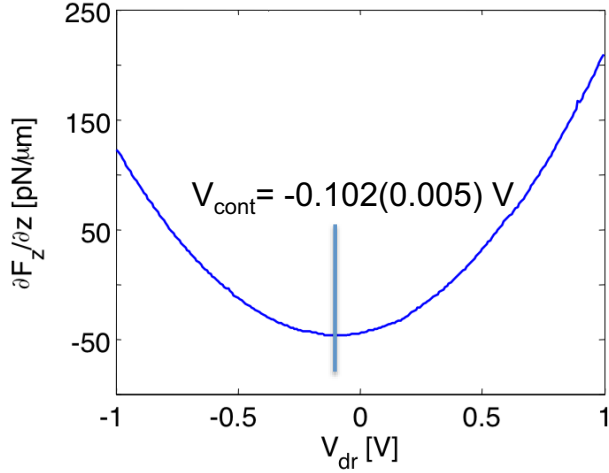


Figure 1.5: $\partial F_z/\partial z$ as a function of tip-sample voltage V_{dr} at height $z = 80$ nm. The value of V_{dr} that minimized $\partial F_z/\partial z$ gives the contact potential difference between the tip and the sample. Data taken on the fully YBCO single crystal.

Deliberately using the electric force, we can perform electric force microscopy by application an AC bias voltage $V_0 \sin(\omega_2 t)$ between the tip and the sample. The resultant force derivative is [15]:

$$F'_E = \frac{V_0^2 \sin^2(\omega_2 t)}{2} \frac{\partial^2 C}{\partial z^2} + \frac{Q_s V_0 \sin(\omega_2 t)}{2\pi\epsilon_0 z^2} \left(\frac{C}{z} - \frac{1}{2} \frac{\partial C}{\partial z} \right) \quad (1.16)$$

where Q_s is the local static charge on the sample surface, C is the capacitance between tip and the sample. As shown in Eq. 1.16, the charge Q_s induces a term at frequency ω_2 , which could be picked up by a lock-in amplifier.

We are also able to perform MFM scan and EFM scan simultaneously. During the scans, we apply an sinusoidal V_{dr} , $V_{dr} = V_1 + V_2 \sin(\omega_2 t)$ and use feedback circuit to lock Δf to its local maximum. The EFM channel records V_1 , whose change measures the local electric potential change on the sample surface. The MFM channel records Δf as usual. The crosstalk between the two channels is neglect. This capability will be useful in future studies, such as search for electric charge associated with a superconducting vortex, or phase transitions that involve both charge order and magnetic order.

Chapter 2

Mechanics of individual vortices in a cuprate superconductor $\text{YBa}_2\text{Cu}_3\text{O}_{7-\delta}$ with moderate anisotropy

Abstract: Superconductors often contain quantized microscopic whirlpools of electrons, called vortices, that can be modelled as one-dimensional elastic objects [16]. Vortices are a diverse playground for condensed matter because of the interplay between thermal fluctuations, vortex-vortex interactions, and the interaction of the vortex core with the three-dimensional disorder landscape [17–20]. While vortex matter has been studied extensively [16, 21, 22], the static and dynamic properties of an individual vortex have not. Here we employ magnetic force microscopy (MFM) to image and manipulate individual vortices in detwinned, single crystal $\text{YBa}_2\text{Cu}_3\text{O}_{6.991}$ (YBCO). We directly measure the interaction of a moving vortex with the local disorder potential. We find an unexpected and dramatic enhancement of the response of a vortex to pulling when we add transverse agitation. In addition, we find enhanced vortex pinning anisotropy that discloses clustering of oxygen vacancies in our sample and demonstrates the power of MFM to probe vortex structure and microscopic defects that cause pinning. The work described in the chapter appears in *Nature*

Physics, **5**, 35 (2009).

2.1 Introduction

A superconducting vortex is characterized by two length-scales: the nanoscale core size ξ (the coherence length) and the much larger magnetic penetration depth, λ . Pinning occurs when the core is co-located with a defect that locally suppresses superconductivity. λ determines the decay length for the currents encircling the core and the elastic properties of a vortex. Here we probe the dynamics of a driven vortex, which is especially interesting when pinning and elasticity compete. Furthermore, we establish a dragged vortex as a probe that extends deep into the bulk of the sample to interact with defects far from the surface, circumventing disadvantages of other local-probe techniques that give information only about the immediate vicinity of the surface [23]. Previous strategies for manipulating single vortices in superconductors usually applied forces relatively delocalized on the scale of λ [24–26]. We use MFM to combine imaging and vortex manipulation with a level of control far beyond what has been demonstrated before [27, 28]. This capability may enable testing vortex entanglement [29] and schemes for quantum computation [30, 31].

Our sample is ideal for studying the interplay between pinning and elasticity, with relatively weak, well-controlled, pinning and relatively rigid vortices. The platelet-shaped single crystal was grown from flux in a BaZrO₃ crucible for high purity and crystallinity [32]. The (001) surfaces were free of visible inclusions. Mechanical detwinning was followed by annealing to oxygen content $7 - \delta = 6.991$, implying 88 K [32–34]. The sample was stored at room temperature for a few years. In YBCO superconductivity arises in CuO₂ planes, parallel to the a , b axes, and in Cu-O chains, along the b -axis. In pristine samples, such as ours, oxygen vacancies in these chains are the dominant source of pinning. The orthorhombic crystal structure gives rise to penetration depth anisotropy, allowing us to determine the orientation of the crystal axes in-situ by finding the directions along which vortex spacings were extremal, as shown in Fig. 1.2. We obtain that the crystal a -axis is 9° from \hat{x} .

2.2 Experiments and discussions

MFM employs a sharp magnetic tip on a flexible cantilever. Our tip magnetization provided an attractive tip-vortex force, \mathbf{F} . While rastering in the $x - y$ plane parallel to the sample surface, we measure local variations in the resonant frequency of the cantilever to determine $\partial F_z / \partial z$ [2]. We deliberately use \mathbf{F} 's lateral components, $F_x \hat{x} + F_y \hat{y} = \vec{F}_{lat}$, for vortex manipulation.

At low temperatures ($T \approx 5$ K), we observed no vortex motion up to our largest lateral force, 20 pN. At higher temperatures, pinning is reduced, and we could reduce the tip-sample distance z to tune from non-invasive imaging to manipulation. Fig. 2.1 shows typical examples for individual, well-isolated, vortices. Incrementing the tip towards the surface for each scan took us gradually from surveillance mode (Fig. 2.1c), where imaging does not disturb vortices, to manipulation mode (Fig. 2.1d), where $F_{lat}^{max} \equiv \max(F_{lat})$ was large enough to cause observable depinning. The similarity of the behaviour of vortices pinned at different locations indicates the uniformity of the pinning landscape in this sample. A single vortex subjected to the dragging force from the MFM tip shows three surprising behaviors, as discussed in the following sessions.

2.2.1 Wiggling effect along the slow scan direction

The dramatic asymmetry between the two scan axes in Fig. 2.1d shows the first of our three main findings: ‘vortex wiggling’. Adding an alternating transverse force enhances vortex dragging markedly. The wiggling occurs because of the rastering associated with imaging: between incremental steps forward along the ‘slow’ scan direction, we raster the tip left and right along the ‘fast’ scan axis. If $F_{lat} \equiv |\vec{F}_{lat}|$ is small, this creates an image of a stationary vortex (Fig. 2.1a,c,e). When F_{lat} is large, the vortex moves as the tip passes over it (Fig. 2.1b,d,f). Although this motion is substantial in the quasi-one-dimensional (1D) scans along the fast axis (Fig. 2.1f), it is much larger along the slow axis (Fig. 2.1d).

We study wiggling further in Fig. 2.2. Fig. 2.2a shows a scan that we acquired after imaging the same area over and over, resulting in an enhanced wiggling effect.

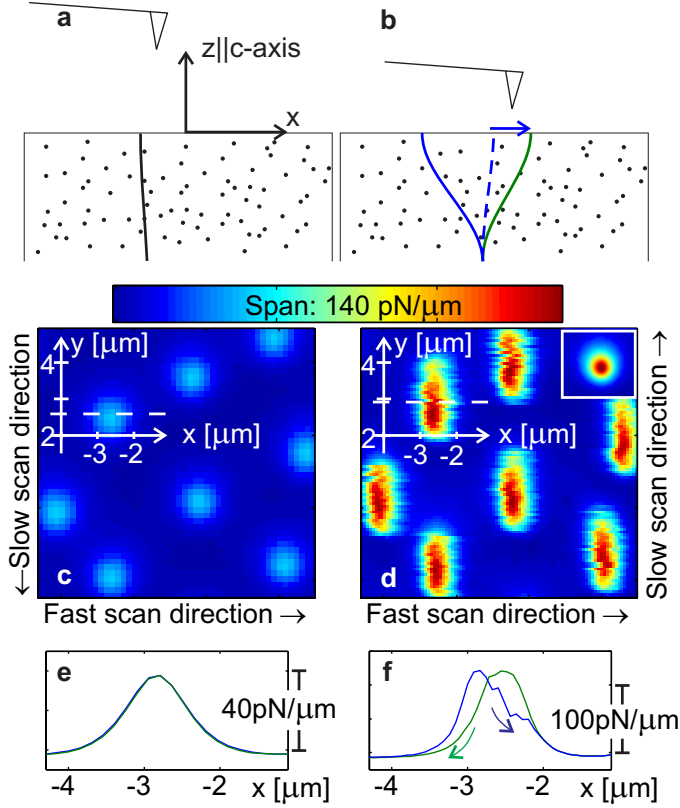


Figure 2.1: MFM imaging and manipulation of individual vortices in YBCO at $T = 22.3 \text{ K}$. **a,b**: Schematic diagrams, not drawn to scale, showing an MFM tip (triangles) that attracts a vortex (thick lines) in a sample with randomly distributed point pinning sites (dots): at 'surveillance' height, the applied force F_{lat} is too weak to move the vortex (**a**); at manipulation height, the vortex moves right and then left, as the tip rasters over it (**b**). Here, we illustrate what happens in a scan along $+\hat{x}$, as indicated by the arrow. Also shown are three configurations of the vortex, previously dragged along $-\hat{x}$: the blue line on the left illustrates the vortex before the tip drags it to the right, the dashed blue line shows an intermediate configuration as it follows the tip and the green line on the right shows the final configuration, after the tip moves away. **c,d**: MFM scans for two different scan heights (colour scale gives $\partial F_z / \partial z$; fast scan and slow scan directions are indicated on the frame): $z = 420 \text{ nm}$ (maximum applied lateral force $F_{lat}^{max} = 6 \text{ pN}$), not low enough to perturb vortices at this temperature (**c**); $z = 170 \text{ nm}$ ($F_{lat}^{max} = 12 \text{ pN}$), low enough to drag the vortices significantly (**d**). Inset: Scan at 5.2 K , showing a stationary vortex at tip height and force comparable to those in the main panel. **e**: Line cut through the data in **c** along the dashed line, showing the signal from a stationary vortex (blue). Overlapping it is a line cut from the reverse scan (green). **f**: Line cut through the data in **d** along the dashed line, showing a typical signal from a dragged vortex. The right arrow shows the data acquired with the tip moving along $+\hat{x}$, as in **d**; the left arrow shows the data acquired with the tip moving back along $-\hat{x}$.

Line scans along $\pm\hat{x}$ from that image (Fig. 2.2b) do not differ from Fig. 2.1f. To study the vortex after completing the scan in Fig. 2.2a, we moved the tip back and forth over the centre of the vortex along $\pm\hat{y}$ to obtain Fig. 2.2c,d. Details of the motion along the fast axis (Fig. 2.2b) are similar to motion along what was the slow axis (Fig. 2.2c,d). A vortex moves in jerks, reminiscent of avalanches [20], but the total distance moved differs substantially. Moreover, Fig. 2.2c,d shows that although a vortex moves very freely between the initial and final positions in Fig. 2.2a, it does not readily move outside this range. In fact, we were never able to permanently drag a vortex very far from its original location, contrary to the case in thin films [27]. This tethering suggests that each vortex was pinned along its full length across the 40- μm -thick crystal, and that we observed the vortex stretching.

A vortex presumably stops moving where elasticity and pinning balance F_{lat} . Qualitatively, wiggling helps segments of the vortex to depin, facilitating the extra motion along the slow axis. Confirming this is Fig. 2.2 with the enhancement of the effect by adding wiggling cycles. Further test of the transverse agitation is shown in Fig. 2.3. By wiggling the tip away from a vortex, the vortex snapped towards the tip.

Wiggling is reminiscent of ‘vortex shaking’, used to accelerate equilibration in vortex matter by oscillating a magnetic field perpendicular to the applied magnetic field generating the vortices [21, 35, 36] and may be the mechanism for it. Our single-vortex data should be amenable to more advanced and quantitative theoretical modelling to describe the wiggling.

2.2.2 Exponential T dependence of the depinning force

Depinning is often measured by the critical current density J_c , the current density required to generate measurable dissipation across the sample. We directly probe the local pinning sites by depinning individual vortices, with the advantage of studying them when they are well-separated to eliminate vortex-vortex interactions. We define the local depinning force F_0 as the lateral force required to create the minimum detectable motion. The detection threshold depends on T , and it is better than 50nm

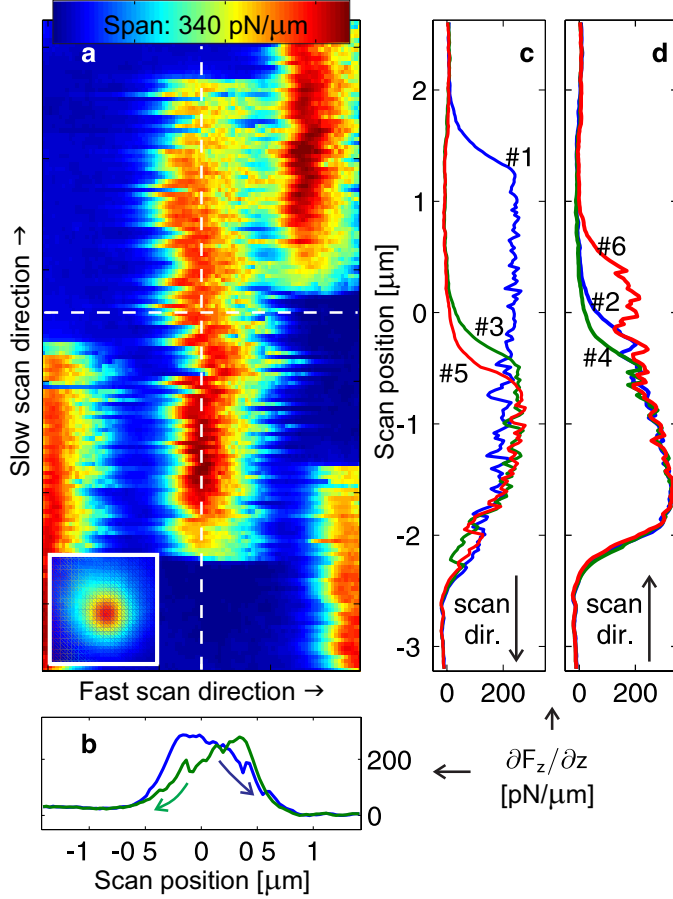


Figure 2.2: MFM image and line scans at $T = 20$ K, showing how wiggling enhances dragging along the slow direction. **a**: Scan at $z = 80$ nm ($F_{lat}^{max} \approx 20$ pN), acquired after repeated imaging, reversing the slow scan direction for each new scan, which enhances the wiggling effect. Scan directions are denoted on the frame; dashed lines show the trajectories of the line scans in **b**, **d**. Inset: Scan with similar parameters at 5.2 K, where vortices were immobile. **b**: Line scans from **a** along the horizontal dashed line. Arrows show the scan direction. **c,d**: Immediately after the scan in **a**, we scanned back and forth along the vertical dashed line at $z = 80$ nm ((**c**) scans down, (**d**) scans up). Indices: Order of line-scan acquisition.

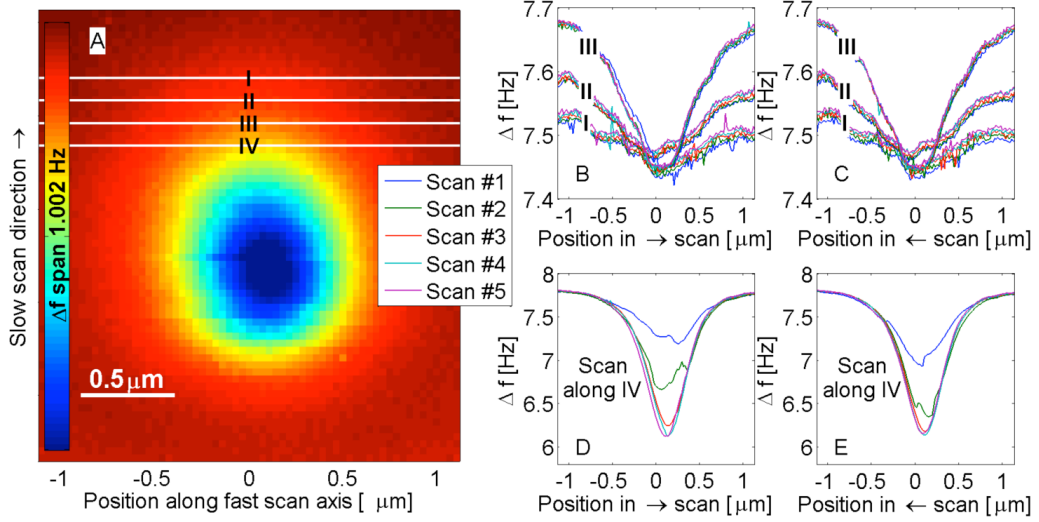


Figure 2.3: Test of transverse agitation at $T = 20$ K. **(A)** Scan at $z = 210$ nm ($F_{lat}^{max} \approx 12$ pN). The vortex is seen to move under the influence of the tip, but not extensively. The lines marked by I-IV denote where and the order we scanned the tip back and forth. The legend enumerates the order of lines scans (1-5), which are shown in the panels on the right. **(B-E)** Line scans at $z = 105$ nm ($F_{lat}^{max} \approx 17$ pN). **(B)** Scans from left to right along tracks I-III. Each line scan was repeated five times, as denoted in the legend. The slight angle between the scan plane and the sample plane is evident in the different offset of the background value of for I, II and III. No motion is evident in scans I, II. Slight motion along the fast scan direction (50nm) is evident in the offset between scan 1 and the rest of the scans in III. **(C)** Like B but for scans from right to left. No motion is evident. **(D, E)** Vortex motion towards the tip along both the slow direction and the fast direction are evident. Clearly every time the tip approaches the point of closest approach, the vortex moves a little towards it. One can see that in the first scan the vortex was near where it was after the last scan in (C) and that it progressed towards the tip in subsequent line scans.

for $T < 50$ K, 25 nm for $T < 40$ K, 10 nm for $T < 35$ K, and on the order of ξ for $T < 30$ K. All vortices measured at the same temperature depinned in a narrow range of forces, in contrast to YBCO thin films [37], in which the width of the distribution of depinning forces is at least several times the mean. The uniformity of F_0 indicates the uniformity of the pinning landscape in our single-crystal YBCO sample.

The temperature dependence of F_0 is consistent with $\exp(-T/T_0)$, decreasing by more than an order of magnitude from $T = 7$ K to $T = 42$ K (Fig. 2.4). This strong dependence cannot be attributed to variation in the penetration depth or the vortex core size, both of which depend only weakly on temperature in this range. The exponential dependence indicates that thermal fluctuations are playing a role [16, 38]. Previous observations of this uncommon dependence have been in macroscopic measurements on less pristine samples [39], and were explained in terms of creep [16]. In creep, vortices move by thermally activated jumps, with the rate given by the usual $\exp(-E_a/T)$, in which the barrier height E_a is a decreasing function of the driving force. Since $\exp(-T/T_0)$ follows from averaging over many vortices, it is unclear that a similar explanation should apply in the single-vortex manipulation limit. A logarithmic scan time dependence of T_0 , which would be a clear signature of creep, was not observed in our preliminary search at higher applied forces. Thus, the striking $\exp(-T/T_0)$ dependence of F_0 requires further investigation, both experimental and theoretical.

2.2.3 Force and direction dependence dragging along the fast scan direction

Our third observation is that when $F_{lat}^{max} \gg F_0$, the distance w a vortex is dragged along the fast scan direction depends not only on the applied force, but also on the direction of the dragging. We extract w by subtracting the line width of a dragged vortex from its static image profile at a lower temperature, as shown in Fig. 2.5. We obtain a strong dependence of w on the applied force dependence of w : w increases nearly quadratically with applied force F_{lat} . Moreover, we can drag a vortex farther along the fast axis if it is along the YBCO b axis than if it is along the a axis. Both

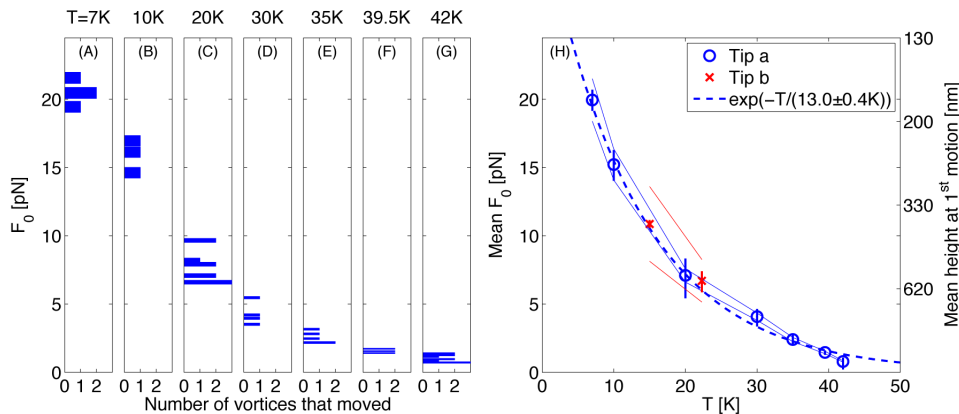


Figure 2.4: **(A-G)** Distribution of depinning forces, F_0 , vs. temperature T . **(H)** Mean values of F_0 vs. T . Dashed line: fit to $\exp(-T/T_0)$, where $T_0 = 13.0 \pm 0.4$ K. The right vertical axis shows the scan height z corresponding to F_0 .

effects are shown in Fig. 2.6. To rule out the possibility that the dragging anisotropy was related to a residual in-plane component of the tip magnetization, we repeated the experiment in different cool-downs using two different tips. The results were the same even though we mounted the second tip at a different azimuthal angle to preserve the scan directions while ensuring that any in-plane magnetization component was rotated.

The behavior along the fast axis can be analysed as individual one-dimensional scans. As the tip approaches a vortex, F_{lat} increases until, if it overcomes pinning, the vortex moves. The vortex then moves until pinning and the growing elastic force balance F_{lat} , presumably when F_{lat} is maximal, enabling us to treat this as a static problem. We have constructed a model based on weak collective pinning (WCP) [16] to explain the w dependence on F_{lat}^{max} . WCP assumes that pinning is only by the collective, cumulative, effect of many pinning sites, each too weak to pin a vortex on its own, and that vortices are elastic strings [40], as described in Ginzburg Landau theory [40]. A characteristic length, L_c , emerges from the competition between pinning and elasticity: a vortex is broken into elastically coupled L_c segments, each pinned by a characteristic force, F_p . Each segment interacts with its neighbours on both ends by an elastic force, which we model as a spring with spring constant k . A vortex takes advantage of pinning by bending on a length $L \gg L_c$, but it cannot bend for $L \ll L_c$.

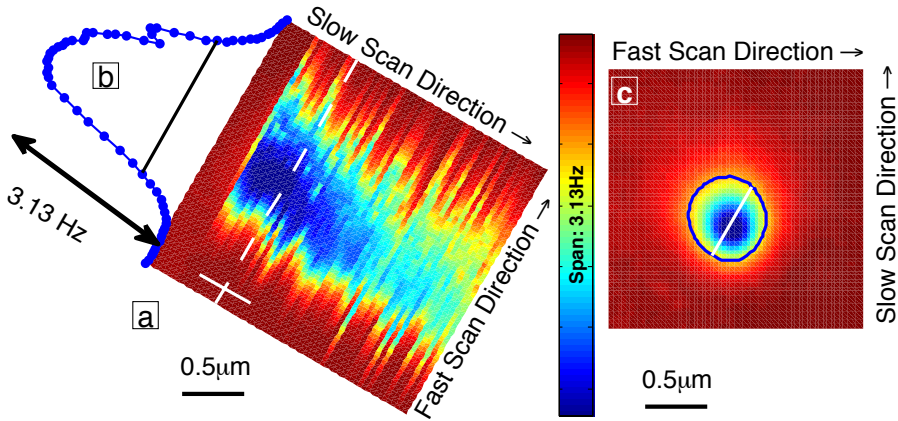


Figure 2.5: Extracting the dragging distance $w(\varphi)$. **a:** Scan at $T = 20$ K and height $z=80$ nm ($F_{lat}^{max} \approx 20$ pN) at angle 60° to \hat{x} . Dashed line denotes scan line cutting region of extremal vortex signal. Solid line denotes range from which $w(\varphi)$ was determined. **b:** Single line scan extracted at the dashed line. Line denotes 0.23 of the peak value, where we extract the width. **c:** Scan at $T = 5.2$ K. The width of the static vortex is extracted by the same procedure as in procedure as in panels (a) and (b), as denoted by the white line on the contour at 0.23 of the peak value.

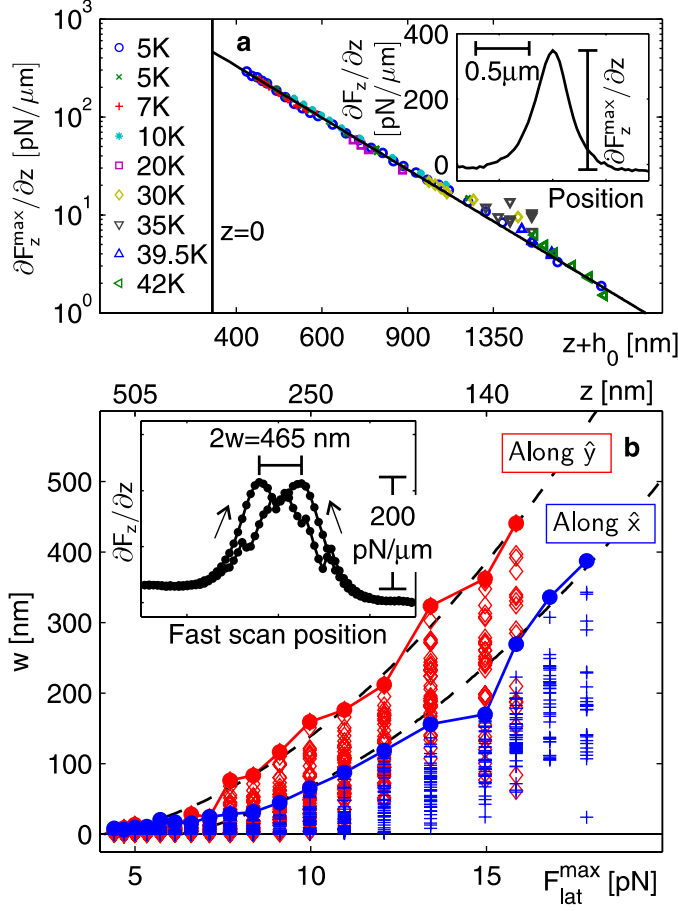


Figure 2.6: Force dependence of the dragged distance, w , along the fast axis. **a**: Force calibration: magnitude of peaks from vortices, $\max(\partial F_z/\partial z) \equiv \partial F_z^{\max}/\partial z$, versus scan height at various temperatures. Clearly the temperature dependence in this range is weak. The solid line is a fit to $\max(\partial F_z/\partial z) = (\tilde{m}\Phi_0/2\pi)/(z+h_0)^3$ ($h_0 = 358 \pm 5$ nm, $\tilde{m} = 32 \pm 1$ Am, detail see Chapter 1). The excellent fit enables us to use $F_z^{\max} = (\tilde{m}\Phi_0/2\pi)/(z+h_0)^2$. The maximum applied lateral force is given by $F_{\text{lat}}^{\max} = \alpha F_{v,z}^{\max}$. For a wide range of tip shapes $0.3 < \alpha < 0.4$ [13]. We set $\alpha = 0.35$, adding at most 25% systematic error to F_{lat}^{\max} . Inset: Single line form a scan at $z = 65$ nm, $T = 5.2$ K, showing the peak height for an immobile vortex (Here, $\max(\partial F_z/\partial z) = 365$ pN/ μm). **b**: Distance moved by the vortex along the fast direction versus z (top axis) acquired at $T = 25$ K versus F_{lat}^{\max} (bottom axis). In addition to the maximum w (filled circles), we plot the distribution (diamonds and crosses), which shows the stochasticity of the vortex motion. Other errors are not shown. Dashed lines are fits to equation (1) (along \hat{x} : $F_1 = 6.3 \pm 0.4$ pN, $F_p \varepsilon_{\perp}/L_c = 272 \pm 12$ pN $_2/\mu\text{m}$; along \hat{y} : $F_1 = 4.1 \pm 0.7$ pN, $F_p \varepsilon_{\perp}/L_c = 212 \pm 17$ pN $_2/\mu\text{m}$). Inset: Subsequent line scans showing the jerky nature of the vortex motion and how w was extracted from the difference of the vortex positions in pairs of subsequent line scans.

To model the w dependence of F_{lat} , we assume that when the vortex is dragged the only distortion is stretching along the dragging direction. We denote by u_n the displacement of the n^{th} segment from the $(n + 1)^{th}$ segment, where n enumerates the segments starting from the surface. For each segment, we have:

$$F_n - ku_n + ku_{n-1} = F_p \quad (2.1)$$

with $u_N = 0$ and $u_0 = 0$. Assuming the dragging force on each segment decays exponentially: $F_n = F_1 \exp(-(n - 1)L_c/\Lambda)$. Summing Eq. 2.1 over n :

$$F = \sum_{n=1}^N F_n = F_1 \sum_{n=1}^N q^{n-1} = F_1 \frac{1 - q^N}{1 - q} = NF_p, \quad (2.2)$$

where $q = \exp(-L_c/\Lambda)$ and the total external force on the N segments that move is F . Multiplying Eq. 2.1 by n and summing gives $\sum_{n=1}^N nF_n + k \sum_{n=1}^N u_n = \sum_{n=1}^N F_p$. Noting that $w = \sum_{n=1}^N u_n$, we find:

$$w = \frac{1}{k} \left(\frac{N(N + 1)}{2} F_p - F_1 \left(\frac{10(N + 1)q^N}{1 - q} + \frac{q(1 - q^N)}{(1 - q)^2} \right) \right).$$

Using the last equality in Eq.2.2, we get:

$$w \approx \frac{F}{2kF_p} \left(-F + \frac{2}{1 - q^{F/F_p}} F - \frac{1 + q}{1 - q} F_p \right), \quad (2.3)$$

when $F = F_{lat}^{\max} > F_p \Lambda / L_c$, we get:

$$w \sim \frac{F_{lat}^{\max} (F_{lat}^{\max} - F_1)}{2kF_p}, \quad (2.4)$$

where the elastic constant k accounts for the resistance of the vortex to tilting.

To calculate k , We start from the line energy of a vortex in a biaxial crystal, which can be shown to be given by $\varepsilon(\varphi, \theta) = \varepsilon_0 \sqrt{\varepsilon^2 \eta(\zeta, \varphi) \sin^2 \theta + \cos^2 \theta}$ [41], where φ and θ are the azimuthal and polar angles the vortex is pointing along, as defined in Fig. 2.7.

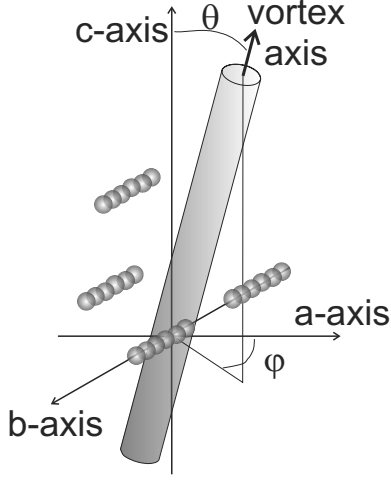


Figure 2.7: Cartoon showing crystal axes, vortex axis, the clusters and the angles used in the equations, θ and φ .

We define $\varepsilon \equiv \lambda_{ab}/\lambda_c$, $\eta \equiv \zeta \cos^2 \varphi + \zeta^{-1} \sin^2 \varphi$, $\zeta \equiv \xi_b/\xi_a = \lambda_a/\lambda_b$ is the in-plane anisotropy of coherence length (vortex core size) and $\varepsilon_0 \equiv \frac{(\Phi_0/\lambda_{ab})}{4\pi\mu_0} \log(\lambda_{ab}/\xi_{ab})$, where $\xi_{ab} = \xi_a \xi_b$.

The total elastic energy of the stretched vortex, not including pinning, as a sum over all segment is:

$$E_{elastic} = \sum_{n=1}^N \varepsilon_l(\varphi, \theta_n) L_c / \cos \theta_n,$$

where θ_n is the polar angle of segment n . Assuming $\theta_n \ll 1$, we expand to second order in θ_n and find that, up to a constant:

$$E_{elastic} \sim \sum_{n=1}^N \varepsilon_{\perp}(\zeta, \varphi) L_c \theta_n^2,$$

where $\varepsilon_{\perp}(\zeta, \varphi) = \varepsilon_0 \varepsilon^2 \eta(\zeta, \varphi)$. Next we note that $\theta_n \sim u_n/L_c$ for $\theta_n \ll 1$, and write $E_{elastic}$ in terms of u_n . Finally, we take a derivative of u_n and obtain the second two terms on the left hand side of Eq.2.1, with the identification:

$$k \equiv \varepsilon_{\perp}/L_c \tag{2.5}$$

therefore, using Eq. 2.4 and Eq. 2.5, we get:

$$w \sim \frac{F_{lat}^{\max}(F_{lat}^{\max} - F_1)}{2F_p \varepsilon_{\perp} / L_c} \quad (2.6)$$

As shown in Fig. 2.6, Eq. 2.6 gives a reasonable fit to the data for large F_{lat}^{\max} , where the exact shape of the top portion of the vortex and the fine details of the pinning landscape are not important.

Eq. 2.6 also explains the anisotropy qualitatively: $w \propto L_c / \varepsilon_{\perp} F_p$. The penetration depth imparts in-plane anisotropy to $\varepsilon_{\perp}(\zeta, \varphi) \propto \eta(\zeta, \varphi)$ [16, 41], implying that it is easier to tilt a vortex towards the b axis. In addition, because of the in-plane anisotropy of the vortex core radius, even for point pinning, the effective pinning potential is less steep along the b axis, implying a smaller depinning force. Eq. 2.6 thus naturally explains the weak dependence of the anisotropy on F_{lat}^{\max} and T , seen in Fig. 2.8. When $F_{lat}^{\max} \gg F_1$, the only dependence on F_{lat}^{\max} is an overall scale. The same is true for the T dependence, because both the superconducting parameters and the defect structure depend only weakly on T in our range [6].

In order to quantitatively understand the dragging in-plane anisotropy, we obtain w as a function of fast scan angle (Fig. 2.8). We found that the main axes of the anisotropy were tilted away from the scan axes and matched the crystal axes, and by applying more force and/or by increasing the temperature we were able to increase w , but could not change the anisotropy appreciably. A similar effect appeared using different tips and for every vortex that we probed.

We revisit the WCP model in biaxial superconductors and describe F_p and L_c in fundamental length scales. In WCP, the typical pinning energy for an object taking up a volume V is $U_{pin} \sqrt{n_i V}$, where n_i is the pinning site density and U_{pin} is the energetic price of depinning. The square root results from the randomness of the meander of the vortex through the pinning potential. It is akin to a random walk. The effective volume taken up by a vortex segment is roughly $V = \xi_a \xi_b L$, where L is the length and ξ_a and ξ_b are the radii of the core along the a and b axes, so that the

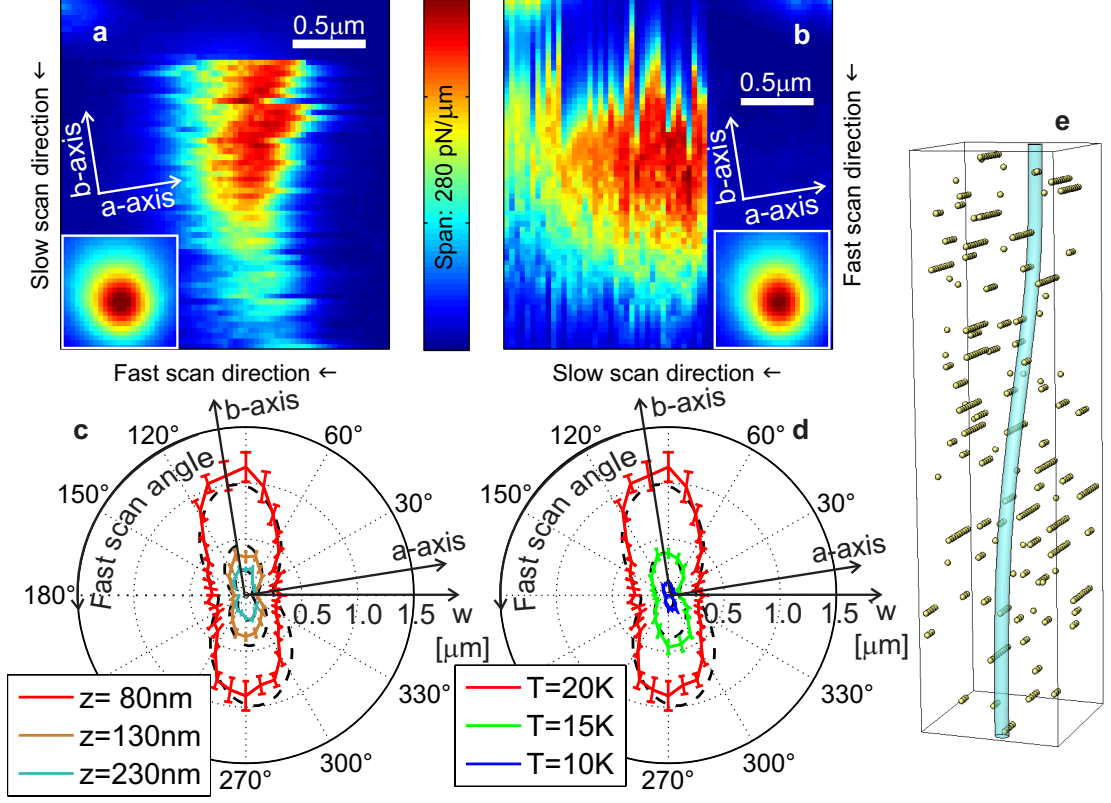


Figure 2.8: Images and analysis showing the anisotropy of dragging when the fast axis is along the a axis and when it is along the b axis. **a,b:** Vortex motion when the fast scan is along \hat{x} (a) and \hat{y} (b) ($T = 20$ K, $z = 80$ nm, $F_{lat}^{max} \approx 20$ pN). Note the erratic nature of the motion and the abrupt snap-in to the tip on approaching the vortex along the slow axis, apparent as a sharp onset of the signal. Insets: Images of immobile vortices obtained with the same tip, scan height and scan directions at $T = 5.2$ K. **c,d:** Distance moved along the fast axis, w , measured near the maximum lateral force, versus scan angle measured from \hat{x} . Bars denote 70% confidence intervals. Dashed lines show the fit described in the text, with the oxygen vacancy cluster size $2R_b$ as a free parameter. Fit result: $2R_b/\xi_{ab} = 0.7$. In **c**, $T = 20$ K at $z = 80$ nm, 130 nm, 230 nm ($F_{lat}^{max} \approx 20, 15, 10$ pN, respectively). In **d**, $z = 80$ nm, for $T = 20, 15, 10$ K. **e:** Schematic diagram of vortex core meandering across the crystal in the presence of point defects clustered along the b axis.

energy per unit length is:

$$\sqrt{\langle \varepsilon_{pin}^2 \rangle} / L \approx U_{pin} \sqrt{n_i \xi_a \xi_b} / L \quad (2.7)$$

This energy is balanced against the elastic energy per unit length, $1/2\varepsilon_{\perp}(u/L)^2$, where u is the displacement of the tilted vortex from its non-tilted position and ε_{\perp} is the vortex line tension. We estimate L_c by identifying u with the typical scale of the fluctuations in the disorder.

When the vortex tilts at an azimuthal angle φ , we set $u = \xi(\zeta, \varphi) = \xi_{ab} \sqrt{\eta(\zeta, \varphi + \pi/2)}$. Optimizing L to minimize the free energy per unit length, $1/2\varepsilon_{\perp}(\zeta, \varphi)(\xi(\zeta, \varphi)/L)^2 - U_{pin} \sqrt{n_i \xi_{ab}^2} / L$, we obtain:

$$L_c(\zeta, \varphi) / L_c^0 = (\eta(\zeta, \varphi) \eta(\zeta, \varphi + \pi/2))^{2/3} \quad (2.8)$$

where $L_c^0 = \left(2\varepsilon_0 \varepsilon^2 \sqrt{\xi_{ab}^2 / n_i} / U_{pin}\right)^{2/3}$ is the result for a uniaxial superconductor [16]. Here we assume that even after it tilts, the vortex is nearly parallel to the c-axis. Each segment of length L_c is pinned with force up to F_p , which is given by:

$$F_p \approx \sqrt{\langle \varepsilon_{pin}^2 \rangle} / \xi(\zeta, \varphi). \quad (2.9)$$

Using Eq.2.8 and 2.9, we find $w(\zeta, \varphi) \propto \eta^{5/6}(\zeta, \varphi + \pi/2) / \eta^{2/3}(\zeta, \varphi)$. We use this expression to fit data in Fig. 2.8. The result, as well as the raw data, is presented in Fig. 2.9. We find that the angle between the a-axis and \hat{x} is $\varphi_0 = 6^\circ$, consistent with the sample-scan axes alignment we identify from vortex images. Fitting all five data sets, we find $\zeta = 1.6$, in clear disagreement with our direct measurement (Fig. 1.2 in page 9) and the known value, $\zeta = 1.3$ [6]. We surmise that there is an extra source of anisotropy.

A likely source for extra pinning anisotropy is nanoscale clustering of oxygen vacancies along the Cu-O chains (b -axis) [42] (Fig. 2.8e). We modified our model and take into account for the pinning correlation, which can be expressed as:

$$\langle U_{pin}(\vec{r}) U_{pin}(\vec{r}') \rangle \propto \delta(x - x') \frac{\pi^{-1} R_b}{(y - y')^2 + R_b^2} \delta(z - z'), \quad (2.10)$$

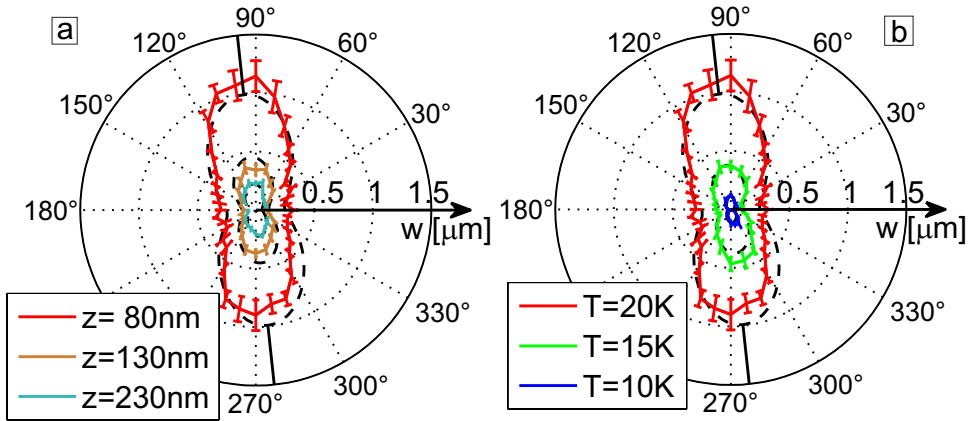


Figure 2.9: Distance moved, w , measured at the maximum lateral force, versus scan angle φ . Bars indicate 70% confidence intervals. Dashed lines show fit to the model, assuming no correlations in the pinning. For the fit we constrain the same ζ for all data sets. Additional parameters are an overall scale factor for each data set and the angle between \hat{y} and the b -axis, φ_0 . Fit results: $\zeta = 1.6$ and $\varphi_0 = 6^\circ$. The solid lines indicate the b -axis from the fit. **(a)** φ -dependence at $T = 20$ K as a function of scan height, which controls the magnitude of the force (for 80 nm, 130 nm, 230 nm: $F_{lat}^{max} \approx 20, 15, 10$ pN). **(b)** φ -dependence at scan height $z = 80$ nm, as a function of temperature.

in which R_b is a length scale that characterizes the correlation length of the disorder along the Cu-O chains. Assuming δT_c -disorder [16], $R_b \gg \xi_{ab}$ and using Eq. 2.10 we find the energy per unit length is given by Eq. 2.7 multiplied by an additional angle dependent factor:

$$\beta(\zeta, \varphi) \equiv \sqrt{\frac{\xi_b \arctan(\sin(\varphi)\xi(\zeta, \varphi)/R_b)}{\sin(\varphi)\xi(\zeta, \varphi)}} \quad (2.11)$$

This implies, using analysis similar to that leading to Eq. 2.8, that L_c attains an additional dependence on φ , with $\gamma(\zeta, \varphi) \equiv \eta^{1/6}(\zeta, \pi/2 + \varphi)/\beta^{2/3}(\zeta, \varphi)$, multiplying the right hand side of Eq. 2.8. As a result, there is an additional factor of $\gamma(\zeta, \varphi)$ dividing both F_p and k .

Using the modified model and imposing $\zeta = 1.3$, we fit the data in Fig. 2.8c,d for the cluster size R_b . We find clusters of order 10 vacancies along the Cu-O chains, large but reasonable for the sample's length of time at room temperature, where oxygen vacancies migrate slowly and cluster [43]. It is also possible that non-GL physics affects the core structure [44], changing details of the pinning-force anisotropy. These results demonstrate that single-vortex manipulation is a local probe of both the core and the defect structure on a scale down to the core size. For example, in samples without intrinsic $a - b$ anisotropy and with known defect structure, MFM could be used to probe the intrinsic structure of the vortex core itself.

2.3 Conclusion

Despite the fact that YBCO is one of the most studied superconductors, our data reveal major surprises about the behaviour of individual vortices. A strong dependence of the depinning force on temperature indicates that thermal effects play an important role, but existing models do not address the behavior of a well isolated vortex as it is individually manipulated. A model based on weak collective pinning for a single vortex quantitatively describes quasistatic aspects of vortex motion with the incorporation of anisotropy in the local microscopic pinning. This demonstrates that single vortex manipulation is a local probe of the structure of both the vortex and the pinning defects. Further work is required to describe the dynamic aspects of

individual vortex motion that we revealed: its stochastic nature and the marked effect of transverse wiggling. In particular: how do the dynamics alter the effective pinning landscape? How do they affect the mechanical properties? Practically, wiggling is an important tool for future experiments that require pulling vortices long distances, for example, in the study of vortex entanglement [29]. Our results show the utility of local force probes for accessing the pinning properties and mechanical behaviour of individual vortices, the collective behaviour of which is of great importance for the properties of superconductors.

Chapter 3

Magnetic force microscopy study of interlayer kinks in individual vortices in the underdoped cuprate superconductor $\text{YBa}_2\text{Cu}_3\text{O}_{6+x}$

Abstract We use magnetic force microscopy to both image and manipulate individual vortex lines threading single crystalline $\text{YBa}_2\text{Cu}_3\text{O}_{6.4}$, a layered superconductor. We find that when we pull the top of a pinned vortex, it may not tilt smoothly. Occasionally, we observe a vortex to break into discrete segments that can be described as short stacks of pancake vortices, similar to the “kinked” structure proposed by Benkraouda and Clem. Quantitative analysis gives an estimate of the pinning force and the coupling between the stacks. Our measurements highlight the discrete nature of stacks of pancake vortices in layered superconductors. The work described in the chapter appears in *Phys. Rev. B.* **79**, 214530 (2009).

3.1 Introduction

Magnetic field penetrates superconductors in the form of vortices, each carrying one magnetic flux quantum, $\Phi_0 \equiv h/2e$ (h is the Planck constant, $-e$ is the electron

charge). In highly anisotropic cuprates, where the c-axis penetration depth (λ_c) is much larger than the in-plane penetration depth (λ_{ab}), a vortex can be treated as a stack of two-dimensional, magnetically coupled, “pancake” vortices [45, 46], with weak interlayer Josephson coupling [47, 48]. Rich physics arises from the competition between thermal energy, vortex-vortex interactions, pinning, and interlayer coupling. While there are numerous studies on vortex-matter thermodynamics [16], work on individual vortices is scarce. Here we use a magnetic force microscope (MFM) to directly probe the pinning energy and interlayer coupling of an individual vortex, both of which determine its shape and the nature of its motion.

The “pancake” model is a well-accepted description for vortices in layered superconductors [16]. Many macroscopic measurements have confirmed this picture, e.g. by observing the loss of vortex line tension at high magnetic fields and elevated temperatures [49, 50]. On the single vortex level, Benkraouda and Clem proposed that sheared pancake vortices can break into separate straight stacks of pancakes to create a kinked structure instead of tilting [51] [Fig. 3.1(a)]. This “kinking” model has been used to explain magnetic features with sub- Φ_0 flux observed in images of individual vortices [52–54] and to study the interaction between pancake vortices and interlayer Josephson vortices [54, 55].

MFM has an important advantage over other magnetic imaging techniques in that it allows us to also manipulate individual vortices [56] with nanoscale control and a known force [37, 57]. Our previous work (ref.[57], presented in chapter 2) demonstrated that in an overdoped $\text{YBa}_2\text{Cu}_3\text{O}_{6.991}$ single crystal, a vortex follows the MFM tip as the tip moves back and forth over it and exhibits a marked enhancement of the motion perpendicular to this wiggling direction. In $\text{YBa}_2\text{Cu}_3\text{O}_{6.991}$ vortices behave like elastic strings rather than stacks of pancakes due to the moderate anisotropy ($\gamma \equiv \lambda_c^{T=0K}/\lambda_{ab}^{T=0K} \approx 5 - 7$)[16]. Here we need larger anisotropy because our goal is to provide a direct test for the “kinking” model and, by implication, for the discrete nature of pancake stacks. We therefore use a very underdoped $\text{YBa}_2\text{Cu}_3\text{O}_{6+x}$ (YBCO) single crystal, because it is known that reducing the doping increases the anisotropy [58] and decreases the interlayer coupling.

In the experiment we create and annihilate interlayer “kinks” with the MFM and

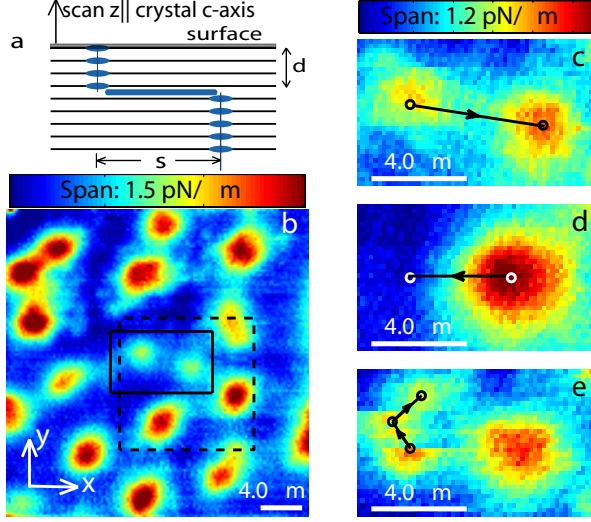


Figure 3.1: MFM images showing the annihilation and creation of kinked stacks of pancake vortices, which appear as pairs of sub- Φ_0 , isolated features. **(a)** Cartoon of a side view of a kinked pancake stack (ellipses), including the core of the vortex (vertical lines) and the interlayer Josephson vortex (thick blue line). d - depth of the kinked structure, s - lateral separation between the stacks. Also depicted are the CuO_2 layers (horizontal lines). **(b)** Initial configuration of vortices after field cooling from $T > T_C$ to $T = 5.4\text{K}$. Scan height $z = 1.05\mu\text{m}$. Most of the features in this scan are Φ_0 vortices. There are also what appear to be sub- Φ_0 features, referred as partial vortex stacks. The solid frame shows the scan area for Fig. 3.1(c)-(e) and highlights a pair of partial stacks. The dashed frame shows the scan area for Fig. 3.2. Also plotted are the scanning x , y axes. **(c-e)** Scans at $T = 12\text{K}$ of the two stacks in the solid frame in (b). The arrows show the tip path used for manipulation, as described in the text. (c) Scan before annihilation ($z = 0.93\mu\text{m}$), (d) scan after annihilation and before creation ($z = 1.24\mu\text{m}$) and (e) scan after creation ($z = 1.24\mu\text{m}$). In (e) the tip starts scanning from the bottom left corner and is incremented along $+\hat{y}$ after each raster period. The vortex stack on the left jumps as the tip scans over it. The dots and arrows show positions where the stack is trapped temporarily and the trajectory of its motion. Here, F_{lat} is much smaller than the force required to move a regular vortex, indicating an unstable stack configuration.

measure the coupling between pancake stacks. We first map the magnetic interaction of the MFM tip with the magnetic field from the sample. Occasionally we observe pairs of well separated features carrying sub- Φ_0 flux, similar to those interpreted in the past as kinked pancake stacks stabilized by local pinning [52]. We then use the MFM tip to combine these pairs of features to create regular Φ_0 vortices. Our success verifies the “kinking” model. As an even more stringent test, we split regular Φ_0 vortices by pulling them apart to create kinks. We determine the required force, which gives an estimate for the attractive interaction between pancake stacks. The result agrees well with the pancake model with dominant magnetic coupling augmented by the line-tension of the Josephson string connecting the stacks.

3.2 Sample and technique

The 100 μm thick platelet shaped crystal $\text{YBa}_2\text{Cu}_3\text{O}_{6+x}$ (0.7mm \times 0.7mm face \parallel crystal ab -plane) was grown by the self-flux method in BaZrO_3 crucibles [32], mechanically detwinned and annealed. $T_c = 21\text{K}$ (transition width $\Delta T_c \approx 2\text{K}$), implying $x \approx 0.4$ and thus $\lambda_{ab}^{T=0\text{K}} \approx 0.36 \mu\text{m}$ and anisotropy $\gamma \approx 75$ [59–61], comparable to $\text{Bi}_2\text{Sr}_2\text{CaCu}_2\text{O}_{8+x}$ ($\gamma \approx 60 - 250$) [16].

Our measurements were performed in a variable temperature MFM in frequency modulation mode [2]. In the experimental setup, a magnetic tip at the end of a flexible cantilever¹ faces the crystal a-b plane. The tip-sample force induces a shift of the cantilever’s resonant frequency f_0 , which we measure. The resonant frequency changes rapidly as the tip approaches the sample, giving precise determination of the tip-sample separation. In our scans, the tip moves at a constant height z above the surface ($\hat{z} \parallel$ crystal c -axis), back and forth along \hat{x} . Then, after one period of motion, which lasts a few seconds, it is incremented along $+\hat{y}$ or $-\hat{y}$. The choice of \hat{x} and \hat{y} are illustrated in [Fig. 3.1(b)]. Subtracting a z -dependent offset, we obtain the contribution to the frequency shift of the tip-vortex interaction, Δf , which gives information on the tip-vortex force, $\partial F_z / \partial z = -2k\Delta f / f_0$ ($f_0 = 59.040\text{kHz}$, the

¹We used a commercial cantilever NanosensorsTM SSS-QMFMR with tip radius of curvature $\approx 25 \text{ nm}$

cantilever spring constant $k = 2.7 \pm 0.1 \text{N/m}$ determined by Sader method [62]).

The force exerted by the tip on the sample is generally regarded as a drawback of MFM. Here, we magnetize the tip to give attractive tip-vortex force and use its lateral components, \vec{F}_{lat} , to overcome the pinning force, F_{pin} , to manipulate individual vortices. We tune $F_{lat} \equiv |\vec{F}_{lat}|$ by varying z . We first image at z where F_{lat} is insufficient to perturb the vortices, which are held static by F_{pin} . For manipulation, we reduce z to increase F_{lat} . When $F_{lat}^{\max}(z) > F_{pin}(T)$, where F_{lat}^{\max} indicates the maximum F_{lat} exerted during the scan, we can manipulate a vortex. Increasing temperature, which reduces $F_{pin}(T)$, gives extra control [37, 57], up to the temperature where the vortices run away.

3.3 Experiment and discussion

For low vortex density, we cool the sample in an applied magnetic field of $0.5 \cdot 10^{-4} \text{T}$ along the crystal's c -axis with the MFM tip retracted $100 \mu\text{m}$ from the sample surface (to minimize the chance of inducing vortices by the tip). Fig. 3.1(b) shows an image acquired at $T = 5.4 \text{K}$, in which vortices appear as peaks. Most vortices give the same peak height, as expected, since they each should carry a flux of exactly Φ_0 . However, some peaks have weaker amplitude and appear in pairs [e.g. Fig. 3.1(b), solid framed region], indicating the flux associated with each member is less than Φ_0 . Previous work suggests that these peaks originate from kinked stacks of pancake vortices forming one Φ_0 -vortex [52]. To test this model, we annihilate kinks and recreate them [Fig. 3.1(c)-(e)]. For the manipulation, we heat the sample to $T = 12 \text{K}$, reducing F_{pin} . Then, after locating two distinct partial stacks [Fig. 3.1(c)], we try to pull one towards the other with the tip. We repeat this until we succeed, reducing z for each new attempt (for driving to the starting position we retract the tip to reduce F_{lat}^{\max} , and with it the chance of accidental perturbation). We find that after we drag one vortex stack, it combines with its partner to form a Φ_0 -vortex with rotational symmetry, suggesting well aligned stacks [Fig. 3.1(d)]. As an additional test, we pull the vortex apart, without changing z and T , by moving the tip away from its center at \vec{R}_i [Fig. 3.1(d)] and successfully create two distinct stacks [Fig. 3.1(e)]. The newly

created partial stacks are not always stable, as signified by occasional vortex jumps [Fig. 3.1(e)].

We confirm that the two stacks we manipulate compose one vortex by fitting the pre-annihilation scan to a model [Fig. 3.2 (a),(b)]. The model is based on the fact that, for $z \gg \lambda_{ab}$, the magnetic field from a vortex stack is approximately equal to the field from a magnetic monopole λ_{ab} below the surface of the superconductor (filling the half space $z \leq 0$) [63]:

$$\vec{B} [\vec{R}, z] \approx \frac{\beta \Phi_0}{2\pi} \frac{(\vec{R} + (z + \lambda_{ab}) \hat{z})}{(R^2 + (z + \lambda_{ab})^2)^{3/2}}, \quad (3.1)$$

where \vec{R} is the in-plane position relative to the vortex center. For a regular Φ_0 vortex, $\beta = 1$. For a partial stack extending from depth d to the surface, $\beta = 1 - e^{-d/\lambda_{ab}}$. For a semi-infinite stack extending from d down: $\beta = e^{-d/\lambda_{ab}}$ [52]. We model our tip as a long narrow cylinder magnetized along its axis \hat{z} . The resulting force acting on the tip due to the interaction with the vortex is $\vec{F} [\vec{R}, z] \approx \tilde{m} \vec{B} [\vec{R}, z]$, where \tilde{m} is the dipole moment per unit length of the tip. The MFM signal from a collection of vortex stacks is then given by the ‘‘monopole-monopole’’ (m-m) model (introduced in Chapter 1):

$$\partial F_z / \partial z = \sum_i A_i \frac{1 - \frac{1}{2} (\vec{R} - \vec{R}_i)^2 / (z + h_0)^2}{\left[1 + (\vec{R} - \vec{R}_i)^2 / (z + h_0)^2 \right]^{5/2}} \quad (3.2)$$

where i enumerates the distinct vortex features in a scan, \vec{R} is the in-plane position of the tip, the peak amplitude for each feature is $A_i = \beta_i \tilde{m} \Phi_0 (z + h_0)^{-3} / \pi$ and $h_0 = \lambda_{ab} + d_{\text{offset}}$ (d_{offset} is the offset due to the tip geometry and any non-superconducting layer on the surface of the superconductor [57]). The fit in Fig. 3.2(b) using eq(1) gives $A_1 + A_2 \approx A_3$ implying $\beta_1 + \beta_2 = 1$ and confirming that two adjacent partial vortex stacks add up to one regular vortex. We want to point out that although the monopole model for the tip is a simplification, the details of the model are not important. As long as the model describes the data and extract the amplitude of each feature correctly, it leads to the same conclusion that the two partial stacks add

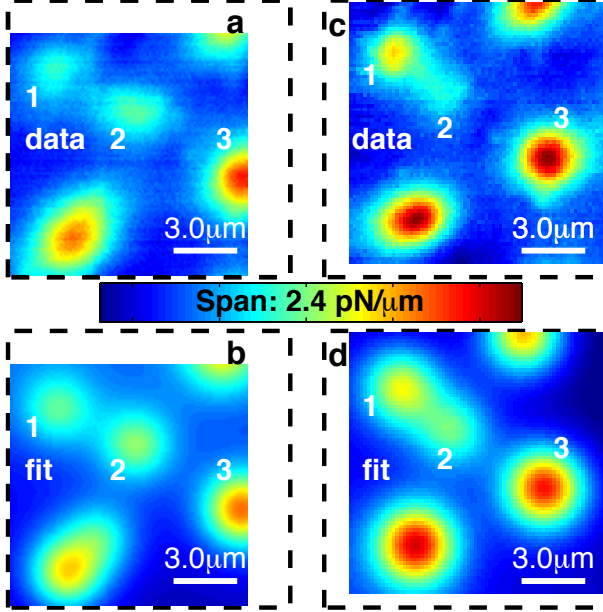


Figure 3.2: Scans (a,c) and fits (b,d) of vortices before and after manipulation. The dashed frames match the dashed frame in Fig. 3.1(a). **(a)** Scan at $T = 5.3\text{K}$, $z = 0.94\mu\text{m}$, of a field cooled vortex configuration. **(b)** Fit to scan in (a) using the m-m model. The fitted amplitudes, $A_1 = 0.69 \pm 0.01\text{pN}/\mu\text{m}$, $A_2 = 0.86 \pm 0.01\text{pN}/\mu\text{m}$, $A_3 = 1.55 \pm 0.01\text{pN}/\mu\text{m}$ (errors denote 95% confidence intervals), give $A_1 + A_2 \approx A_3$. For pair 1-2 the fit gives $d = 0.6\lambda_{ab}$ and $s = 4.1\mu\text{m}$. **(c)** Scan at $T = 5.3\text{K}$, $z = 0.84\mu\text{m}$, after combining and re-separating features 1 and 2. Both the signal strength and the separation between the two stacks change because of the manipulation. **(d)** Fit to scan in (c). Fitted amplitudes: $A_1 = 1.28 \pm 0.03\text{pN}/\mu\text{m}$, $A_2 = 0.94 \pm 0.03\text{pN}/\mu\text{m}$, $A_3 = 2.00 \pm 0.02\text{pN}/\mu\text{m}$. As in (b), $A_1 + A_2 \approx A_3$. For this pair: $d = 0.9\lambda_{ab}$, $s = 3.2\mu\text{m}$.

up to be one regular vortex.

Other experimental observations provide further insight about the kinked stacks. When we recombine and re-separate the same pair of stacks repeatedly, we can only manipulate one member. Presumably, this stack is the finite top stack. Furthermore, both the separation between the stacks and the signal amplitudes change in the annihilation-creation process (e.g. Fig. 3.2), indicating different kink structures. This result shows that pinning is important and that the tip allows the dragged pancakes to explore the pinning environment. Finally, partial pairs are rare [only one in Fig. 3.1(b)]. However, most other vortices have irregular shape, which we believe is due to misalignment of the pancakes, too small to be resolved because of the relatively large λ_{ab} . This irregularity tends to diminish after dragging, in support of the picture that pinning hinders pancake stacks from aligning.

We next determine the coupling between stacks in a vortex from the force required to create a kink (Fig. 3.3). For that, we move the tip repeatedly along a line away from a regular vortex, reducing z for each new line-scan [Fig. 3.3(d)]. We estimate F_{lat} from the m-m model (Fig. 3.4). For large z , the vortex remains unperturbed, implying $F_{lat}^{\max}(z) < F_{pin}(T)$. We estimate $F_{pin}(T)$ from the largest z at which we observe vortex motion, manifested by discontinuities in the line scan larger than the noise level ($\approx 0.05\text{pN}/\mu\text{m}$) (We interpret features that are continuous as either topography or vortices). For example, at $T = 10\text{K}$ we observe first motion at $z = 0.36\mu\text{m}$, giving $F_{pin}(T = 10\text{K}) \approx F_{lat}^{\max}(z = 0.36\mu\text{m}) \approx 1.2\text{pN}$. For lower scans (e.g. $z = 0.24\mu\text{m}$), the tip drags part of the vortex to a new position, creating two distinct stacks [Fig. 3.3(b)]. In order to pull a vortex apart, F_{lat} has to overcome both F_{pin} and the restoring force F_{el} , which binds the two partial stacks together. At a position where a partial stack stops following the tip, $F_{lat}^{\max} \approx F_{pin} + F_{el}$. Thus, the measured restoring force is $F_{lat}^{\max}(z = 0.24\mu\text{m}) - F_{lat}^{\max}(z = 0.36\mu\text{m})$, giving $F_{el} \approx 0.1\text{pN}$ for $s = 3.3\mu\text{m}$, as identified by fitting Fig. 3.3(b) to the m-m model.

The restoring force, F_{el} , has two attractive contributions: the magnetic coupling between pancakes in different layers and the Josephson-string line-tension. The former is obtained by summing over the magnetic interactions between all the pancakes in the two partial stacks. Benkraouda and Clem (BC) [51] calculated this force for two

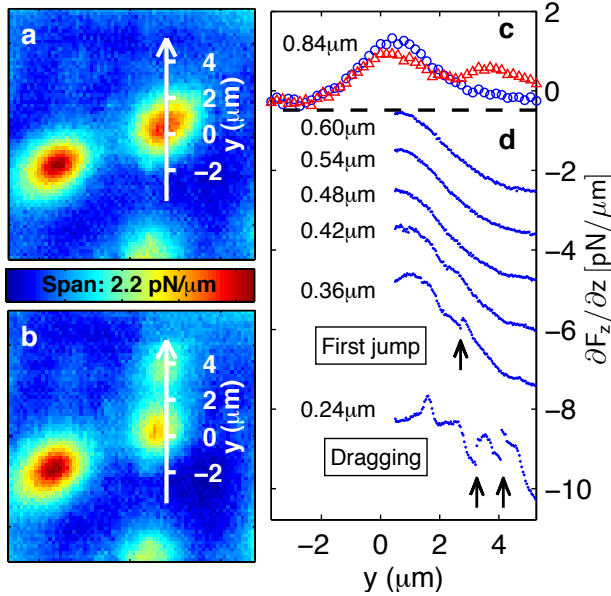


Figure 3.3: Creating kinks in a straight stack. **(a)** Image of two regular, field cooled, vortices at $T = 5.3\text{K}$ ($z = 0.80\mu\text{m}$). The white line marks the location of the line-cut plotted in (c) and the path for the line-scans in (d). **(b)** Image of a regular vortex [the one on the left in (a)] and the newly created kinked-stack pair, created by the sequence of line scans in (d). The white line is the same as in (a). Scan at $T = 5.3\text{K}$, $z = 0.80\mu\text{m}$. **(c)** Circles and triangles show points extracted along the white line in (a) and (b), respectively. **(d)** Line scans acquired with the tip moving over the white lines in (a) and (b) starting from $y = 0$ ($T = 12\text{K}$). $z = 0.60, 0.54, 0.48, 0.42\mu\text{m}$: the vortex is stationary at approximately $y = 0$, with the signal dropping as the tip moves away. $z = 0.36\mu\text{m}$: the vortex jumps towards the tip for the first time (tip position when this happens is marked by an arrow, roughly when the lateral force peaks (Fig. 3.4)), as indicated by the abrupt signal increase due to the increased tip-vortex interaction. $z = 0.24\mu\text{m}$: the vortex is dragged by the tip. The arrows highlight the discontinuities of the trace due to vortex motion. We believe that other sharp features in the trace originate from bumps on the surface which would deflect the tip as we further lowered the scan height.

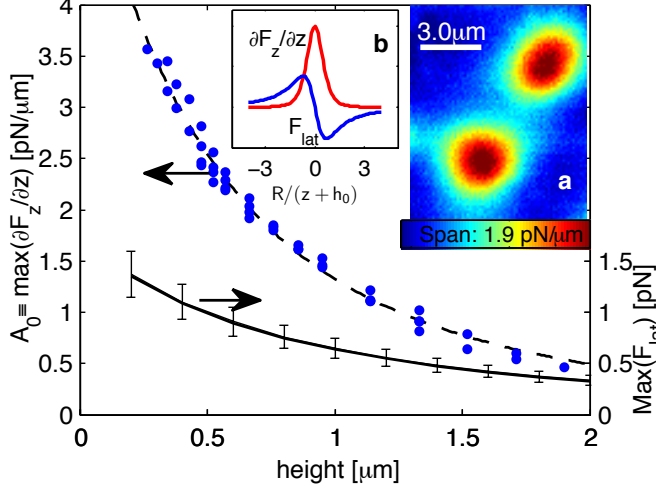


Figure 3.4: Calibration of the tip to extract $F_{lat}^{\max}(z)$, the maximum lateral force exerted on a vortex during a scan at height z . At each z we acquire a scan of two immobile vortices at $T = 5.0\text{K}$ [insert (a) – an example for $z = 0.85\mu\text{m}$]. We fit each scan to the m-m model and plot the peak amplitude, $A_0 \equiv \max(\partial F_z/\partial z)$ (main panel, left ordinate). We then fit the result to $(\tilde{m}\Phi_0/\pi)/(z+h_0)^3$, the dependence of the peak height on z in the model (dashed line). The fit yields $\tilde{m} = 22 \pm 3\text{nA}\cdot\text{m}$ and $h_0 = 1.55 \pm 0.10\mu\text{m}$. Within the model $F_{lat}^{\max} = (\tilde{m}\Phi_0/3\sqrt{3}\pi)/(z+h_0)^2$ (solid line, right ordinate). Error bars show the 95% confidence interval from the fit parameter uncertainty. The change of F_{lat}^{\max} due to the choice of different tip models is well within the error bars. Note that we perform the manipulation at elevated temperature (e.g. $T = 10\text{K}$ for Fig. 3.3), which leads to an additional 10% systematic error in F_{lat}^{\max} , due to the increase of λ_{ab} [59]. Insert (b) shows $\partial F_z/\partial z$ and F_{lat} in the model as a function of R in units of $(z+h_0)$. Note that $F_{lat}(0) = 0$ and reaches F_{lat}^{\max} at $R = (z+h_0)/\sqrt{2}$, roughly when $\partial F_z/\partial z = \max(\partial F_z/\partial z)/2$.

stacks of equal length, long on the scale of λ_{ab} . In our case, the length of the top stack, d , is of order λ_{ab} . For $s \gg \lambda_{ab}$ we obtain the BC result, suppressed by a factor of approximately $1 - e^{-d/\lambda_{ab}}$, to give:

$$F_{\text{mag}}(s) = -\partial E_{\text{mag}}/\partial s \approx (\Phi_0/4\pi\lambda_{ab})^2 [\lambda_{ab}/s - e^{-s/\lambda_{ab}}(1 + \lambda_{ab}/s)] [1 - e^{-d/\lambda_{ab}}]. \quad (3.3)$$

The line tension of a Josephson string for $\lambda_{ab} < s < \lambda_c$ is [47]:

$$F_J = -\partial E_J/\partial s \approx (\Phi_0/4\pi)^2 (\lambda_{ab}\lambda_c)^{-1}. \quad (3.4)$$

Given $\lambda_{ab} = 0.40\mu\text{m}$ and $\lambda_c = 31.6\mu\text{m}$ at $T = 10\text{K}$ [59, 60], $s = 3.3\mu\text{m}$ and $d = 0.5\lambda_{ab}$ [from fitting Fig. 3.3(b)], we find $F_{\text{mag}} = 0.09\text{pN}$ and $F_J \approx 0.02\text{pN}$. Adding the two gives $F_{\text{tot}} = F_J + F_{\text{mag}} = 0.11\text{pN}$, in good agreement with our estimate from the measurement.

3.4 Conclusions

We manipulated 20 vortices in different cooldowns all at temperatures around $T_c/2$. For each cycle, we warmed the sample to $T > T_C$ and then field cooled, sometimes changing the magnetic fields slightly, to get a different initial vortex configuration. We successfully created and observed the kinked structure in two vortices. In the remaining cases we could drag the top of the vortex but did not observe kinking. This is not unexpected: by MFM we can only manipulate pancakes that lie at most a few λ_{ab} beneath the surface because of the exponential suppression of F_{lat} . Imaging depth is also limited, because the resolution is set by $z + h_0$ ², the scale on which the magnetic field from a stack decays. The low rate of creating observable kinks in the limited volume defined by d and s (10%) and of observing field-cooled partial stacks (one pair in 3 thermal-cycles) reasserts that the balance between local pinning and F_{el} is crucial for determining the alignment of the pancakes composing one vortex. It

²we happen to have micron-size h_0 in this run mostly from the sample nonsuperconducting layer, which developed as a result of extensive surface cleaning due to silver epoxy contamination. Usually on fresh samples, h_0 is a few hundreds of nm.

also suggests that although the distribution of pinning sites has spatial variation, it is not strongly inhomogeneous.

By using MFM for imaging and manipulation, we probe the force required to separate individual vortices into pancake stacks in a highly anisotropic superconductor, and find that the interaction between pancake stacks in a single vortex is dominated by magnetic coupling. Our experiment directly measures the line energy and the pinning force of a single vortex, which, in competition with thermal energy and vortex-vortex interactions, determine the properties of vortex matter. The fact that it can be energetically cheap to form interlayer Josephson vortices in the presence of pinning implies that such vortices are less likely to entangle. Our technique of manipulating individual vortices by MFM combined with quantitative force analysis opens unique possibilities to study interacting many-body systems [64], as well as to address open questions in vortex matter, e.g, testing vortex entanglement and measuring the cutting barrier for vortices by deliberately winding one vortex around another and determining the required force [29, 65].

Chapter 4

Determining the penetration depth λ by Meissner repulsion

4.1 Introduction

The magnetic penetration depth λ , the length scale for supercurrent to screen external magnetic field, is one of the two fundamental length scales in superconductors [66]. It is determined by the superfluid density, which is related to the number of electrons in the superconducting state. The accurate determination of λ and its temperature variation $\Delta\lambda(T) \equiv \lambda(T) - \lambda(0)$ is crucial for understanding the fundamentals of the superconducting state, such as the gap structure [67, 68], the underlying pairing mechanism and the phase stiffness of the superconductivity [69]. However, the absolute value of λ is notoriously difficult to measure, especially in samples that may have either intrinsic or extrinsic inhomogeneity.

There are only a handful methods to measure λ and each has pitfalls that people performing the measurements are well aware of. For example, μ SR measurements take the assumption that vortices form Abrikosov lattice [70], which is not valid in many cases and can lead to significant errors [71]. To obtain λ from lower critical field measurement, one has to carefully polish the sample in order to get rid of the surface barrier and to accurately determine the demagnetization factor according to the sample shape [61]. Bulk measurements by microwave- and RF-based techniques are

made difficult by complex sample topography and inhomogeneity and give different results on nominally identical samples [72].

Efforts to measure λ by magnetic scanning probes include scanning SQUID susceptometry [73], mostly limited by the accuracy in determining the sensor-sample separation z , and magnetic force microscopy (MFM) by imaging individual vortices [74, 75]. The quantitative determination of λ from vortex images is highly non-trivial due to the convolution with the tip structure, which requires numerically calculating the convoluted signal based on detailed knowledge of the tip magnetic structure [75].

We resolve the difficulty of complex tip geometry by measuring the height dependence of the diamagnetic response in the Meissner state. The diamagnetic response is not as badly affected by the finite tip width as lateral imaging, allowing us to make approximations that give an analytical description justified for similar tips. In this chapter, I discuss the model for extracting λ and lay out the approximations. I also demonstrate on two $\text{YBa}_2\text{Cu}_3\text{O}_{6+x}$ (YBCO) single crystals that the values we obtained with two different tips both agree well with previously published results.

4.2 Sample and technique

We use high resolution cantilevers (NC-18 from Mikro-Masch), and coat half of the tip (a sharp pyramid about $30\ \mu\text{m}$ high) with an $40\ \text{nm}$ thick iron film by evaporating along the direction of the cantilever.

The YBCO single crystals were grown by the self-flux method in BaZrO_3 crucibles [32] and annealed, with superconducting transition temperature $T_c \approx 56\ \text{K}$, implying $x \approx 0.56$. The samples are platelet shaped, with the face parallel to crystal ab -plane about $1\text{mm} \times 0.7\text{mm}$ and thickness $60\text{-}80\ \mu\text{m}$. The samples were kept for less than two months after growth either in room temperature desiccator or below $77\ \text{K}$ ensuring that they were fresh. Sample I is fully detwinned, and sample II has twin boundaries separated by a few microns.

Although λ is difficult to measure accurately, people have done careful measurement by most of the available techniques on similar $\text{YBa}_2\text{Cu}_3\text{O}_{6+x}$ single crystals. All the techniques are expected to have 10% systematic error or more and all the results

Table 4.1: reference of λ measurements in $\text{YBa}_2\text{Cu}_3\text{O}_{6+x}$ ($x \approx 0.56$) ortho-II crystals. $T_{measure}$ is the T at which λ is measured.

method	λ [nm]	$T_{measure}$ [K]	T_c [K]	reference
μsR	$\lambda_{ab} = 175$	1.25	59	Sonier <i>et al</i> , Ref [76]
lower critical field	$\lambda_{ab} = 175 \pm 6$	0	56	Liang <i>et al</i> , Ref [61]
ESR (Gd-doped)	$\lambda_a = 202 \pm 22$ $\lambda_b = 140 \pm 28$	0	56	Pereg-Barnea <i>et al</i> , Ref [6]
Infrared spectroscopy	$\lambda_a = 248$ $\lambda_b = 183$	12	59	Homes <i>et al</i> , Ref [77]

in table 4.1 agree within the error range. These samples are good candidates for us to calibrate measurement of the absolute value of λ .

4.3 Model the Meissner response

To obtain λ , we cool the samples in the absence of magnetic field and measure $\partial F_z / \partial z(z)$.

In the Meissner state, the MFM tip experiences repulsion from the superconductor. The levitation force depends on the shape and magnetic moment of the tip, its separation from the surface z , as well as the London penetration depth λ . To calculate the force, we start from a point dipole placed above a isotropic type-II superconductor and integrated over the tip, as calculated by J.H. Xu (Ref. [78]):

$$F(z) = \frac{\mu_0}{4\pi} \int_0^\infty dk k^3 G(\lambda k) e^{-2zk} \int_{\text{tip}} d\mathbf{r}' \int_{\text{tip}} d\mathbf{r}'' M(\mathbf{r}') M(\mathbf{r}'') e^{-k(z'+z'')} J_0(k|\mathbf{R}' - \mathbf{R}''|),$$

Our MFM measures the vertical derivative of $F(z)$:

$$\partial F_z / \partial z(z) = -\frac{\mu_0}{2\pi} \int_0^\infty dk k^4 G(\lambda k) e^{-2zk} \int_{\text{tip}} d\mathbf{r}' \int_{\text{tip}} d\mathbf{r}'' M(\mathbf{r}') M(\mathbf{r}'') e^{-k(z'+z'')} J_0(k|\mathbf{R}' - \mathbf{R}''|) \quad (4.1)$$

where we assumed that the tip was magnetized along the z-direction and used $\mathbf{r} =$

$\mathbf{R} + z\hat{z}$, $\mathbf{R} = R\hat{R}$ and

$$G(x) = \frac{\sqrt{1+x^2} - x}{\sqrt{1+x^2} + x} \sim e^{-2x} \left(1 + \frac{x^3}{3} - \frac{3x^5}{20} + O[x]^6 \right) \quad \text{for } x \ll 1. \quad (4.2)$$

Approximating $G(\lambda k)$ by $e^{-2\lambda k}$ is equivalent to replacing the response of the superconductor by an image of the field source mirrored through a plane λ below the superconducting surface (illustrated in Fig. 4.1(a)). Under this time-reversed mirror approximation, the change in λ is nearly equivalent to change in z , allowing us to determine $\Delta\lambda(T) \equiv \lambda(T) - \lambda(6K)$ independent of any model of the sensor structure [73, 79]. We obtain from sample II $\Delta\lambda(T)$ consistent with linear T dependence (Fig. 4.1(b)), as expected from the nodal d-wave gap structure of YBCO [67].

4.3.1 Truncated cone model

To extract λ , we model the tip as a sharp, single-domain conical shell truncated at the distance h_0 . $M(\mathbf{r}) = mt\delta(R - \alpha(z + h_0))$, where we assume \vec{M} is along \hat{z} , $\alpha \approx 15^\circ$ is the cone angle, t is the magnetic film thickness, m is the magnetization, and h_0 is the truncation height. From Eq. 4.5 we start the integrals over z' and z'' at h_0 , and replace z by $z - h_0$. In the limit of $\alpha \ll 1$, k is bounded from above and $J_0(k|\mathbf{R} - \mathbf{R}'|) \approx J_0(0)$. We then perform the z integrals and the θ integrals to get:

$$\partial F_z / \partial z(z) = -\frac{\mu_0}{2\pi} (\alpha mt)^2 \int_0^\infty dk k^4 G(k\lambda) e^{-2(z-h_0)k} \left(\int_{\theta_1}^{\theta_2} d\theta' \int_{h_0}^\infty dz' z' e^{-kz'} \right)^2$$

The θ integral just gives $\theta_2 - \theta_1 \equiv \Delta\theta$ and the z integral gives $k^{-2} e^{-h_0 k} (1 + h_0 k)$. We get

$$\partial F_z / \partial z(z) = -\frac{\mu_0}{2\pi} (\alpha mt \Delta\theta)^2 \int_0^\infty dk (1 + h_0 k)^2 e^{-2h_0 k} G(k\lambda) e^{-2(z-h_0)k}$$

For $z \gg \lambda$, we get:

$$\partial F_z / \partial z(z) = -\frac{\mu_0}{2\pi} \frac{(\alpha mt \Delta\theta)^2}{z + \lambda} \left[1 + \frac{h_0}{z + \lambda} + \frac{h_0^2}{2(z + \lambda)^2} \right] \quad (4.3)$$

To describe touchdown curves at various temperatures, we use

$$\partial F_z/\partial z(z) - \partial F_z/\partial z(z, T)|_{z=\infty} = \frac{A}{z + \lambda} \left[1 + \frac{h_0}{z + \lambda} + \frac{h_0^2}{2(z + \lambda)^2} \right] \quad (4.4)$$

where $\partial F_z/\partial z(z, T)|_{z=\infty}$ contains the shift of the cantilever's resonant frequency with temperature, $A \equiv -\mu_0(\alpha mt \Delta\theta)^2/2\pi$ and $\Delta\theta \equiv \theta_2 - \theta_1 = \pi$ for our half-coated tips. Since m and t may not be known exactly we take A as a fitting parameter.

4.4 Results and error analysis

We fit touchdown curves in Fig. 4.1(a) using Eq. 4.4, fixing h_0 from scanning electron microscopy images of the tip (Fig. 4.2) and let A , λ and $\partial F_z/\partial z|_{z=\infty}$ to vary. In the fit, we minimize $\chi^2 \equiv \sum (1 - \partial F_z/\partial z(z)_{data}/\partial F_z/\partial z(z)_{fit})^2$ for $z \geq 0.6\mu\text{m}$. We obtain $\lambda(6K) = 185$ nm and 196 nm in sample I and sample II respectively. Extrapolating using $\Delta\lambda(T)/T = 0.97$ nm/K as we measure (Fig. 4.1(b)), we obtain $\lambda(0) = 180$ and 190 nm, in good agreement with previous reported values $\lambda(0) = 180 \pm 20$ nm on similar crystals nm by a few techniques [6, 34, 76, 77] as summarized in Table 4.1.

How accurate is the measurement of λ ? Using the measurement on sample II as an example, if we consider only statistical errors, we obtain $\lambda_{ab}(6K) = 196 \pm 3$ nm from bootstrapping [80] with 70% confidence interval.

The systematic errors mainly come from the uncertainty in determining h_0 and z , and the approximation made in the model. The ± 20 nm uncertainty on h_0 leads to ± 14 nm uncertainty in λ . We detect the surface within ± 5 nm owing to the abrupt change of $\partial F_z/\partial z$ when van der Waals force dominates over the magnetic force (Fig. 4.1(a)). We calibrate the scanner using the laser interference pattern from the sample, which gives at most 3% error in determining z mostly due to the nonlinearity of the scanner. We choose to measure fresh surfaces because any non-superconducting layer makes the measured λ larger than the real value by the thickness of the layer.

We observe no change in the tip magnetic strength before and after ramping the magnetic field to 0.1 T at 30 K, consistent with the tip being mono-domain. The magnetization of the tip is presumably aligned along the film. Assuming \vec{M} along z

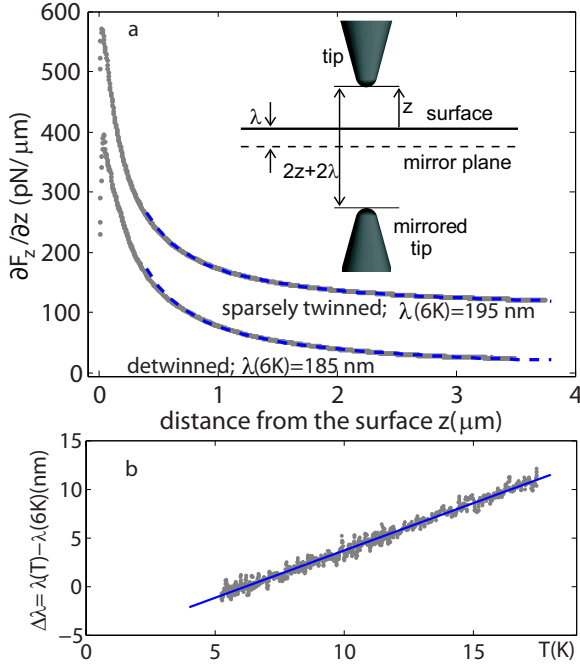


Figure 4.1: Measuring λ and $\Delta\lambda$ by MFM in the Meissner state using time-reversed mirror approximation. **a:** z dependence of $\partial F_z/\partial z$ (grey dots) by MFM at $T = 6$ K on two YBCO single crystals ($T_c \approx 56$ K) and the fit to the truncated cone model (dashed line) from which we extract λ as a fit parameter. The vertical offset, $\partial F_z/\partial z|_{z=\infty}$ is 0 and 100 pN/ μm respectively. Inset plots the sketch showing the time-reversed mirror approximation: the response of the superconductor can be replaced by an imaged tip reflected over a plane λ below the superconducting surface. **b:** $\Delta\lambda(T) \equiv \lambda(T) - \lambda(6\text{K})$ of sample II (grey dots) from $T=5$ K to 12 K determined independently of the tip model. The linear fit (solid line) shows a slope of 0.97 nm/K.

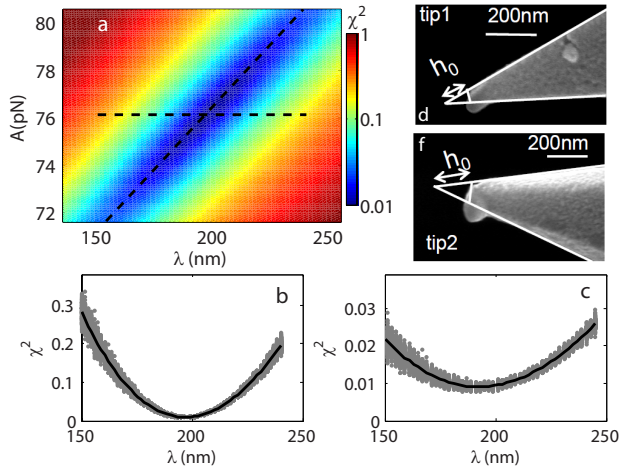


Figure 4.2: **a-c**: Fit quality χ^2 for the fit in Fig. 4.1(a) for sample II. **a**: χ^2 plotted as the color scale in the two-dimensional parameter space of A and λ with $\partial F_z / \partial z$ optimized at each point. **b-c**: χ^2 as a function of λ when A is fixed (**b**) at the value that minimizes χ^2 as plotted by the horizontal dashed line in (a), and when A is free floating (**c**) as given by the diagonal dashed line in (a). The distribution of χ^2 (grey dots) are from bootstrapping 200 times. **d-f**: Scanning electron microscopy images of tip 1 (d) used for sample I and tip 2 (f) used for sample II, from which we determine $h_0 = 120 \pm 20$ nm and 160 ± 20 nm respectively. The curvature at the tip apex comes from extra deposition of materials due to a sharp edge.

does not induce systematic error in λ because the in-plane component gives the same functional dependence of $\partial F_z/\partial z$ as the z component.

We neglect the tip width in the model by assuming the tip is infinitely narrow. To estimate the correction from finite tip width, we release this approximation by taking the Bessel Function in Eq. 4.5 to the second order: $J_0(x) = 1 - 1/4x^2 + O(x^4)$. In this case, Eq. 4.5 can be approximated by:

$$\begin{aligned} \frac{\partial F_z}{\partial z}(z) &= -\frac{\mu_0}{2\pi}(\alpha mt)^2 \int_0^\infty dk k^4 G(k\lambda) e^{-2zk} \times \\ &\int d\theta' d\theta'' dz' dz'' z' z'' e^{-k(z'+z'')} \left(1 - \frac{1}{4}\alpha^2 k^2 (z'^2 + z''^2 - 2z'z'' \cos(\theta' - \theta'')) \right) \end{aligned}$$

Working out the integral, we get the correction to be:

$$\begin{aligned} \partial F_z/\partial z(z)_{corr} &= -\frac{\mu_0}{2\pi}(\alpha mt \Delta\theta)^2 \alpha^2 \left[\left(\frac{3}{2(z+\lambda)} + \frac{3h_0}{2(z+\lambda)^2} + \frac{9h_0^2}{8(z+\lambda)^3} \right) \right. \\ &+ 4 \left(\frac{\sin \Delta\theta/2}{\Delta\theta} \right)^2 \left(\frac{1}{(z+\lambda)} + \frac{h_0}{(z+\lambda)^2} + \frac{h_0^2}{(z+\lambda)^3} \right) \left. \right] + O\left(\frac{h_0}{z+\lambda}\right)^4 \\ &\approx A\alpha^2 \left(\frac{3}{2} + \frac{4}{\pi^2} \right) \left(\frac{1}{z+\lambda} + \frac{h_0}{(z+\lambda)^2} + \frac{h_0^2}{2(z+\lambda)^3} \right) + A\alpha^2 \left(\frac{3}{8} + \frac{2}{\pi^2} \right) \frac{h_0^2}{(z+\lambda)^3} \end{aligned}$$

Note that the first term on the right hand side on the last line have the same functional form as the model in Eq. 4.4. Therefore, only the second term leads to error in λ , which is at most 2% owing to the small value of α . We have performed numerical simulations of a truncated cone tip with realistic width, which quantitatively confirms the analytical model of Eq. 4.4. When $h_0 = 0$ (sharp cone), this is no correction associated with finite tip width, consistent with the analysis in the sharp cone model.

Adding all the errors, we obtain $\lambda(0) = 190 \pm 25$ nm for sample II. The same analysis on sample I gives $\lambda(0) = 180 \pm 30$ nm.

In YBCO crystals, λ along the crystal a and b axes are not equal, and we measure the average $\lambda_{ab} \equiv \sqrt{\lambda_a \lambda_b}$. When pinning is weak, we can determine λ_a/λ_b by resolving the positions of individual field-cooled vortices. As shown in Fig.1.2 in page 9, the Fourier transform of the positions of field cooled vortices in fully doped $\text{YBa}_2\text{Cu}_3\text{O}_{7-\delta}$ ($\delta = 0.01$) gives an elliptic band, the eccentricity of which gives λ_a/λ_b [57]. However,

such measurement requires the vortex-vortex interaction to overcome pinning, which may often not be satisfied [79].

To summarize, we demonstrate a method to measure λ within 15% error by MFM from the height dependence of the diamagnetic response. The essential elements of the method are the precise height determination, and modeling the diamagnetic response with a small number of parameters.

4.5 Additional discussions of the model

4.5.1 Sharp cone model

The sharp cone model is a special case of the truncated cone model at $h_0 = 0$: $M(R, z) = mt\delta(R - \alpha z)$. We also assume that the axis of symmetry of the cone is normal to the cantilever surface and parallel to the scan z-axis, and that the tip is magnetized along the z-axis. Plug $M(R, z)$ to Eq. 4.1, we obtain:

$$\frac{\partial F_z}{\partial z}(z) = -\frac{\mu_0}{2\pi}(\alpha mt)^2 \int_0^\infty dk k^4 G(k\lambda) e^{-2zk} \times \int d\theta d\theta' dz' dz'' z' z'' e^{-k(z'+z'')} J_0\left(\alpha k \sqrt{z'^2 + z''^2 - 2z'z'' \cos(\theta' - \theta'')}\right) \quad (4.5)$$

where the θ integrals are over a range θ_1 to θ_2 and the z integrals run from the bottom of the cone $z = 0$ to its full height, which we take as infinite. We can perform the z -integrals in polar coordinates. We find:

$$\frac{\partial F_z}{\partial z}(z) = -\frac{\mu_0}{2\pi}(\alpha mt)^2 \int_0^\infty dk k^4 G(k\lambda) e^{-2zk} \times \int d\theta d\theta' \int_0^{\pi/2} d\phi \int_0^\infty d\zeta \zeta^3 \frac{\sin 2\phi}{2} e^{-k(\sin\phi + \cos\phi)\zeta} J_0(\alpha k \zeta \sqrt{1 - \sin 2\phi \cos(\theta' - \theta'')}) \quad (4.6)$$

Changing coordinates to $\bar{\zeta} = k\zeta$ we find:

$$\frac{\partial F_z}{\partial z}(z) = -\frac{\mu_0}{2\pi}(\alpha mt)^2 \int_0^\infty dk G(k\lambda) e^{-2zk} C.$$

Where C is a dimensionless number given by:

$$C \equiv \int d\theta' d\theta'' \int_0^{\pi/2} d\phi \int_0^\infty d\bar{\zeta} \bar{\zeta}^3 \frac{\sin 2\phi}{2} e^{-(\sin\phi + \cos\phi)\bar{\zeta}} J_0(\alpha\bar{\zeta}\sqrt{1 - \sin 2\phi \cos(\theta' - \theta'')})$$

Going back to Eq. 4.6, we note as long as the time-reversed mirror approximation is valid, we get

$$\partial F_z / \partial z(z, T) - \partial F_z / \partial z(z, T)|_{z=\infty} = \frac{A_{CM}}{z + \lambda} \quad (4.7)$$

This simple z dependent is not affected by the tip width at all. Neither is it affected by $\Delta\theta$ being another value rather than π or 2π . Eq. 4.7 is also consistent with the sharp cone model being a special case of the truncated cone model at $h_0 = 0$.

4.5.2 Other approximations of the truncated cone model

Dipole at the tip apex The tip apex is approximated as the truncation face in the model. Very often, we find a magnetic half-dome, or a magnetic sphere, with the diameter about 50 nm at the tip apex. To account for its contribution, we add a dipole at the end of the truncated cone. The magnetic moment of the dipole can be along an arbitrary direction. Here we choose it to along z as an example and the conclusion does not depend on this choice. The signal is given by:

$$\partial F_z / \partial z(z) = -\frac{\mu_0}{2\pi} (mt)^2 \int_0^\infty dk k^4 G(k\lambda) e^{-2(z-h_0)k} \left(\int_{\theta_1}^{\theta_2} d\theta' \int_{h_0}^\infty dz' (\alpha z' + \beta \delta(z - \epsilon) e^{-kz'}) \right)^2$$

where β characterizes the magnetic moment of the dipole and ϵ is its offset from the truncation height. We take $\epsilon = 0$ to simplify the expressions and to not introduce more parameters since ϵ is the smallest scale in the problem. It gives

$$\begin{aligned} \partial F_z / \partial z(z) = & -\frac{\mu_0}{2\pi} (\alpha mt \Delta\theta)^2 \left(\left(\frac{1}{z + \lambda} + \frac{h_0}{(z + \lambda)^2} + \frac{h_0^2}{2(z + \lambda)^3} \right) \right. \\ & \left. + \frac{1}{2} \frac{\beta}{\alpha} \left(\frac{1}{(z + \lambda)^3} + \frac{3h_0}{2(z + \lambda)^4} \right) + \left(\frac{\beta}{\alpha} \right)^2 \frac{3}{4(z + \lambda)^5} \right) \end{aligned} \quad (4.8)$$

This correction adds two terms to the truncated cone model (first term): the dipole-cone interaction and (second term) the dipole-dipole interaction (third term). Fitting Eq. 4.8 to the touchdown curves, we get $\beta = 0$ and the same λ as using the truncated cone model. Note changing ϵ does not change the functional dependence but only adds another constant. This result means the dipole correction for the tip apex is not important.

In-plane magnetic moment of the tip In the model, we neglect the small in-plane magnetic moment of the tip, which comes from the 5^0 - 10^0 alignment angle relative to the normal direction of the crystal surface. The potential of a point dipole \vec{m} with the magnetic moment along arbitrary direction is given as Eq 30 in Ref [81]. when $\vec{m} = m \cos \eta \hat{z} + m \sin \eta \hat{x}$, the response potential is

$$\varphi^r(k) = G(\lambda k)\varphi^s(k) = 2\pi G(\lambda k)e^{-kz'}e^{-i\vec{k}\cdot\vec{r}'}m(\cos \eta + i \sin \eta \cos(\theta_k - \phi))$$

where θ_k and ϕ are the polar angle of \vec{k} and \vec{m} . The magnetic energy of a tip with its apex at $(0,0,a)$ is the result of integrating over all the dipoles composing the tip:

$$\begin{aligned} U &= -\frac{1}{2} \int_{tip} \vec{M} \cdot \vec{h}^r \\ &= \frac{1}{4\pi} \int d\theta_k \int dk G(\lambda k) e^{-2ka} \int_{tip} dV \int_{tip} dV' e^{-k(z'+z)} e^{-i\vec{k}\cdot(\vec{r}'-\vec{r})} M(r)M(r') \\ &\quad [\cos^2 \eta + \sin^2 \eta \cos(\theta_k - \phi') \cos(\theta_k - \phi) - i \cos \eta \sin \eta (\cos(\theta_k - \phi') - \cos(\theta_k - \phi))] \end{aligned} \quad (4.9)$$

The imaginary part in Eq. 4.9 is zero because the integral over ϕ and ϕ' cancel. Taking the narrow tip approximation $\alpha \ll 1$, we expand in the leading order of α to work out the integral of the real part. $e^{i\vec{k}\cdot(\vec{r}'-\vec{r})} \approx 1 + ik\alpha z(\cos(\theta_k - \phi) - \cos(\theta_k - \phi'))$ and here the imaginary part is again zero after integration. $\int_0^\pi d\phi \int_0^\pi d\phi' \cos(\theta_k - \phi) \cos(\theta_k - \phi) = 4 \sin^2 \theta_k$ and $\int d\theta_k (\cos^2 \eta + 4 \sin^2 \eta \sin^2 \theta_k) = 2\pi(1 + \sin^2 \eta)$. As a result, the in-plane component only changes the amplitude of A to the order of η^2 and the functional dependence remains the same.

To summarize, the errors associated with the two approximations we made in the truncated cone model are small.

4.5.3 Possible future improvement

The accuracy of λ in current MFM measurement is dominated by the uncertainty of tip geometry. This uncertainty can be greatly reduced once we replace the pyramid-shape tip by tips with simple geometry. The possible choices of tips for future improvement include a magnetically coated nanotube tip, which can be well described as a cylinder shell, and a spherical nanomagnet on top of a AFM tip, which is essentially a magnetic dipole. These tips are likely to carry a much smaller magnetic moment due to their small dimensions. To achieve good signal to noise with the nanotube or nanomagnet tips, one may have to reduce z and consider releasing the mirror approximation since the time-reversed mirror approximation may break down.

4.6 Time-reversed mirror approximation

The time-reversed mirror approximation is expressed mathematically as $G(\lambda k) \approx e^{-2\lambda k}$ (Eq. 4.2) in the limit of small λ/z . This approximation is good to the order of $O(\lambda/z)^3$. Under this approximation, any change in λ is equivalent to change in z and therefore $\Delta\lambda(T) \equiv \lambda(T) - \lambda(T_0)$ can be measured independent of any model of the sensor structure. We use it to determine $\Delta\lambda$ both by MFM and by scanning SQUID susceptometry.

4.6.1 $\Delta\lambda$ measurements by MFM and scanning SQUID susceptometry

To measure $\Delta\lambda(T)$ by MFM, we park the tip at a fixed z , changing T and record $\partial F_z/\partial z$. The change in $\partial F_z/\partial z$ can be counted by shifting z on a $\partial F_z/\partial z(z)$ curve at a base temperature T_0 . The amount we need to shift z gives the change of λ between T and T_0 . We extend $\Delta\lambda(T)$ to lower temperature than 5 K by scanning SQUID susceptometry (SSS) in a ^3He cryostat [73]. In SSS, we measure the mutual inductance between the field coil and the pick-up loop. In MFM, the tip acts as both the field source and the field sensor. In SQUID, the field-coil is the field source, while the pick-up loop is the sensor. The diamagnetic response for a superconductor is

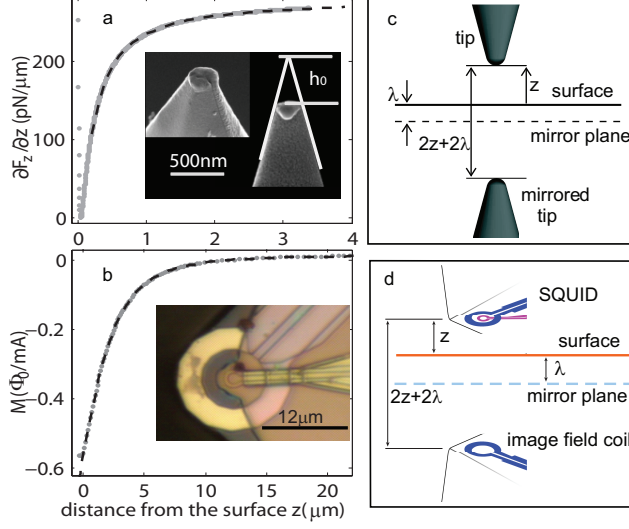


Figure 4.3: The time reversed mirror approximation for MFM and Scanning SQUID, using which we measure $\Delta\lambda$ independent of modeling. **a:** z dependence of $\partial F_z/\partial z$ (dots) by MFM at $T = 5$ K over a $\text{Ba}(\text{Fe}_{1-x}\text{Co}_x)_2\text{As}_2$ single crystal ($x=5.1\%$). The dashed line plots the fit to the truncated cone model, as described in the chapter. Inset shows scanning electron microscopy images of the tip, from which h_0 is fixed. **b:** z dependence of the mutual inductance M (dots) by SSS at $T = 0.4$ K a $\text{Ba}(\text{Fe}_{1-x}\text{Co}_x)_2\text{As}_2$ single crystal ($x=11\%$), and a fit (dashed line) to the mirror-image model [73]. Inset shows a photograph of the front end of the SQUID. **c,d:** Sketch showing the time-reversed mirror approximation for MFM(c) and SSS(d).

approximated as an imaged field coil $2(z+\lambda)$ from the pick-up loop. The measurement principle is illustrated in Fig 4.3.

4.6.2 Errors at large λ limit

The mirror approximation breaks down near the superconducting transition temperature T_c when λ/z is large. To estimate the error associated with it, I release the approximation of $G(k)$ and numerically calculate $\partial F_z/\partial z$ as a function of λ and z using the truncated cone approximation of the tip geometry. I first calculate the value of $\partial F_z/\partial z$ at $z = z_0$ and $\lambda = \lambda_0$. Then I calculate $\partial F_z/\partial z(z, \lambda)$ for various λ and obtain z_{app} which satisfies $\partial F_z/\partial z(z_{app}, \lambda_0) = \partial F_z/\partial z(z_0, \lambda)$. $z_{app} - z_0$ gives $\lambda_{meas} - \lambda_0$, e.g. $\lambda_{meas} \equiv \lambda_0 + (z_{app} - z_0)$. Fig. 4.4 shows the results of two sets of

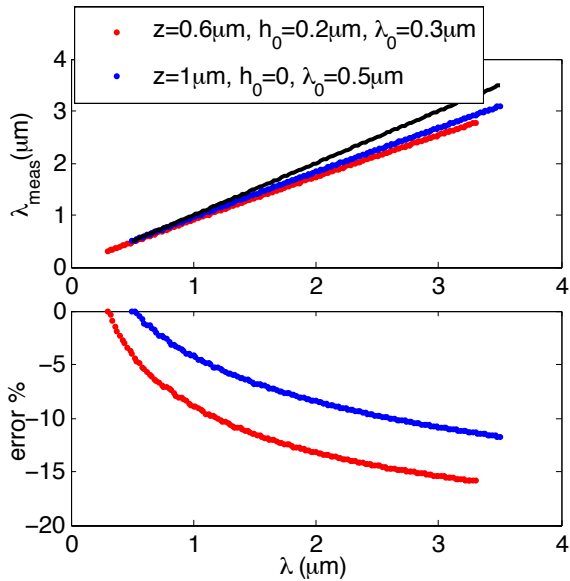


Figure 4.4: The estimated error in $\Delta\lambda$ from time-reversed mirror approximation. **a:** λ_{meas} using time-reversed mirror approximation as a function of the real λ . Red and blue dots plot two sets of parameters. The black line plots the real λ . **b:** The relative error defined as $(\lambda_{meas} - \lambda)/\lambda \times 100\%$ as a function of λ .

representative parameters. From the calculation we confirm that the error on λ_{meas} is smaller than 5% as long as $z > \lambda_0$. The error gets larger with increasing λ . At $\lambda = 3\mu\text{m}$, we underestimate λ by at most 15%.

4.6.3 Validity in fully anisotropic materials

Our model base on the Meissner response to an isotropic superconductor. However, most unconventional superconductors are anisotropic. One should be aware that the response field of an anisotropic superconductor may deviate from the isotropic case, and may be asymmetric even when the source has certain symmetries. V.G. Kogan calculate the response of an anisotropic superconductor to a local field source in detail (Ref. [81]). I will discuss his results in light of the validity of applying the time-reversed mirror approximation in our model.

Let $\lambda_{a,b,c}$ be the penetration depth of the three principal axes. When $\lambda_a = \lambda_b < \lambda_c$, the response of a uniaxial superconducting half-space with the c axis normal to the

interface to an arbitrary weak source is as if the superconductor were isotropic with the penetration depth $\lambda_{ab} \equiv \sqrt{\lambda_a \lambda_b}$. This result ensures that the calculation on isotropic superconductors can be directly applied to anisotropic materials as long as there is no in-plane anisotropy.

In the presence of in-plane anisotropy, the deviation from the isotropic case is small in the limit of small λ . Assume $\lambda_c > \lambda_b > \lambda_a$. When $z \gg \lambda$, we take $k\lambda \ll 1$, and obtain Eq. 18 in Ref. [81]:

$$\phi^r = \phi^s \left(1 - 2 \frac{\lambda_b k_x^2 + \lambda_a k_y^2}{k} \right)$$

let $\gamma^2 = \lambda_a/\lambda_b$ and $\epsilon = 1 - \gamma$, we can rewrite ϕ^r as

$$\phi^r = \phi^s \left(1 - 2k\lambda_{ab} - 2 \frac{(1 - \gamma)(k_x^2 + \gamma k_y^2)\lambda_{ab}}{\gamma k} \right)$$

The first two terms are the time-reversed mirror approximation. The third term is roughly $\epsilon k \lambda_{ab} \ll 1$ when $\epsilon \ll 1$ and $k \lambda_{ab} \ll 1$. The approximation is valid when $z \gg \lambda$ and the in-plane anisotropy is small.

In both the case discussed above, the response of λ_c drops off the result for any source.

4.6.4 λ_c mixing in in the presence of topography

When there are topographic steps in the vicinity of our local measurement, λ_c mixes in when the sensor is facing the crystal $a - b$ plane.

Assume the step height is h . The dominant effect of c -axis conduction is to shift the depth of currents flowing along $a - b$ plane. To a rough estimation, the screening current depth in ab plane can be approximated as:

$$y(x) \approx \lambda_{ab} + h e^{-x/\lambda_c}$$

where $x = 0$ is at the step.

The temperature-induced change is then:

$$dy/dT \approx d\lambda_{ab} + hx/\lambda_c^2 e^{-x/\lambda_c} d\lambda_c/dT$$

Our measurements average over a length scale of L . Assume $L \gg \lambda_c$, we obtain the measured value as:

$$\Delta\lambda_{meas}(T) = \Delta\lambda_{ab}(T) + h/L\Delta\lambda_c(T)$$

A reasonable upper limit of the size of steps in regions we take MFM scans is 10 nm. If we average over 2 μm , we obtain an upper limit of 1% λ_c mixing in λ_{ab} measurements. For SQUID, a reasonable upper limit of the size of steps in regions we scan is 500 nm and λ_{ab} measurements average over 15 μm , which gives 4% λ_c mixing in λ_{ab} measurements.

Since $\lambda_c \gg \lambda_{ab}$ and to first order multiple steps will be additive, $\Delta\lambda_c$ mixing in $\Delta\lambda_{ab}$ can be significant if the sample surface is rough. It is therefore important to choose flat regions for the measurements.

4.7 Estimate λ by imaging individual vortices

The sharp cone model and the truncated cone model can also be applied to describe the vortex profile in MFM images. The magnetic field of a vortex at the interface between half-space superconductor and vacuum is given by [82]:

$$\vec{B}(R, z) = \frac{\Phi_0}{(2\pi)^2} \int d^2q \frac{\exp(i\vec{q} \cdot \vec{R} - qz)}{Q(Q + q\lambda_{ab})} (\hat{z} - i\hat{q})$$

where $Q = \sqrt{1 + (\lambda q)^2}$. The signal of a vortex is:

$$\frac{\partial F_z}{\partial z}(R, z) = \int dz' d^2R' M_z(\vec{R}', z') \frac{\partial^2}{\partial z'^2} B_z(\vec{R} + \vec{R}', z + z').$$

In order to get analytical expression of the vortex profile, we neglect the width of the MFM tip and assume its magnetic moment is along the \hat{z} axis. In the sharp cone

model, the tip's magnetic moment is given as $\vec{M}(z) = mt\delta(R - \alpha z)\hat{z}$. The signal of a vortex is then approximately

$$\frac{\partial F_z}{\partial z}(R, z) = m\Phi_0 t \int dz' \alpha z' \frac{\exp(-q(z+z'))}{Q(Q+\lambda q)} q^3 J_0(qR). \quad (4.10)$$

where J_n is the Bessel function and $\int d^2k \exp ik \cdot r = \int k dk 2\pi J_0(kr)$.

At large z limit, $z \gg \lambda$, $\lambda q \ll 1$ and $Q(Q + \lambda q) = \exp(\lambda q) + O(\lambda q)^2$.

The vortex profile from Eq. 4.10 can be approximated as:

$$\frac{\partial F_z}{\partial z}(R, z) = m\Phi_0 t \alpha \frac{(z + \lambda)}{((z + \lambda)^2 + R^2)^{3/2}}. \quad (4.11)$$

The peak magnitude is at $R = 0$ and has a z dependence of:

$$\frac{\partial F_z}{\partial z}(z)_{\max} = \frac{\partial F_z}{\partial z}(R = 0, z) = m\Phi_0 t \alpha \frac{1}{(z + \lambda)^2}. \quad (4.12)$$

If we model the tip as truncated cone, the vortex profile in the limit of large z is

$$\frac{\partial F_z}{\partial z}(R, z) = m\Phi_0 t \alpha \left(\frac{(z + \lambda)}{((z + \lambda)^2 + R^2)^{3/2}} + \frac{h_0(2(z + \lambda)^2 - R^2)}{((z + \lambda)^2 + R^2)^{5/2}} \right). \quad (4.13)$$

and the peak magnitude is

$$\frac{\partial F_z}{\partial z}(z)_{\max} = m\Phi_0 t \alpha \left(\frac{1}{(z + \lambda)^2} + \frac{2h_0}{(z + \lambda)^3} \right). \quad (4.14)$$

The approximation of neglecting the tip width leads to large errors in determining λ from images of vortices. Comparing to the errors, the correction from truncating the sharp cone as taken in the TCM is not significant so we use the cone model (Eq.4.11, 4.12) to describe vortices for simplicity. There are two ways to get an estimate of λ from vortex image: via the peak magnitude and via the spatial extension. We take images of isolated vortices at consecutive constant heights. We fit the images to Eq. 4.10, using the peak magnitude $A_v \equiv m\Phi_0 t \alpha / (z + \lambda)^2$ and the width $w \equiv z + \lambda$ as free parameters. From the images and fits, we get A and w as a function of z . The

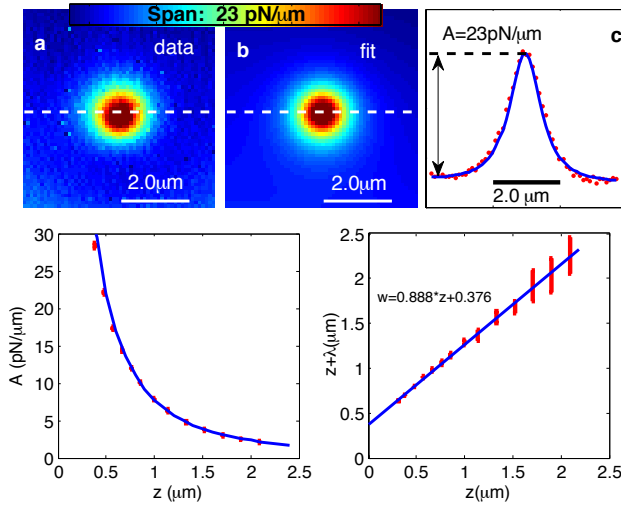


Figure 4.5: Extracting an estimate of λ from images of individual vortices in a $\text{YBa}_2\text{Cu}_3\text{O}_{6+x}$ ($x = 0.56$) single crystal. **a,b**: image of a vortex at $T = 5$ K and $z = 0.4 \mu\text{m}$ (a) and fit to Eq. 4.11 (b). The dashed line shows the positions plotted in (c). **c**: line cut of the image and the fit in (a) and (b). Also shown the extraction of the peak magnitude $A_v \equiv \max(\partial F/\partial z)$. **d**: A_v from a set of vortex images (including (a)) at consecutive heights (red dots). The solid line plots the fit to of z dependence to the cone model (Eq. 4.12), which gives gives $\lambda = 230 \pm 30$ nm as a fit parameter. **e**: $z + \lambda$ extracted from fitting to Eq. 4.12 as a function of z . The solid line plots a linear fit of $z + \lambda = Cz + z_0$. We get $C = 0.89$ and $z_0 = 360$ nm.

z dependence of A is then fit to Eq. 4.12, with λ as a free parameter. Meanwhile, the z dependence of w is expected to be linear with a slope close to 1. The intersection of w at $z = 0$ gives another estimate of λ .

Fig. 4.5 show the result from sample II as used in section 4.4. The fit to A_v in Fig. 4.5(d) gives $\lambda = 230 \pm 30$ nm. This is not far from the expected value $\lambda = 180$ nm. The linear fit to w in Fig. 4.5(e) gives $\lambda \approx 370$ nm. This number overestimate λ significantly. However, Also, to a crude approximation, one can correct the effect of convolution by subtracting a representative tip width. When we use tip width of 100 nm, we get an estimate of λ to be 270 nm. This is much closer than an estimate using the half width at half maximum (HWHM) of vortex images as demonstrated in [74], which is off by a factor of 2.5.

Chapter 5

Local measurement of the penetration depth in the pnictide superconductor

$\text{Ba}(\text{Fe}_{0.95}\text{Co}_{0.05})_2\text{As}_2$

Abstract: The discovery of iron based superconductors has generated great interest in understanding their pairing symmetry and pairing mechanism, which can be studied by the superfluid density. Some properties of the iron-pnictides, such as multiple conduction bands and vicinity of the superconductivity to magnetic order, give additional challenges to accurately determine the superfluid density $\rho_s(T) \equiv 1/\lambda(T)^2$. We demonstrated on single crystals of $\text{Ba}(\text{Fe}_{0.95}\text{Co}_{0.05})_2\text{As}_2$ that MFM can measure the important and hard-to-determine absolute value of λ , as well as obtain its temperature dependence and spatial homogeneity. We observe that the temperature variation $\Delta\lambda(T)$ varies 20 times slower with temperature than previously reported by bulk techniques. $\rho_s(T)$ over the full temperature range is well described by a clean two-band fully gapped model, consistent with the proposed $s\pm$ pairing symmetry. The work discussed in this chapter appears in Phys. Rev. B. **81**, 100501(R) (2010).

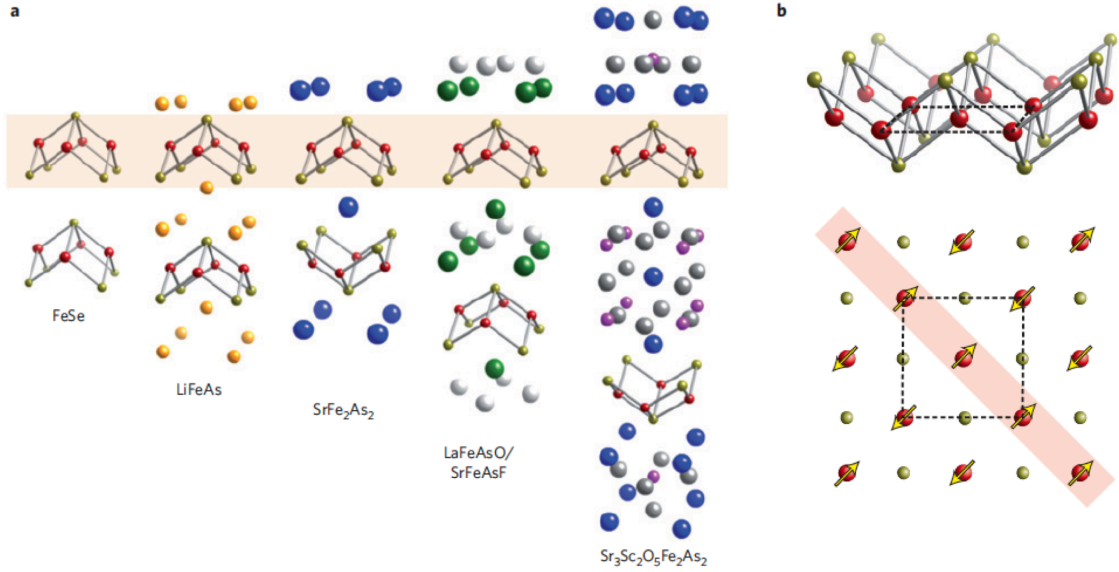


Figure 5.1: Crystallographic and magnetic structures of the iron-base superconductors. Image taken from ref [84]. **a:** The five structures of the iron-based superconductor. Among them the 1111 families (fourth from the left) have the highest T_c , while the 122 families (third from the left) are the mostly studies systems. **b:** The active planar iron layer common to all families. Iron ions shown in red and Pn (short for pnictogen/chalcogen) shown in red. The dashed line indicates the unit cell, which includes two Fe atoms due to the staggered Pn positions. The ordered spin arrangement is indicated by arrows.

5.1 Brief introduction of iron-pnictide superconductors

The surprising discovery of 26 K superconductivity in doped LaFeAsO [83] has generated great interests in understanding properties of iron-based superconductors (FePn). It is commonly believed that the superconductivity originates from a planar layer of iron and pnictogen (P, As) or chalcogen (S, Se, Te). Depending on the crystalline structure, they can be divided into five families, as shown in Fig. 5.1. Among all of the compounds, the 1111 families have the highest T_c ; the 122 families are the mostly studied systems owing to the better access of high-quality single crystals, and widely thought to capture the main features of all iron-pnictide superconductors.

The pairing symmetry of the pnictides depends on the electronic band structure and the pairing mechanism. Band structure calculation using the local density approximation [85] gives a Fermi surface consisting of at least two hole pockets at the Brillouin zone (BZ) center (Γ point) and two electron pockets at $(0, \pm\pi)$ and $(\pm\pi, 0)$. The two non-equivalent pnictigen positions result in folding the BZ zone to include two Fe atoms per unit cell and to put the electron pockets at $(\pm\pi, \pm\pi)$. Depending on the structural details, there might be a third hole pockets at Γ point. The multiple-band Fermi surface has been confirmed experimentally, by several angle-resolved photoemission spectroscopy (ARPES) [86–88], and quantum oscillation measurements [89].

Fig. 5.2a plots the typical phase diagram of the Ba-based 122 system. In BaFe_2As_2 , the systematic substitution of either the Ba [90], Fe [91, 92], or As [93] sites with a different element produces very similar phase diagram: the superconducting phase has a dome shape with substitution. The undoped and lightly doped compounds have coupled anti-ferromagnetic (AFM) and structural transitions at elevated temperatures, which is suppressed as the superconducting (SC) phase onsets and disappears when SC has more or less the highest transition temperature T_c . This behavior is different from the fluorine-doped 1111 systems (Fig. 5.2b), where AFM and SC phases are completely separated and do not overlap; the magnetic and structural transitions happen at separated temperatures even for the undoped compound [94].

As for any unconventional superconductors, the mechanism that causes superconductivity in the iron-pnictides is a question of primary importance. The electronic structure suggests that the same magnetic interactions that drives AFM ordering also produce the pairing interaction for superconductivity [95]. If the interaction is repulsive, as mediated by magnetic fluctuations, the order parameter of the superconducting state need to change sign along the direction where the magnetic coupling is the strongest. Therefore, the proposed order parameter (OP) for the pnictide has a sign change between Γ (0,0) and M ($\pm\pi, \pm\pi$) points. The possible OP symmetry are plotted in Fig. 5.3. Among them the most discussed one is the s_{\pm} , where the OP changes sign between Γ and M but has the same sign at both Γ and M .

Experimental determinations of the OP symmetry usually probe either the phase or the amplitude of the OP. Very limited phase experiments have been done so far,

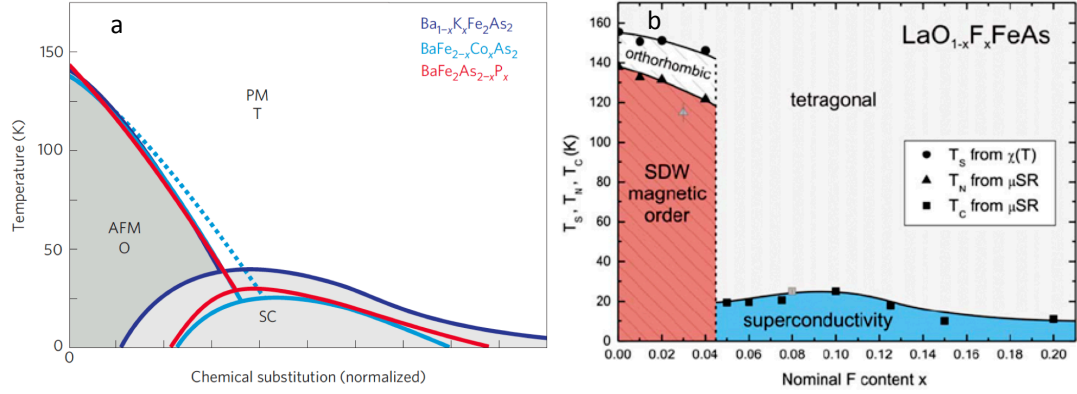


Figure 5.2: Experimental phase diagrams of the BaFe_2As_2 system (a, data from ref [90, 91, 93], image taken from ref [84]) and fluorine-doped 1111 system (b, ref [94]). Both systems go through the structural transition from tetragonal to orthorhombic phase and magnetic transition from paramagnetic to anti-ferromagnetic phase (spin-density wave). The magnetic structure in the AFM phase is shown in Fig. 5.1.

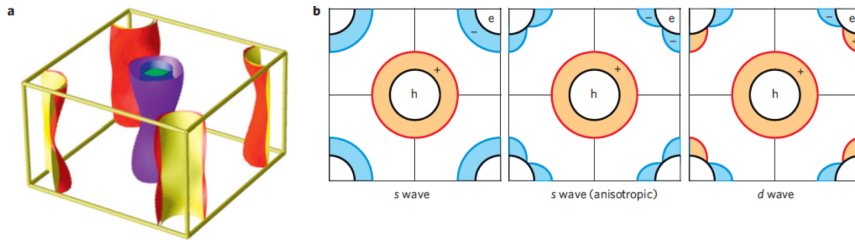


Figure 5.3: The Fermi surface structure (a) and superconducting OP symmetry of 122 iron-pnictides (b). Images taken from ref [84]. **a**: FS of BaFe_2As_2 with 10% Co doping, calculated using DFT and drawn on the true BZ zone (ref [96]). The hole pockets are centered at Γ point and the electron pockets at M point. **b**: Schematic of the OP structure on the two-dimensional projection of FS. The proposed multi-band pairing gap symmetries, drawn on as shaded regions on the hole (orange) and electron (blue) pockets, are shown for an s_{\pm} structure with isotropic gaps (left) and anisotropic gaps with accidental nodes on the electron pocket (middle), and for a d -wave symmetry (right).

owning the difficulty to design tunnelling junction experiments that can distinguish a conventional s -wave state from $s\pm$ states. The experiments reported so far [97, 98] is inconsistent with d -wave symmetry but compatible with $s\pm$ symmetry.

The magnitude of the OP, e.g. the superconducting gap structure, is usually probed through the excitation rate of quasi-particles. It can be measured by obtaining the temperature dependence of a few properties, including the nuclear relaxation rate (by NMR), thermal conductivity, specific heat and the magnetic penetration depth. Comparing with other quasi-particle excitation measurement, measurements of the magnetic penetration depth λ have the advantage of directly probing the superconducting states: λ is determined by the superfluid density, $\rho_s(T) \equiv 1/\lambda^2$, which is related to the number of electrons in the superconducting states.

The temperature dependence of $\rho_s(T)$ is a sensitive probe of the superconducting gap structure. When the gap is zero at nodes on the Fermi surface, $\rho_s(T)$ varies as a power law in T at low T [67, 99]. A fully gapped OP gives a low- T exponential dependence: $\rho_s(T)/\rho_s(0) \approx 1 - \sqrt{2\pi\Delta_0/T} \exp(-\Delta_0/T)$, where Δ_0 is the superconducting gap at $T = 0$. Since it is difficult to determine $\lambda(T)$, its temperature-induced change, $\Delta\lambda(T) \equiv \lambda(T) - \lambda(0)$ is often measured, which follows the same temperature dependence as ρ_s at low T . Table 5.1 provides an incomplete list of $\Delta\lambda$ and λ measurements in single crystals of iron-pnictides, which shows a wide disparity. For example, linear $\Delta\lambda(T)$ in clean LaFePO over a wide temperature range provides strong evidence for well formed line nodes [73, 100]. Similar behaviors were reported in $\text{BaFe}_2(\text{As,P})_2$ [101] and KFe_2As_2 [102] compounds but ruled out for most other samples that were studied. Moreover, different groups measuring nominally the same samples do not agree (e.g. $(\text{Ba,K})\text{Fe}_2\text{As}_2$).

A few hypotheses can explain the disparity of the penetration depth. Band structure calculations have shown that the s and d states are nearly degenerate [109]. Therefore, a small change in the crystallographic or electronic structure, e.g. the pnictogen height [110], could switch one to the other. It can also be induced by impurity scattering. Pair breaking process can lift the node [111]; it can also change the exponential behavior of isotropic $s\pm$ to a steep power-law [112]. Moreover, sample inhomogeneity can affect all the measurements, and the unknown absolute value of

Table 5.1: The literature on penetration depth measurement taken on single-crystal pnictide superconductors before Sep. 2009. The results are organized by the crystalline structure of the materials. The measurement techniques are also provided along with the group and reference information. ‘×’ stands for ruled out by the authors. When it is marked at columns labelled as ‘full gap’, it refers to behaviors inconsistent with exponential $\Delta\lambda(T)$ or $\rho_s(T)$. ‘✓’ refers to the preferred explanation by the authors and ‘-’ stands for no comments.

sample	1 full gap	$\frac{\rho_s(T)}{\rho_s(0)}$		$\Delta\lambda$		method	group	Ref
		2 full gap	T nodal	T^2				
SmFeAs(O,F)	×	✓	×	-	RF oscillator	Bristol	[103]	
1111 PrFeAsO _{1-y}	×	✓	×	-	microwave	Kyoto	[104]	
RFeAs(O,F)	×	×	×	✓	RF oscillator	Ames	[105]	
P-base LaFePO	×	×	✓	×	RF oscillator	Bristol	[100]	
LaFePO	×	×	✓	×	SQUID	Stanford	[97]	
BaFe ₂ (As,P) ₂	×	×	✓	×	microwave	Kyoto	[101]	
122 (Ba,K)Fe ₂ As ₂	×	✓	×	-	microwave	Kyoto	[106]	
(Ba,K)Fe ₂ As ₂	×	×	×	✓	RF oscillator	Ames	[107]	
Ba(Fe,Co) ₂ As ₂	×	×	×	✓	RF oscillator	Ames	[108]	

λ greatly limit the ability to accurately determine the gap structure, especially given the multiband nature of the pnictides. It is therefore important to be able to measure both λ and $\Delta\lambda$ locally on a scale of a few microns.

5.2 Measurement of $\rho_s(T)$ in $\text{Ba}(\text{Fe}_{0.95}\text{Co}_{0.05})_2\text{As}_2$

We measure the local $\Delta\lambda_{ab}(T)$ and $\lambda_{ab}(T)$, the penetration depth for screening currents flowing in the a-b planes, in electron-doped $\text{Ba}(\text{Fe}_{1-x}\text{Co}_x)_2\text{As}_2$ single crystals ($x \approx 0.05$, $T_c = 18.5$ K, grown from self-flux [92]) from $T = 5$ K to T_c by magnetic force microscopy (MFM) [Fig. 5.4]. We also use scanning SQUID susceptometry (SSS) [113] to measure $\Delta\lambda_{ab}(T)$ down to 0.4 K. We find that ρ_s can be well described by a two-band fully gapped OP over the full temperature range. We also use MFM to image and manipulate vortices to measure the homogeneity of $\lambda_{ab}(T)$ and the flux pinning force. We find that ρ_s is uniform to within 10% or better, although vortex

pinning is highly inhomogeneous.

In our MFM, a sharp magnetic tip at the end of a flexible cantilever faces the crystal surface, which is parallel to the a-b plane. By measuring the shift in the cantilever's resonant frequency [2], we determine $\partial F_z/\partial z$ [37], where F is the force between the tip and the sample, and \hat{z} is along the tip magnetization direction and is normal to the cantilever and to the crystal a-b surface. $\partial F_z/\partial z$ changes abruptly within a few nanometers of the surface, allowing precise determination of the tip-sample separation z . In the Meissner state, the tip-superconductor interaction can be approximated by the magnetic interaction between the tip and its image mirrored through a plane at $z = -\lambda_{ab}$ (Fig. 5.4a inset) [78]. This local levitation force is determined uniquely by $z + \lambda_{ab}(T)$ for $z \gg \lambda_{ab}$ (λ_c does not enter for any source field above a smooth, infinite ab surface) [81]. Thus, changing T at constant z offsets a $\partial F_z/\partial z$ curve along the \hat{z} -axis by $\Delta\lambda_{ab}(T)$. To acquire the data labeled as MFM $\Delta\lambda$ in Fig. 5.5, we park the tip at $z = 500$ nm, change T and acquire $\partial F_z/\partial z$. The z offset required to match $\partial F_z(T)/\partial z$ with a reference curve at $T = 5$ K gives $\lambda_{ab}(T) - \lambda_{ab}(5\text{K})$. Using a similar method for data acquired by SSS in a ^3He refrigerator [73], we extend measurements of $\Delta\lambda_{ab}$ down to 0.4 K on two nominally identical samples. The SSS results match the MFM results over the common temperature range. By using local scanning probes, we reduce the influence of the complex topography around the sample edges [81].

Figure 5.5 shows that $\Delta\lambda_{ab}(T)$ increases very slowly with T at low T , inconsistent with the linear dependence that would be expected for line-nodes. The same behavior appears at three different locations on two samples with SSS and at four different locations with MFM on a third sample. Between $T = 0.02T_c$ and $0.4T_c$ $\Delta\lambda_{ab}(T)$ varies by about an order of magnitude less than has been reported for a similar sample using a bulk technique [108]. At low T , $\Delta\lambda_{ab}(T)$ can be described by either a two-band fully-gapped model or by a power law with a small coefficient as described below.

We also extract $\lambda_{ab}(T)$ by modeling the tip-superconductor interaction, with the magnetic tip as a sharp, single domain cone, truncated at a distance $h_0 = 400 \pm 20$ nm from its apex as shown in Fig. 5.4e. Within the model, the z -dependence of $\partial F_z/\partial z$

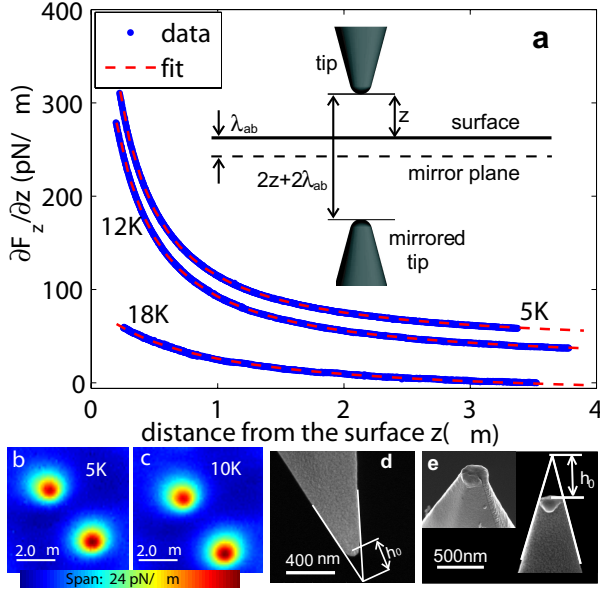


Figure 5.4: Technique to measure λ and $\Delta\lambda$ by MFM from Meissner repulsion (a) and vortex imaging (b,c). **(a)** z dependence of $\partial F_z/\partial z$ (blue symbols) at $T = 5, 12$ and 18 K and the fit to the truncated cone model (red dashed line). **(Inset)**: Sketch to illustrate that the tip-superconductor interaction in the Meissner state can be approximated by the interaction between the tip and its image mirrored through a plane (dashed line) λ_{ab} below the surface of the superconductor (solid line) when $z \gg \lambda_{ab}$. Comparing the curves provides $\Delta\lambda_{ab}$ independently of the tip model. Fits give $\lambda_{ab}(T)$ at $T = 5, 12, 18$ K to be $0.33, 0.37, 1.10 \mu\text{m}$. **(b, c)** Images of two vortices ($z = 400$ nm) at 5 K (b) and 10 K (c). The shapes and amplitudes depend on both the magnetic field from vortices and the tip structure, but the similarity shows that both the spatial variation and the temperature-induced change of λ_{ab} are small. **(d,e)** Scanning electron microscopy images of the tip before (d) and after (e) the measurements. Also shown are the truncation distance $h_0 = 300 \pm 30$ nm in (d) and $h_0 = 400 \pm 20$ nm in (e). An accidental crash during the measurement changes the truncation distance h_0 from 300 ± 30 nm (d) to 400 ± 20 nm (e). Despite the crash, $\partial F_z/\partial z$ curves taken before and after the crash give the same $\lambda_{ab}(5\text{K})$ to within 10 nm.

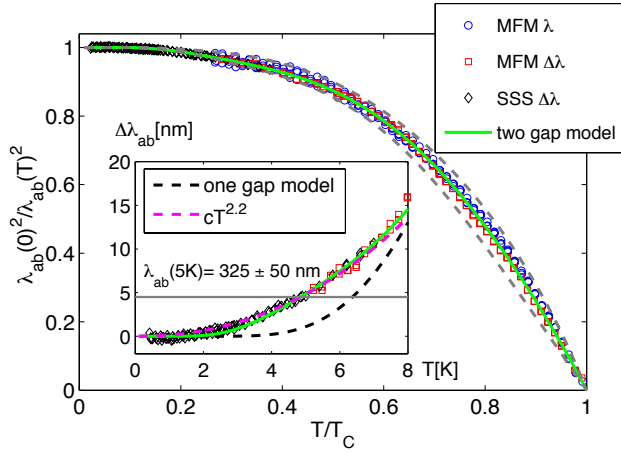


Figure 5.5: Normalized superfluid density $\rho_s(T)/\rho_s(0) \equiv \lambda_{ab}(0)^2/\lambda_{ab}(T)^2$ vs. T . We determine $\Delta\lambda_{ab}(T)$ by MFM (squares) and by SSS (diamonds) from measuring the change in the diamagnetic response at fixed height. These values are offset to match the absolute value of $\lambda_{ab}(T)$ obtained by fitting the MFM data to the truncated cone model (circles). The green solid line shows a fit of the two-band s-wave model discussed in the main text ($\Delta_1 = 2.6T_c$, $\Delta_2 = 0.8T_c$, $x = 0.88$ and $a = 1.4$). The width of the dashed band reflects the uncertainty in $\lambda_{ab}(0)$. **Inset:** $\Delta\lambda_{ab}$ vs. T at low T . Black dashed line: one-gap s-wave model with $a = 1.5$ and $\Delta_0 = 1.95T_c$. Magenta dashed line: $\Delta\lambda_{ab}(T) = cT^{2.2}$ ($c = 0.14\text{nm}/\text{K}^{2.2}$).

is given by:

$$\frac{\partial F_z(z, T)}{\partial z} - \frac{\partial F_z(z, T)}{\partial z} \Big|_{z=\infty} = A \left(\frac{1}{z + \lambda_{ab}(T)} + \frac{h_0}{(z + \lambda_{ab}(T))^2} + \frac{h_0^2}{2(z + \lambda_{ab}(T))^3} \right) \quad (5.1)$$

where A is determined by the tip shape and the coating. The value $A = 78$ pN from fitting at $T < T_c/2$ is consistent to within 30% with the magnetic moment expected from the nominal iron coating on the tip, and with that inferred from the tip-vortex interaction [37]. We record $\partial F_z/\partial z$ as a function of z and T and extract λ_{ab} at many temperatures by fitting to Eq. 5.1 with A and h_0 fixed and λ_{ab} and $\partial F_z/\partial z(\infty, T)$ allowed to vary separately for each T . The fit works well for all T (Fig. 5.4). The resulting values of $\lambda_{ab}(T)$ are shown in Figure 5.5 with label ‘‘MFM λ ’’ and agrees well with the model-independent $\Delta\lambda_{ab}$. If we consider only statistical errors, we obtain $\lambda_{ab}(5K) = 325 \pm 5$ nm with 70% confidence interval. However, the systematic error from the finite width corrections of the tip-geometry is 5%. In addition, the ± 20 nm uncertainty on h_0 leads to $74 \text{ pN} \leq A \leq 81 \text{ pN}$ by bootstrapping. The extremals of A and h_0 gives ± 35 nm systematic error on $\lambda_{ab}(5K)$. Thus, adding the two main sources of systematic error, we find $\lambda_{ab}(5K) = 325 \pm 50$ nm.

Knowing $\lambda_{ab}(T)$ gives ρ_s over the full temperature range (Fig. 5.5). The fact that ρ_s does not saturate at low T is inconsistent with a single-band isotropic gap. A two-band fully gapped OP, which was proposed theoretically [95, 114] and tested experimentally [86, 106], describes the data well (Fig. 5.5). In the model,

$$\rho_s(T) = x\rho_1(T) + (1 - x)\rho_2(T), \quad (5.2)$$

where $\rho_{1,2}(T)$ are the superfluid densities in bands $i = 1, 2$, with gaps

$$\Delta_i(T) = \Delta_i(0) \tanh \left(\frac{\pi T_C}{\Delta_i(0)} \sqrt{a_i \left(\frac{T_C}{T} - 1 \right)} \right), \quad (5.3)$$

where a_i describes the rate of $\Delta_i(T)$ increasing upon cooling from T_c [68]. Our fit (taking into account the systematic error on $\lambda_{ab}(5K)$) gives $\Delta_1(0) = 2.5 \pm 0.3T_c$,

$\Delta_2(0) = 0.70 \pm 0.1T_c$, $x = 0.89 \pm 0.06$ and $a_1 = 1.45 \pm 0.4$ with $a_2 \equiv 1$. The value of a_1 suggests that pairing is likely to be more complicated than phonon-mediated weak coupling [115, 116], which would give $a = 1$. The magnitude of $\Delta_{1,2}(0)$ is consistent with the scaled down values deduced from optical spectroscopy on similar materials with higher T_c [86, 117]. At low T a power law cT^n where $n = 2.2$ and $c = 0.14 \text{ nm/K}^{2.2}$ also fits the data. The dominant sources of errors are the calibration accuracy of the scanner, thermal drift, and the breakdown of the assumption of $z \gg \lambda_{ab}$, which together would bound c between 0.12 and 0.18 $\text{nm/K}^{2.2}$. The small coefficient is inconsistent with that previously reported [107]. We are not aware of any model for nodal OP, either clean or reasonably dirty, that predicts such a small $\Delta\lambda_{ab}$ below $0.4T_c$. Instead, we interpret this weakened exponential behaviour of $\Delta\lambda_{ab}$ and $\rho_s(T)$ from 0.4 K all the way to T_c as strong evidence for two full gaps, consistent with the extended s-wave OP [95, 118].

5.3 Vortex images as quantitative measure of $\rho_s(T)$ inhomogeneity

We performed three tests of ρ_s uniformity.

First, we repeated the touchdown measurements at four positions separated by around 10 μm and obtained $\lambda_{ab}(T = 5 \text{ K}) = 325 \text{ nm}, 330 \text{ nm}, 325 \text{ nm}$ and 330 nm . This result suggests that λ_{ab} is uniform across the sample.

A second test of uniformity is afforded by measuring the local T_c by mapping the lowest T at which we cannot detect Meissner levitation by MFM (sensitivity corresponds to $\lambda_{ab}(T) > 3 \mu\text{m}$) or diamagnetic response by SSS (sensitivity corresponds to $\lambda_{ab}(T) > 20 \mu\text{m}$ [119]). We find the variation of T_c to be less than 0.5 K throughout the range of $10 \times 10 \mu\text{m}^2$ by MFM and $200 \times 200 \mu\text{m}^2$ by SSS.

Vortex imaging provides a third test of $\rho_s(T)$ uniformity. To this end, we cool the sample in an external magnetic field and scan the tip at a constant height z above the surface at 5 K. All vortices appear very similar (Fig. 5.6a), indicating that the spatial variation of λ_{ab} is limited. The convolution of the tip and the vortex field makes

it difficult to extract λ_{ab} from vortex imaging, as explained in Chapter 4. Instead, we calculate the normalized curvature \mathcal{C} at each vortex peak to quantify the spatial variation by taking similar approximations as in session 4.4 and using equations 4.13 and 4.14:

$$\begin{aligned} \mathcal{C} &\equiv \max \left((\partial F_z / \partial z)^{-2} \det \left(\frac{\partial^2 (\partial F_z / \partial z)}{\partial x_i \partial x_j} \right) \right) \\ &= \frac{9}{(z + \lambda_{ab})^4} \left(\frac{z + \lambda_{ab} + 4h_0}{z + \lambda_{ab} + 2h_0} \right)^2 \end{aligned} \quad (5.4)$$

(i, j run over 1, 2 and $x_1 \equiv x, x_2 \equiv y$). The length-scale $\mathcal{C}^{-1/4}$ characterizes the spatial extent of the magnetic field from each vortex (Fig. 5.6a). The scatter (Fig. 5.6b) of the normalized $\mathcal{C}^{-1/4}$ ($\pm 8\%$) at constant z gives an estimate for the spatial variation of λ_{ab} .

In contrast to the uniform ρ_s , vortex pinning is very inhomogeneous. Vortices do not form an ordered lattice when field-cooled in fields up to 13 mT, the highest field that allows us to resolve individual vortices in this material. Instead, vortices always appear in the same regions when we thermal cycle in different fields using different cooling rates (Fig. 5.7a). This behavior suggests inhomogeneous pinning. To measure the pinning force distribution, we use the MFM tip to drag individual vortices and to convert the recorded $\partial F_z / \partial z$ to the required force [37]. We measure two different forces (Fig. 5.7 b-d): the force for dragging the most weakly pinned vortex, F_{\min} , a measure of the smallest pinning force; and the force for dragging all of the vortices (usually ≤ 10) in a field of view, F_{typ} , a measure of the typical pinning force. In this sample $3 \leq F_{\text{typ}} / F_{\min} \leq 5$. $F_{\text{typ}} \approx 18$ pN at 5K, corresponding to a critical current of $J_c \approx 80$ kA/cm² ($F_c = J_c \Phi_0 d$, where Φ_0 is the flux quantum, $d = 10 \mu\text{m}$ is the sample thickness), consistent with the value from bulk measurement of an optimally doped sample [120]. Even at F_{typ} , vortices do not follow the tip all the way, indicating the existence of pinning forces larger than F_{typ} . In fact, F_{typ} is still at least an order of magnitude smaller than the force required to stabilize vortices in the dense clusters we see (the vortex-vortex interaction for a pair separated by 400 nm corresponds to a current density of 3 MA/cm²). We do not detect any correlation

between pinning and superfluid density, suggesting that strong pinning exists without affecting superconductivity on the scale of λ_{ab} . The ability to measure the absolute value of the penetration depth despite a disordered vortex configuration is important, since the most commonly used method, muon-spin-rotation [121], assumes an ordered vortex configuration.

5.4 Conclusion

To conclude, by measuring $\lambda_{ab}(T)$ and $\Delta\lambda_{ab}(T)$ locally we find that underdoped $\text{Ba}(\text{Fe}_{1-x}\text{Co}_x)_2\text{As}_2$ ($x \approx 0.05$) has homogenous ρ_s whose temperature dependence can be described by a two-band fully-gapped OP. This result provides thermodynamic evidence for fully gapped models such as the proposed extended s-wave model [95, 114] for electron doped 122 pnictides at the underdoped regime. We obtain $\lambda_{ab}(0) = 325 \pm 50$ nm, which gives a phase-coherent temperature of above 100 K, much higher than T_c , hinting that phase fluctuations are not as important here as in the underdoped cuprates [69]. Instead, T_c in the underdoped iron-pnictides may be suppressed by the competition with non-superconducting phases. MFM allows us to obtain the superfluid density and to map its spatial variation down to the submicron scale. This capability may be useful to study how different phases compete for charge carriers.

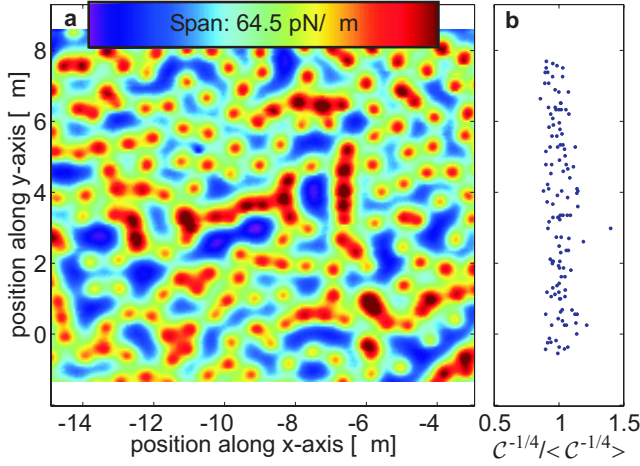


Figure 5.6: Spatial uniformity of λ_{ab} from vortex imaging at 5 K. **(a)** Image of vortices at $T = 5\text{K}$, $z = 125\text{ nm}$ and $B = 3.5\text{ mT}$. **(b)** The normalized length-scale associated with each vortex peak in (a): $\mathcal{C}^{-1/4} / \langle \mathcal{C}^{-1/4} \rangle$ ($\langle \rangle$ denotes the mean). We find $\mathcal{C}^{-1/4} = 250(1 \pm 0.08)\text{ nm}$ (70% confidence interval).

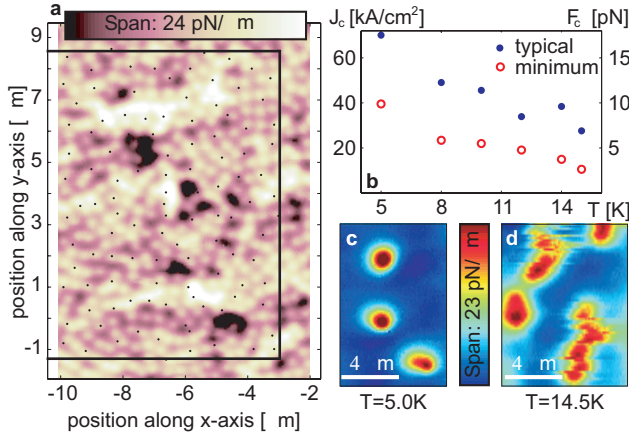


Figure 5.7: Inhomogeneous vortex pinning. **(a)** Image of vortices at $T = 5\text{ K}$, $z = 80\text{ nm}$ and $B = 9.5\text{ mT}$, overlaid by the vortex positions (dots) in Fig. 5.6a and the boundary of that scan (black frame). The vortex configuration is highly disordered. Vortices avoid the same regions in both scans, taken days apart and many thermal cycles between. **(b)** Local critical current (left ordinate) and the depinning force (right ordinate) vs. T . The comparison of minimum and typical values implies inhomogeneous pinning. **(c)** Image of vortices at $T = 5\text{ K}$, $z = 120\text{ nm}$ showing that F_{\min} only moves the vortex at the bottom. **(d)** Image of moving vortices at $T = 14.5\text{K}$, $z = 430\text{nm}$ showing that F_{typ} allows us to drag all vortices a distance of several microns.

Chapter 6

Local measurement of the superfluid density in the pnictide superconductor $\text{Ba}(\text{Fe}_{1-x}\text{Co}_x)_2\text{As}_2$ across the superconducting dome

Abstract We locally measure the superfluid density $\rho_s(T)$ in $\text{Ba}(\text{Fe}_{1-x}\text{Co}_x)_2\text{As}_2$ single crystals with magnetic force microscopy and scanning SQUID susceptometry. These high-precision, local-probe-based techniques enable us to measure both the zero temperature value of the superfluid density $\rho_s(0)$ and the temperature variation, to distinguish homogeneous from spatially varying responses, and to report systematic behavior as a function of Co doping across the superconducting dome. We observe systematic evolution of $\rho_s(T)$ that can be summarized as three trends. First, $\rho_s(0)$ falls more quickly with T_c on the underdoped side of the dome than on the overdoped. Second, the temperature variation of $\rho_s(T)$ at low temperature increases away from optimal doping. Third, $\rho_s(T)$ increases sharply with cooling through the superconducting transition temperature T_c of both optimally doped and underdoped compounds. These observations are consistent with magnetic fluctuation mediated pairing and the coexistence of magnetism and superconductivity. The work described in the chapter appears in *Phys. Rev. Lett.* **106**, 067001 (2011).

6.1 Introduction

The magnetic penetration depth λ is one of the most important length scales in superconductors [66]. Its temperature evolution is a sensitive probe of the superconducting gap structure [67, 68] and its value is related to the density of electrons in the superconducting state, $\rho_s(T) \equiv 1/\lambda(T)^2$. Comparing $\rho_s(T)$ from samples across the phase diagram of a family of iron pnictide superconductors can shed light on the pairing mechanism [95] as well as on the relation between superconductivity and adjacent phases [122]. The family of $\text{Ba}(\text{Fe}_{1-x}\text{Co}_x)_2\text{As}_2$ is a good candidate for such studies because single crystals can be grown cleanly with relatively sharp superconducting transitions [91, 92], because the magnetic and structural transitions are well characterized [123–125], and because other careful studies of quasi-particle excitation measurements such as thermal conductivity [126, 127] and Raman scattering [128] have been successfully performed across the phase diagram.

λ is difficult to measure accurately. In the pnictides, the proximity of the magnetic phase to superconductivity on the underdoped (UD) side of the superconducting dome prevents measurement of λ by μSR [129]. Bulk measurements by microwave- and RF-based techniques are made difficult by complex sample topography and inhomogeneity, which can explain the significantly different results among nominally similar samples of both $\Delta\lambda \equiv \lambda(T) - \lambda(0)$ [101, 103, 106–108] and λ [72] measurements. Local-probe studies of $\rho_s(T)$ across the doping range are strongly desirable, because such measurements can obtain λ even when the magnetic order is adjacent or co-existing [79], and can reduce the error from topography and inhomogeneity [73].

In this chapter, we report local measurements of $\lambda_{ab}(T)$, the penetration depth for screening currents flowing in the ab plane in a set of $\text{Ba}(\text{Fe}_{1-x}\text{Co}_x)_2\text{As}_2$ single crystals grown from self-flux [92]. We measure at Co composition x across the superconducting dome: underdoped (UD) $x = 0.045, 0.049, 0.051$; optimally doped (OptD) $x = 0.07$; and overdoped (OD) $x = 0.085, 0.11$ ¹. Our measurements average over a few microns. The positions we choose to measure show strong, uniform diamagnetic response, and are at least 15 microns away from topographic steps larger than 0.5 micron. We are

¹For UD samples, $\lambda_a \neq \lambda_b$, our measurements give $\lambda_{ab} \equiv \sqrt{\lambda_a \lambda_b}$

able to resolve well-formed vortices to rule out granularity on sub-micron scales except at $x = 4.5\%$. We observe systematic evolution of $\rho_s(T)$ with x . Our observations suggest strong correlation between magnetism and superconductivity.

6.2 Experiments: three observations

We determine $\lambda_{ab}(T)$ from 5 K to T_c by MFM within 15% error, mostly from uncertainty in the MFM tip geometry. We use the same MFM tip at $x = 4.5\%$, 7% and 11%, reducing the relative error of $\lambda_{ab}(T)$ among these samples. $\Delta\lambda_{ab}(T)$ by both techniques has 7% error, mostly from calibration uncertainty of the scanner. At most x , we measure at least two samples from the same growth batch, one by MFM and one by SSS. When $\Delta\lambda_{ab}(T)$ measured by both the techniques overlaps in the common temperature range, we offset $\Delta\lambda_{ab}(T)$ from SSS by $\lambda_{ab}(T = 5\text{K})$ from MFM, and obtain $\rho_s(T) \equiv 1/\lambda_{ab}(T)^2$ over the full temperature range, as shown in Fig. 6.1. However, $\Delta\lambda_{ab}(T)$ measured by the two techniques do not agree at $x = 4.9\%$, presumably due to sample variations. At $x = 11\%$, we observe different $\Delta\lambda_{ab}(T)$ by SSS at three locations separated by hundreds of microns (shown in Fig. 6.4), one of which matches the MFM measurement.

We observe a systematic change of $\rho_s(T)$ with Co doping x across the superconducting dome that can be characterized by three trends. First, the zero temperature value $\rho_s(0)$ (Fig. 6.2) peaks at OptD. It is strongly reduced in the UD regime, falling sharply as the magnetic order onsets. For UD samples, $\rho_s(0)$ falls more quickly than T_c , while on the OD side, $\rho_s(0)$ falls less rapidly than T_c . This observation is different from a previous measurement by bulk technique that reported $\rho_s(0)$ increasing with doping across the doping dome [72].

Second, the magnitude of $\Delta\lambda_{ab}(T)$ [Fig. 6.1c] at low T increases away from OptD on both sides of the dome. At $x = 7\%$, $\Delta\lambda_{ab}(T)$ remains flat within 0.5 nm below 3 K, indicating fully gapped superconductivity, consistent with the proposed order parameter s_{\pm} [95]. We use a phenomenological single-gap fit to $\rho_s(T)$ at $x = 7\%$,

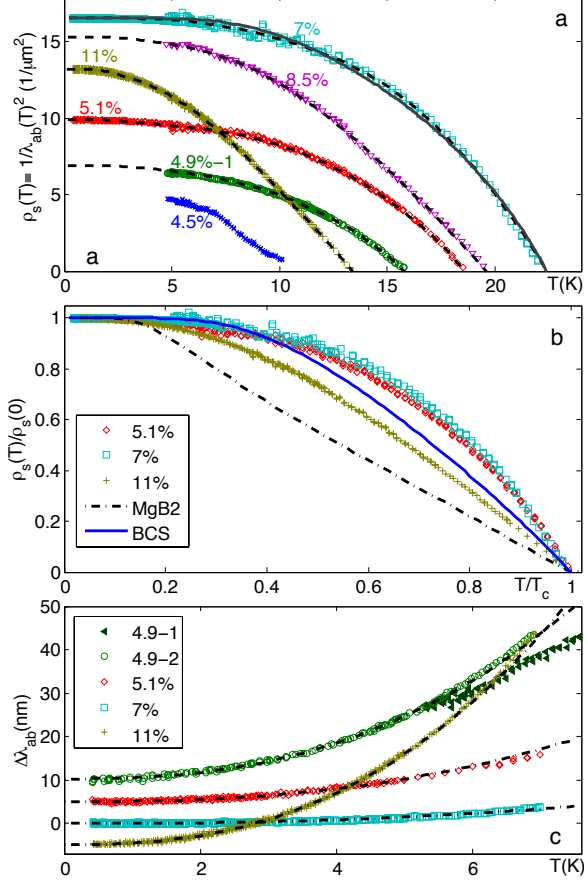


Figure 6.1: The temperature dependence of $\rho_s(T) \equiv 1/\lambda_{ab}(T)^2$ and $\Delta\lambda_{ab}(T)$ shows three systematic trends. **a:** $\rho_s(T)$ vs T . Solid line: a single-gap equation (Eq. 1) fits only $x = 7\%$. Dashed lines: phenomenological two-gap fits (Eq. 2) work well at every doping. Fit parameters in Table. 6.1). At $x = 8.5\%$, we did not measure $\lambda_{ab}(T)$, so we offset $\Delta\lambda_{ab}(T)$ by the mean of $\lambda_{ab}(0)$ at $x = 7\%$ and $x = 11\%$. **b:** $\rho_s(T)/\rho_s(0)$ vs T/T_c . At $x = 5.1\%$ (UD) and $x = 7\%$ (OptD), $\rho_s(T)$ rises more sharply than for MgB₂ from Ref. [130], single-band weakly coupled BCS theory, or $x = 11\%$ (OD). **c:** $\Delta\lambda_{ab}(T)$ down to 0.4 K measured by SSS at the indicated x . Dashed lines: power-law fits (Eq. 3) describe the data well up to $0.3T_c$ with the power n fixed at 2.5 (fit parameters in Table. 6.1). The amplitude A increases away from optimal doping, where $\Delta\lambda_{ab}(T)$ is so flat as to be consistent with exponential behavior. Successive data sets are offset vertically by 5 nm for clarity. $\Delta\lambda_{ab}(T)$ at $x = 4.9\%$ measured on a different sample by MFM at $T > 5$ K is also plotted.

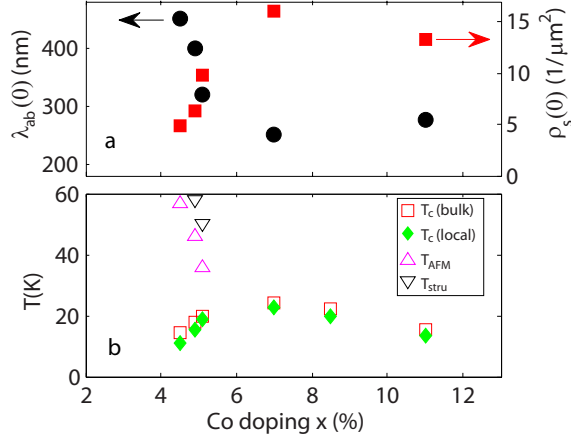


Figure 6.2: **a:** $\lambda_{ab}(0)$ and $\rho_s(0)$ as extrapolated from Fig 6.1(a), showing the rapid drop of $\rho_s(0)$ on the underdoped side. For $x = 4.5\%$, $\rho_s(5K)$ is plotted because the extrapolation is unclear. **b:** Temperatures of structural, magnetic and superconducting transitions T_{stru} , T_{AFM} and $T_c(\text{bulk})$, from resistivity measurements of samples from the same growth as studied here. $T_c(\text{local})$ is from linear extrapolation of $\rho_s(T)$ to zero from the MFM data presented here.

with the gap function [68]

$$\Delta(T) = \Delta(0) \tanh \left(\frac{\pi T_c}{\Delta(0)} \sqrt{a \left(\frac{T_c}{T} - 1 \right)} \right) \quad (6.1)$$

where a is a free parameter that characterizes the rise of $\rho_s(T)$ below T_c . This full single gap fit gives $\Delta(0) = 2.0k_B T_c$ and $a = 1.7$, and, as shown in figure 1a, adequately describes the measured temperature dependence for $x = 7\%$.

Due to the steeper $\Delta\lambda_{ab}(T)$ away from OptD, the full single gap fit does not work at other dopings. The low temperature variation can be described by a power law, but the full temperature dependence is also well described by a two-gap fit with one gap being small. In cases where the SSS and MFM data do not agree or where only one is available, only one of the fits is possible. We use a phenomenological two-gap fit:

$$\rho_s(T) = p\rho_1(T) + (1-p)\rho_2(T) \quad (6.2)$$

where ρ_1 , ρ_2 are given by Eq. 6.1 with gaps Δ_1 , Δ_2 . We fix T_c of the two gaps to

Table 6.1: Fit parameters for curves in Fig. 6.1 and 6.4, for the two-gap (Eq. 6.2) and power-law (Eq. 6.3) models. Power law fits are based on SSS data and two-gap fits on MFM or combined MFM and SSS data. Where both power-law and two-gap fits are shown, SSS and MFM data on different samples agreed. At $x = 4.9\%$, 5.1% and 7% , $\Delta\lambda_{ab}(T)$ at multiple positions separated by at least 100 microns are identical. For $x=11\%$, SSS results from 3 positions are shown. T_c measured on the same sample by MFM or SSS are also provided.

x	$T_c(K)$	full gap				A (nm/K ^{2.5})
		$\frac{\Delta_1}{k_B T_c}$	$\frac{\Delta_2}{k_B T_c}$	a	p	
4.9%-1	15.8	2.2	0.6	1.6	0.90	-
4.9%-2	15.5	-	-	-	-	0.26 (3 positions)
5.1%	18.6	2.3	0.7	1.6	0.90	0.09 (4 positions)
7%	22.4	3.3	1.3	1.7	0.70	0.02 (4 positions)
8.5%	19.6	1.9	0.6	1	0.92	-
11%	13.5	1.7	0.6	0.9	0.87	0.38 (position 1)
11%	-	-	-	-	-	0.27 (position 2)
11%	-	-	-	-	-	0.18 (position 3)

be identical and set a for the smaller gap to be 1 to minimize the number of free parameters. Best fit values are shown in Table 6.1. In the power law description,

$$\Delta\lambda_{ab}(T) = AT^n. \quad (6.3)$$

The best fit value of n varied from 2.3 to 2.9, but the error bars for all data sets are consistent with $n = 2.5$. We therefore fixed $n = 2.5$ for simplicity. As shown in Table 6.1, the fitted magnitude of A increases away from OptD.

The third trend we observe is that near T_c , $\rho_s(T)$ of the OptD and UD rises faster with decreasing temperature than weak-coupling BCS theory, MgB₂ or OD (Fig. 6.1b). This feature is characterized in the full-gap fits: a at $x = 5.1\%$ and 7% are significantly larger than the BCS value $a = 1$, suggesting a steeper rise of $\rho_s(T)$ with cooling than the weakly-coupled BCS would give. The same feature is shown in $\rho_s(T)/\rho_s(0)$ vs T/T_c plots when comparing with other superconductors. The curves at $x = 5.1\%$ (UD) and 7% (OptD) have similar slopes near T_c . Both are steeper than that of MgB₂, a weakly coupled two-gap BCS superconductor; or $x = 11\%$ (OD).

6.3 Spatial and sample variation in $\Delta\lambda$

Local probes allow us to measure at multiple positions on multiple samples and to examine real-space inhomogeneity. On all samples we measured with MFM, we obtain identical $\lambda_{ab}(T)$ and $\Delta\lambda_{ab}(T)$ within errors on positions several microns apart. On all samples studied with SSS, we measured three or four positions separated by hundreds of microns. For the $x = 4.9\%$, 5.1% , and 7% samples, the $\Delta\lambda_{ab}(T)$ measurements were identical within errors at each location. We observe different $\Delta\lambda_{ab}(T)$ on the two 4.9% samples. The one measured by MFM has a slope of $\Delta\lambda_{ab}(T)$ 30% less steep than that of the other sample by SSS (Fig. 6.3). The disagreement between the two techniques prevents us from obtaining $\rho_s(T)$ over the full T range at 4.9% precisely. Instead, we obtain a range of normalized superfluid density by taking into account the uncertainty of $\Delta\lambda_{ab}(T)$ at $T < 5$ K bounded by the MFM and SSS measurements. As shown in Fig. 6.3, the rise of $\rho_s(T)/\rho_s(0)$ with cooling near T_c is as steep as that of the 5.1% and 7% .

We observe spatial variation in $\Delta\lambda_{ab}(T)$ on one $x = 11\%$ sample as shown in Fig. 6.4, resulting in the variations in fit parameters shown in Table 6.1 and magnitude A also plotted in Fig. 6.3. In principle, such spatial variations could come from doping inhomogeneity in the sample, or from roughness of the sample surface, or from other variations. In order to quantify doping inhomogeneity in the sample, we performed x-ray microanalysis after the SSS measurement was complete. The $3 \mu\text{m}$ beam was scanned across a 1.2 mm long line in $20 \mu\text{m}$ steps. We observe no systematic change in the doping level to within $\pm 2\%$ of the total Co concentration. We do not think the spatial variation comes from sample surface roughness because we checked the topography by susceptometry scans in-situ and by optical microscopy after the measurement, and because roughness is expected to overestimate $\Delta\lambda$, while the three values are either smaller than or the same as the MFM result.

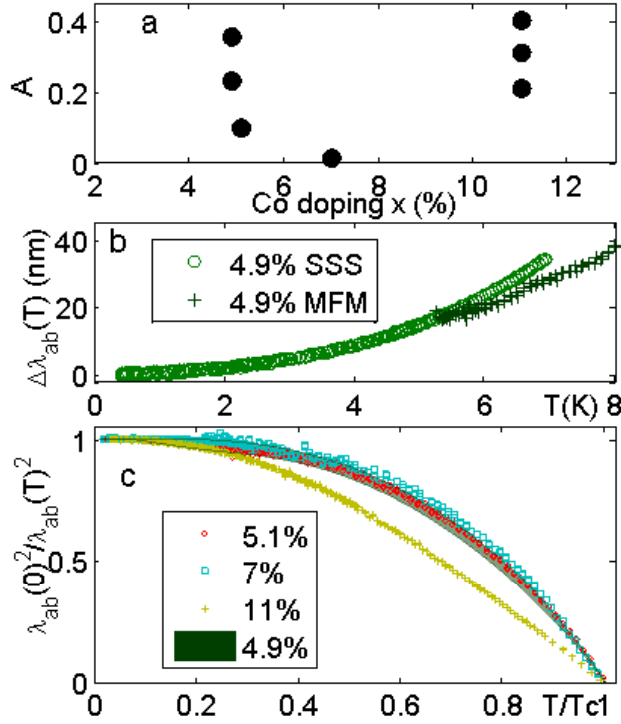


Figure 6.3: Sample and position variations of $\Delta\lambda_{ab}(T)$. **(a)** Magnitude A from power-law fit of $\Delta\lambda_{ab}(T)$ showing the doping dependence as well as the sample and position variations at $x = 4.9\%$ and $x = 11\%$. **(b)** $\Delta\lambda_{ab}(T)$ measured by SSS from 0.4 K to 7 K and by MFM on a sister sample from 5 K to T_c at $x = 4.9\%$. **(c)** $\rho_s(T)$ of $x = 4.9\%$ with uncertainty of $\rho_s(0)$ and T_c (shading region). $\rho_s(0)$ at $x = 5.1\%$, 7% and 11% are also plotted for comparison.

6.4 Discussion

The systematic trends that we have observed in $\rho_s(T)$ should be considered in light of properties in the superconducting states that are expected to evolve with doping, including the structure of the gap in k -space on multiple bands [128, 131], magnetic scattering, other forms of scattering [132], and transfer of spectral weight to spin fluctuations and the magnetic phase [133]. In particular, the three trends of $\rho_s(T)$ can be accounted for by the interplay between magnetism and superconductivity.

The first trend, $\rho_s(0)$ dropping more rapidly on moving towards UD than towards OD, follows naturally from the fact that the structural and magnetic transitions lead to significant Fermi surface reconstruction [131, 134], resulting in smaller electron and hole pockets and therefore fewer charge carriers for the superconducting state. In the UD cuprates, the reduction of $\rho_s(0)$ approximately following T_c [135] has been often attributed to phase fluctuations of the superconducting state [69]. We observed an even faster drop of $\rho_s(0)$ than T_c , consistent with the scenario that coexisting order, e.g. magnetic order, removes a large number of itinerant carriers that might otherwise enter the superconducting condensate.

The second trend, weakening of fully-gapped behavior away from OptD, agrees with heat transport measurements which have also reported an increase in low-energy quasi-particle excitation on either side of OptD [127]. The observation indicates strong pair-breaking scattering or anisotropic superconducting gap structure in the s_{\pm} pairing symmetry [112]. The Fermi surface reconstruction resulting from the magnetic order on the UD side is not expected to lead to nodes, but may result in deep minima in the gap structure [136, 137]. The increasing strength of the static order and low-frequency magnetic fluctuations on the UD side [124, 125] could enhance pair-breaking magnetic scattering [138], giving rise to a power law dependence in $\Delta\lambda_{ab}(T)$ [112] that gets sharper with less doping on the UD side. On the OD side, deep gap minima may result from an anisotropic reduction of pairing strength as the doping moves further from the static magnetic order. Although pair-breaking may play some role and is one possible explanation for the spatial variation in the 11% sample, two facts suggest that our results are not dominated by pair-breaking

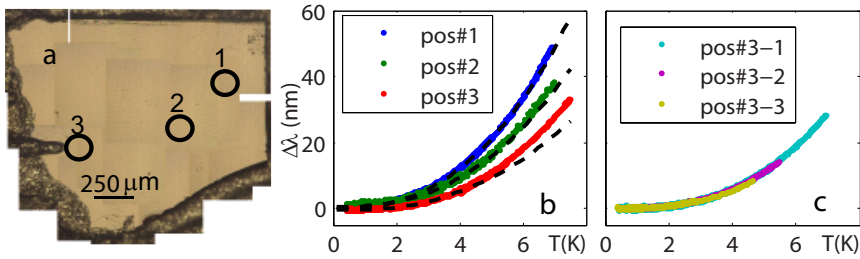


Figure 6.4: Inhomogeneity in $\Delta\lambda_{ab}(T)$ observed in an $x = 11\%$ sample. **a:** Photograph of the $x = 11\%$ sample measured by SSS. The label of positions corresponds to the position where $\Delta\lambda_{ab}(T)$ was measured. **b,c:** $\Delta\lambda_{ab}(T)$ by SSS at positions 1-3 (b) and three different positions around position 3 each separated by $15\mu\text{m}$ (c). Dashed lines in (b) plot power-law fits with parameters given in Table 6.1.

processes from sample imperfection: the doping dependence we report is consistent with the low energy excitations measurements on annealed crystals [139], and we observe flat $\Delta\lambda_{ab}(T)$ at OptD.

The third trend, the rapid increase $\rho_s(T)$ of the UD and OptD when cooling through T_c , also agrees with the importance of magnetism. If the pairing is mediated by spin-fluctuations [95], forming superconductivity pushes the fluctuation spectrum to higher frequency, which further strengthens pairing, leading to a more rapid rise of $\rho_s(T)$ than the standard BCS expression would give [138]. On the OD side, away from the magnetic order, the absence of low-frequency magnetic fluctuations may contribute to the slow rise of $\rho_s(T)$ when cooling through T_c . The slower rise at $x = 11\%$ than the weak-coupling BCS result may hint that the two gaps have different T_c 's.

To conclude, by locally measuring $\lambda_{ab}(T)$ and $\Delta\lambda_{ab}(T)$, we observe systematic doping evolution of both the zero temperature value and the temperature dependence of $\rho_s(T)$ in $\text{Ba}(\text{Fe}_{1-x}\text{Co}_x)_2\text{As}_2$ single crystals. Using local scanning techniques, we reduce the error from sample inhomogeneity. The three systematic trends we observe on $\rho_s(T)$ across the superconducting dome are consistent with the role of magnetism as a coexisting and competing order to the superconductivity as well as the pairing glue.

6.5 Speculations

6.5.1 $\rho_s(0)$ of cuprates and pnictides

The role of phase fluctuation in unconventional superconductors, which has been under heated discussion in the past two decades, can be investigated by the zero-temperature value of superfluid density $\rho_s(0)$. In the UD cuprates, Uemura and collaborators reported universal correlation between $\rho_s(0)$ and T_c [135], which was attributed to the importance of phase fluctuations in superconductors with small superfluid density [69]. The phase coherent temperature T_θ^{max} , the temperature at which phase order would disappear unless pairing order disappeared first, is proportional to $\rho_s(0)$. In most UD cuprates, $T_\theta^{\text{max}} \approx T_c$.

Table 6.2 contains $\rho_s(0)$ of $\text{Ba}(\text{Fe}_{1-x}\text{Co}_x)_2\text{As}_2$ reported in this chapter, of YBCO from Ref [6, 60, 140], and of La-124 from Ref [141]. $\rho_s(0)$ of $\text{Ba}(\text{Fe}_{1-x}\text{Co}_x)_2\text{As}_2$ is about 1.5 to 2 times as large as the value of $\rho_s(0)$ of UD cuprates with similar T_c . The data are also plotted in Fig. 6.5.

When we calculate T_θ^{max} , dimensionality of the superconducting state comes in.

$$T_\theta^{\text{max}} = A \frac{(\hbar c)^2 a}{16\pi e^2 \lambda(0)^2}$$

where both the dimensionless number A and the coherent length scale a depends on the anisotropy between the in-plane and c-axis superfluid density. In the 2D limit, $A = 0.9$ and a is the spacing between the superconducting layers. The 3D limit gives $A = 2.2$ and $a = \sqrt{\pi}\xi_c$, which leads to a much larger T_θ^{max} than the 2D limit even for the same $\rho_s(0)$, as shown in Fig. 6.5.

Using the 3D limit, we obtain T_θ^{max} for the pnictides more than 15 times of T_c in the underdoped regime, suggesting the phase fluctuation may not be as important in the pnictides as in the cuprates. However, $\rho_s(0)$ of the two materials with similar T_c are not very different; the phase fluctuation theory was qualitatively developed for quasi-two-dimensional materials, and may need extra caution to apply to more isotropic materials like the pnictides. Both facts make it intriguing to investigate more about the role of phase fluctuation in the pnictides both theoretically and experimentally.

Table 6.2: The in-plane $\rho_s(0)$ and T_c of $\text{Ba}(\text{Fe}_{1-x}\text{Co}_x)_2\text{As}_2$, $\text{YBa}_2\text{Cu}_3\text{O}_{6+x}$, and $\text{La}_{2-x}\text{Sr}_x\text{CuO}_4$. The compounds are in the underdoped region of the phase diagram unless labelled explicitly by ‘OptD’ for optimal doping and ‘OD’ for overdoping.

material	T_c (K)	$\rho_s(0)$ ($1/\mu\text{m}^2$)	Ref
YBCO	75	53	[6]
	56	35	
YBCO	50	20	[140]
	17	5.4	
	14	4.1	
YBCO	12	3.0	[60]
	10	2.0	
	8	1.2	
La124	35.5	13.2	[141]
	32	8.9	
	22.2	7.1	
	14	3.8	
BaCo122	23 (OptD)	16.0	this work
	18.5	9.8	
	15.5	6.2	
	11	4.9	
	13.5 (OD)	13.2	

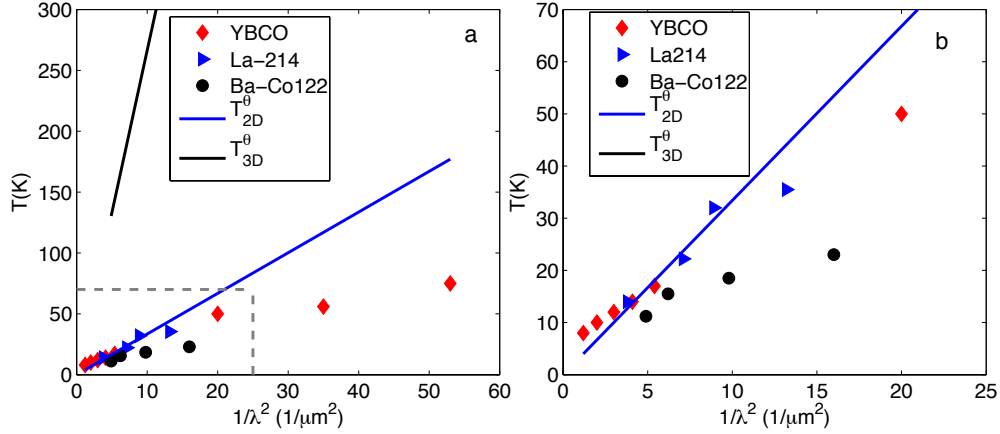


Figure 6.5: **a:** $\rho_s(0)$ vs. T_c of cuprates and pnictides from the data listed in Table 6.2, and the phase fluctuation temperature in 2D limit T_θ^{2D} using YBCO parameter $A = 0.9$ and $a = 0.59$ nm, and in 3D limit T_θ^{3D} using BaCo122 parameter $\xi_c = 1.1$ nm, $a = \sqrt{\pi}\xi_c$ and $A = 2.2$. **b:** the blow-up plot of a in the region marked by the dashed line.

6.5.2 Disparity of gap structures in the pnictides

The gap structure and order parameter symmetry of the iron-pnictide superconductors are still under debate after extensive studies in the recent few years. One of the intrinsic difficulties is the multi-band nature of the pnictides. If one band is fully gapped carrying 90% of the superconducting electrons, the second gap being nodal or nodeless will give similar behaviour in quasi-particle excitation measurements, making it difficult to distinguish the two situations. However, a more consistent understanding seems to be forming.

Table 6.3 summarizes some recent results from the leading groups on pnictide penetration depth measurements. In my opinion, behaviours consistent with full gap are commonly observed in most 122 and 1111 families. Although the low T $\Delta\lambda(T)$ in many measurements is consistent with a powerlaw, the small magnitude of $\Delta\lambda(T)$ reported by different groups can be attributed to pair-breaking scattering in the fully gapped $s\pm$ superconducting state. The small difference in $\Delta\lambda(T)$ magnitude among measurements is also consistent with possible difference in pair-breaking scattering among samples.

Pnictide with stronger superconductivity (e.g. higher T_c) are more likely to be found fully-gapped. This is the trend we report in this chapter by comparing compounds in the same family ($\text{Ba}(\text{Fe}_{1-x}\text{Co}_x)_2\text{As}_2$). It is also consistent with the fact that nodal pnictides very often have quite low T_c (e.g. LaFePO , KFe_2As_2). One possibility is that the anisotropic magnetic fluctuation leads to fully gapped $s\pm$ superconductivity in the pnictides. The reduction of the pairing strength may lead to modulation of the gap structure, or even accidental nodes. To test this hypothesis, it is crucial to accurately determine the gap size of each band in materials that appear fully gapped, and to determine the depth of the nodes in nodal pnictides both experimentally and theoretically.

Table 6.3: The up-to-date literature on penetration depth measurement taken on single-crystal pnictide superconductors. Some references in Table 5.1 were removed by newer results from the same group. ‘✓’ refers to the preferred explanation by the authors, ‘×’ for ruled out by the authors, ‘c’ for consistent with, and ‘-’ for no comments.

sample		$\frac{\rho_s(T)}{\rho_s(0)}$		$\Delta\lambda$		T_c (K)	group	Ref
		1 full gap	2 full gap	T nodal	T^2			
hline	SmFeAs(O,F)	×	✓	×	-	44	Bristol	[103]
1111	PrFeAsO _{1-y}	×	✓	×	-	35	Kyoto	[104]
P-base	LaFePO	×	×	✓	×	7	Bristol	[100]
	LaFePO	×	×	✓	×	7	Stanford	[97]
122	KFe ₂ As ₂	×	×	✓	×	4	Kyoto	[102]
	BaFe ₂ (As,P) ₂	×	×	✓	×	30	Kyoto	[101]
	(Ba,K)Fe ₂ As ₂	×	✓	×	-	> 25	Kyoto	[106]
	Ba(Fe,Co) ₂ As ₂	×	c	×	✓	22.5	Ames	[142]
	Ba(Fe,Co) ₂ As ₂	✓	✓	×	×	22.5	Stanford	
	Ba(Fe,Co) ₂ As ₂	×	✓	×	c	< 19 K	Stanford	

Bibliography

- [1] Y. Marin and C. C. Williams, *Appl. Phys. Lett.* **50**, 1455 (1987).
- [2] T. Albrecht, P. Grutter, D. Horne, and D. Rugar, *J. Appl. Phys.* **69**, 668 (1991).
- [3] J. R. Kirtley, *REPORTS ON PROGRESS IN PHYSICS* **73** (2010).
- [4] D. N. Basov, R. Liang, D. A. Bonn, W. N. Hardy, B. Dabrowski, M. Quijada, D. B. Tanner, J. P. Rice, D. M. Ginsberg, and T. Timusk, *Phys. Rev. Lett.* **74**, 598 (1995).
- [5] S. T. Johnson, E. M. Forgan, S. H. Lloyd, C. M. Aegerter, S. L. Lee, R. Cubitt, P. G. Kealey, C. Ager, S. Tajima, A. Rykov, et al., *Phys. Rev. Lett.* **82**, 2792 (1999).
- [6] T. Pereg-Barnea, P. J. Turner, R. Harris, G. K. Mullins, J. S. Bobowski, M. Raudsepp, R. Liang, D. A. Bonn, and W. N. Hardy, *Phys. Rev. B* **69**, 184513 (2004).
- [7] N. L. Wang, S. Tajima, A. I. Rykov, and K. Tomimoto, *Phys. Rev. B* **57**, R11081 (1998).
- [8] A. G. Sun, S. H. Han, A. S. Katz, D. A. Gajewski, M. B. Maple, and R. C. Dynes, *Phys. Rev. B* **52**, R15731 (1995).
- [9] V. K. Vlasko-Vlasov, U. Welp, G. W. Crabtree, D. Gunter, V. Kabanov, and V. I. Nikitenko, *Phys. Rev. B* **56**, 5622 (1997).
- [10] C. P. BEAN, *Rev. Mod. Phys.* **36**, 31 (1964).

- [11] U. H. Pi, Z. G. Khim, D. H. Kim, A. Schwarz, M. Liebmann, and R. Wiesendanger, *Appl. Phys. Lett.* **85**, 5307 (2004).
- [12] A. Chang, H. Hallen, L. Harriott, H. Hess, H. Kao, J. Kwo, R. Miller, R. Wolfe, and J. van der Zielb, *Appl. Phys. Lett.* **61**, 1974 (1992).
- [13] A. Wadas, O. Fritz, H. Hug, and H. Guntherodt, *Zeitschrift Fur Physik B-Condensed Matt.* **88**, 317 (1992).
- [14] J. Pearl, *J. Appl. Phys.* **37**, 4139 (1966).
- [15] B. D. Terris, J. E. Stern, D. Rugar, and H. J. Mamin, *Phys. Rev. Lett.* **63**, 2669 (1989).
- [16] G. Blatter, M. V. Feigel'man, V. B. Geshkenbein, A. I. Larkin, and V. M. Vinokur, *Rev. Mod. Phys.* **66**, 1125 (1994).
- [17] M. P. A. Fisher and D. H. Lee, *Phys. Rev. B* **39**, 2756 (1989).
- [18] D. R. Nelson and V. M. Vinokur, *Phys. Rev. B* **48**, 13060 (1993).
- [19] D. Ertascedil and M. Kardar, *Phys. Rev. Lett.* **73**, 1703 (1994).
- [20] J. P. Sethna, K. A. Dahmen, and C. R. Myers, *Nature* **410**, 242 (2001).
- [21] N. Avraham, B. Khaykovich, Y. Myasoedov, M. Rappaport, H. Shtrikman, D. E. Feldman, T. Tamegai, P. H. Kes, M. Li, M. Konczykowski, et al., *Nature* **411**, 451 (2001).
- [22] F. Pardo, F. de la Cruz, P. L. Gammel, E. Bucher, and D. J. Bishop, *Nature* **396** (1998).
- [23] J. E. Hoffman, K. McElroy, D.-H. Lee, K. M. Lang, H. Eisaki, S. Uchida, and J. C. Davis, *Science* **297**, 1148 (2002).
- [24] G. S. Park, C. E. Cunningham, B. Cabrera, and M. E. Huber, *Phys. Rev. Lett.* **68**, 1920 (1992).

- [25] M. Breitwisch and D. K. Finnemore, *Phys. Rev. B* **62**, 671 (2000).
- [26] B. W. Gardner, J. C. Wynn, D. A. Bonn, R. Liang, W. N. Hardy, J. R. Kirtley, V. G. Kogan, and K. A. Moler, *Applied Physics Letters* **80**, 1010 (????).
- [27] A. Moser, H. Hug, B. Stiefel, and H. Gntherodt, *J. Magn. Magn. Mater.* **190**, 114 (1998).
- [28] M. Roseman and P. Grütter, *Applied Surface Science* **188**, 416 (2002).
- [29] C. J. O. Reichhardt and M. B. Hastings, *Phys. Rev. Lett.* **92**, 157002 (2004).
- [30] M. Berciu, T. Rappoport, and J. Boldizsár, *Nature* **435**, 71 (2005).
- [31] C. Weeks, G. Rosenberg, B. Seradjeh, and M. Franz, *Nat. Phys.* **3**, 796 (2007).
- [32] R. Liang, D. Bonn, and W. Hardy, *Physica C* **304**, 105 (1998).
- [33] R. Liang, D. Bonn, and W. Hardy, *Physica C* **304**, 105 (1998).
- [34] R. Liang, D. A. Bonn, and W. N. Hardy, *Phys. Rev. B* **73**, 180505 (2006).
- [35] M. Willemin, C. Rossel, J. Hofer, H. Keller, A. Erb, and E. Walker, *Phys. Rev. B* **58**, R5940 (1998).
- [36] E. H. Brandt and G. P. Mikitik, *Phys. Rev. Lett.* **89**, 027002 (2002).
- [37] E. W. J. Straver, J. E. Hoffman, O. M. Auslaender, D. Rugar, and K. A. Moler, *Appl. Phys. Lett.* **93**, 172514 (2008).
- [38] M. Müller, D. A. Gorokhov, and G. Blatter, *Phys. Rev. B* **64**, 134523 (2001).
- [39] S. Senoussi, M. Osséna, G. Collin, and I. A. Campbell, *Phys. Rev. B* **37**, 9792 (1988).
- [40] E. H. Brandt, *Phys. Rev. Lett.* **69**, 1105 (1992).
- [41] B. L. I., *Europhys. Lett.* **8**, 673 (1989).

- [42] T. Nishizaki, K. Shibata, M. Maki, and N. Kobayashi, *J. Low Temp. Phys.* **131**, 931 (2003).
- [43] R. Liang, D. A. Bonn, W. N. Hardy, J. C. Wynn, K. A. Moler, L. Lu, S. Larochelle, L. Zhou, M. Greven, L. Lurio, et al., *Physica C* **383**, 1 (2002).
- [44] J. E. Sonier, R. F. Kiefl, J. H. Brewer, D. A. Bonn, S. R. Dunsiger, W. N. Hardy, R. Liang, R. I. Miller, D. R. Noakes, and C. E. Stronach, *Phys. Rev. B* **59**, R729 (1999).
- [45] J. R. Clem, *Phys. Rev. B* **43**, 7837 (1991).
- [46] S. N. Artemenko and A. N. Kruglov, *Phys. Lett. A* **143**, 485 (1990).
- [47] J. R. Clem, *J. Supercond.* **17**, 613 (2004).
- [48] L. N. Bulaevskii, M. Ledvij, and V. G. Kogan, *Phys. Rev. B* **46**, 11807 (1992).
- [49] J. Figueras, T. Puig, X. Obradors, W. K. Kwok, L. Paulius, G. W. Crabtree, and G. Deutscher, *Nat. Phys.* **2**, 402 (2006).
- [50] B. Khaykovich, D. T. Fuchs, K. Teitelbaum, Y. Myasoedov, E. Zeldov, T. Tamegai, S. Ooi, M. Konczykowski, R. A. Doyle, and S. F. W. R. Rycroft, *Phys. Rev. B* **61**, R9261 (2000).
- [51] M. Benkraouda and J. R. Clem, *Phys. Rev. B* **53**, 438 (1996).
- [52] J. W. Guikema, H. Bluhm, D. A. Bonn, R. Liang, W. N. Hardy, and K. A. Moler, *Phys. Rev. B* **77**, 104515 (2008).
- [53] M. Beleggia, G. Pozzi, A. Tonomura, H. Kasai, T. Matsuda, K. Harada, T. Akashi, T. Masui, and S. Tajima, *Phys. Rev. B* **70**, 184518 (2004).
- [54] A. N. Grigorenko, S. J. Bending, A. E. Koshelev, J. R. Clem, T. Tamegai, and S. Ooi, *Phys. Rev. Lett.* **89**, 217003 (2002).
- [55] V. K. Vlasko-Vlasov, A. Koshelev, U. Welp, G. W. Crabtree, and K. Kadowaki, *Phys. Rev. B* **66**, 014523 (2002).

- [56] A. Moser, H. Hug, B. Stiefel, and H. Guntherodt, *J. Magn. Magn. Matt.* **190**, 114 (1998).
- [57] O. M. Auslaender, L. Luan, E. W. J. Straver, J. E. Hoffman, N. C. Koshnick, E. Zeldov, D. A. Bonn, R. Liang, W. N. Hardy, and K. A. Moler, *Nat. Phys.* **5**, 35 (2009).
- [58] T. Schneider, *Physica B: Condensed Matter* **326**, 289 (2003).
- [59] A. Hosseini, D. M. Broun, D. E. Sheehy, T. P. Davis, M. Franz, W. N. Hardy, R. Liang, and D. A. Bonn, *Phys. Rev. Lett.* **93**, 107003 (2004).
- [60] D. M. Broun, W. A. Huttema, P. J. Turner, S. Ozcan, B. Morgan, R. Liang, W. N. Hardy, and D. A. Bonn, *Phys. Rev. Lett.* **99**, 237003 (2007).
- [61] R. Liang, D. A. Bonn, W. N. Hardy, and D. Broun, *Phys. Rev. Lett.* **94**, 117001 (2005).
- [62] J. Sader, J. Chon, and P. Mulvaney, *Rev. Sci. Instrum.* **70**, 3967 (1999).
- [63] J. R. Clem, *Physica C* **235**, 2607 (1994).
- [64] D. R. Nelson and V. M. Vinokur, *Phys. Rev. B* **48**, 13060 (1993).
- [65] D. R. Nelson, *Phys. Rev. Lett.* **60**, 1973 (1988).
- [66] M. Tinkham, *Introduction to Superconductivity* (McGraw-Hill, 1975).
- [67] W. Hardy, D. Bonn, D. Morgan, R. Liang, and K. Zhang, *Phys. Rev. Lett.* **70**, 3999 (1993).
- [68] R. Prozorov and R. W. Giannetta, *Supercond. Sci. and Technol.* **19**, R41 (2006).
- [69] V. J. Emery and S. A. Kivelson, *Nature* **374**, 434 (1995).
- [70] J. E. Sonier, J. H. Brewer, and R. F. Kiefl, *Rev. Mod. Phys.* **72**, 769 (2000).

- [71] J. E. Sonier, W. Huang, C. V. Kaiser, C. Cochran, V. Pacradouni, S. A. Sabok-Sayr, M. D. Lumsden, B. C. Sales, M. A. McGuire, A. S. Sefat, et al., arxiv 1010.6046 (2010).
- [72] R. T. Gordon, H. Kim, N. Salovich, R. W. Giannetta, R. M. Fernandes, V. G. Kogan, T. Prozorov, S. L. Bud'ko, P. C. Canfield, M. A. Tanatar, et al., Phys. Rev. B **82**, 054507 (2010).
- [73] C. W. Hicks, T. M. Lippman, M. E. Huber, J. G. Analytis, J. Chu, A. S. Erickson, I. R. Fisher, and K. A. Moler, Phys. Rev. Lett. **103**, 127003 (2009).
- [74] M. Roseman and P. Grütter, New Journal of Physics **3**, 24 (2001).
- [75] E. Nazaretski, J. P. Thibodaux, I. Vekhter, L. Civale, J. D. Thompson, and R. Movshovich, Appl. Phys. Lett. **95**, 262502 (2009).
- [76] J. E. Sonier, J. H. Brewer, R. F. Kiefl, D. A. Bonn, S. R. Dunsiger, W. N. Hardy, R. Liang, W. A. MacFarlane, R. I. Miller, T. M. Riseman, et al., Phys. Rev. Lett. **79**, 2875 (1997).
- [77] C. C. Homes, D. A. Bonn, R. Liang, W. N. Hardy, D. N. Basov, T. Timusk, and B. P. Clayman, Phys. Rev. B **60**, 9782 (1999).
- [78] J. H. Xu, J. H. Miller, and C. S. Ting, Phys. Rev. B **51**, 424 (1995).
- [79] L. Luan, O. M. Auslaender, T. M. Lippman, C. W. Hicks, B. Kalisky, J.-H. Chu, J. G. Analytis, I. R. Fisher, J. R. Kirtley, and K. A. Moler, Phys. Rev. B **81**, 100501 (2010).
- [80] M. Efron and R. Tibshirani, *An introduction to the bootstrap* (CRC Press, 1975).
- [81] V. G. Kogan, Phys. Rev. B **68**, 104511 (2003).
- [82] V. G. Kogan, A. Y. Simonov, and M. Ledvij, Phys. Rev. B **48**, 392 (1993).
- [83] Y. Kamihara, T. Watanabe, M. Hirano, and H. Hosono, JACS **130**, 3296 (2008).
- [84] J. Paglione and R. L. Greene, Nat Phys **6**, 645 (2010).

- [85] D. Singh, *Physica C: Superconductivity* **469**, 418 (2009).
- [86] H. Ding, P. Richard, K. Nakayama, K. Sugawara, T. Arakane, Y. Sekiba, A. Takayama, S. Souma, T. Sato, T. Takahashi, et al., *Europhys. Lett.* **83**, 47001 (2008).
- [87] D. H. Lu, M. Yi, S. Mo, A. S. Erickson, J. Analytis, J. Chu, D. J. Singh, Z. Hussain, T. H. Geballe, I. R. Fisher, et al., *Nature* **455**, 81 (2008).
- [88] T. Kondo, A. F. Santander-Syro, O. Copie, C. Liu, M. E. Tillman, E. D. Mun, J. Schmalian, S. L. Bud'ko, M. A. Tanatar, P. C. Canfield, et al., *Phys. Rev. Lett.* **101**, 147003 (2008).
- [89] H. Shishido, A. F. Bangura, A. I. Coldea, S. Tonegawa, K. Hashimoto, S. Kasahara, P. M. C. Rourke, H. Ikeda, T. Terashima, R. Settai, et al., *Phys. Rev. Lett.* **104**, 057008 (2010).
- [90] M. Rotter, M. Pangerl, M. Tegel, and D. Johrendt, *Angewandte Chemie International Edition* **47**, 7949 (2008).
- [91] N. Ni, M. E. Tillman, J. Yan, A. Kracher, S. T. Hannahs, S. L. Bud'ko, and P. C. Canfield, *Phys. Rev. B* **78**, 214515 (2008).
- [92] Jiun-Haw Chu, J. G. Analytis, C. Kucharczyk, and I. R. Fisher, *Phys. Rev. B* **79**, 014506 (2009).
- [93] S. Jiang, H. Xing, G. Xuan, C. Wang, Z. Ren, C. Feng, J. Dai, Z. Xu, and G. Cao, *J. of Phys.: Cond. Matt.* **21**, 382203 (2009).
- [94] H. Luetkens, H. Klauss, M. Kraken, F. J. Litterst, T. Dellmann, R. Klingeler, C. Hess, R. Khasanov, A. Amato, C. Baines, et al., *Nat Mater* **8**, 305 (2009).
- [95] I. I. Mazin, D. J. Singh, M. D. Johannes, and M. H. Du, *Phys. Rev. Lett.* **101**, 057003 (2008).
- [96] I. Mazin and J. Schmalian, *Physica C: Superconductivity* **469**, 614 (2009).

- [97] C. W. Hicks, T. M. Lippman, M. E. Huber, Z. Ren, J. Yang, Z. Zhao, and K. A. Moler, *J. Phys. Soc. Jpn* **78**, 013708 (2009).
- [98] C. Chen, C. C. Tsuei, M. B. Ketchen, Z. Ren, and Z. X. Zhao, *Nat Phys* **6**, 260 (2010).
- [99] J. Annett, N. Goldenfeld, and S. R. Renn, *Phys. Rev. B* **43**, 2778 (1991).
- [100] J. D. Fletcher, A. Serafin, L. Malone, J. G. Analytis, J. Chu, A. S. Erickson, I. R. Fisher, and A. Carrington, *Phys. Rev. Lett.* **102**, 147001 (2009).
- [101] K. Hashimoto, M. Yamashita, S. Kasahara, Y. Senshu, N. Nakata, S. Tonegawa, K. Ikada, A. Serafin, A. Carrington, T. Terashima, et al., *Phys. Rev. B* **81**, 220501 (2010).
- [102] K. Hashimoto, A. Serafin, S. Tonegawa, R. Katsumata, R. Okazaki, T. Saito, H. Fukazawa, Y. Kohori, K. Kihou, C. H. Lee, et al., *Phys. Rev. B* **82**, 014526 (2010).
- [103] L. Malone, J. D. Fletcher, A. Serafin, A. Carrington, N. D. Zhigadlo, Z. Bukowski, S. Katrych, and J. Karpinski, *Phys. Rev. B* **79**, 140501 (2009).
- [104] K. Hashimoto, T. Shibauchi, T. Kato, K. Ikada, R. Okazaki, H. Shishido, M. Ishikado, H. Kito, A. Iyo, H. Eisaki, et al., *Phys. Rev. Lett.* **102**, 017002 (2009).
- [105] C. Martin, M. E. Tillman, H. Kim, M. A. Tanatar, S. K. Kim, A. Kreyssig, R. T. Gordon, M. D. Vannette, S. Nandi, V. G. Kogan, et al., *Phys. Rev. Lett.* **102**, 247002 (2009).
- [106] K. Hashimoto, T. Shibauchi, S. Kasahara, K. Ikada, S. Tonegawa, T. Kato, R. Okazaki, C. J. van der Beek, M. Konczykowski, H. Takeya, et al., *Phys. Rev. Lett.* **102**, 207001 (2009).
- [107] C. Martin, R. T. Gordon, M. A. Tanatar, H. Kim, N. Ni, S. L. Bud'ko, P. C. Canfield, H. Luo, H. H. Wen, Z. Wang, et al., *Phys. Rev. B* **80**, 020501 (2009).

- [108] R. T. Gordon, C. Martin, H. Kim, N. Ni, M. A. Tanatar, J. Schmalian, I. I. Mazin, S. L. Bud'ko, P. C. Canfield, and R. Prozorov, *Phys. Rev. B* **79**, 100506 (2009).
- [109] S. Graser, T. A. Maier, P. J. Hirschfeld, and D. J. Scalapino, *New J. of Phys.* **11**, 025016 (2009).
- [110] K. Kuroki, H. Usui, S. Onari, R. Arita, and H. Aoki, *Phys. Rev. B* **79**, 224511 (2009).
- [111] V. Mishra, G. Boyd, S. Graser, T. Maier, P. J. Hirschfeld, and D. J. Scalapino, *Phys. Rev. B* **79**, 094512 (2009).
- [112] A. B. Vorontsov, M. G. Vavilov, and A. V. Chubukov, *Phys. Rev. B* **79**, 140507 (2009).
- [113] F. Tafuri, J. R. Kirtley, P. G. Medaglia, P. Orgiani, and G. Balestrino, *Phys. Rev. Lett.* **92**, 157006 (2004).
- [114] K. Seo, B. A. Bernevig, and J. Hu, *Phys. Rev. Lett.* **101**, 206404 (2008).
- [115] R. H. Liu, T. Wu, G. Wu, H. Chen, X. F. Wang, Y. L. Xie, J. J. Ying, Y. J. Yan, Q. J. Li, B. C. Shi, et al., *Nature* **459**, 64 (2009).
- [116] V. Stanev, J. Kang, and Z. Tesanovic, *Phys. Rev. B* **78**, 184509 (2008).
- [117] G. Li, W. Z. Hu, J. Dong, Z. Li, P. Zheng, G. F. Chen, J. L. Luo, and N. L. Wang, *Phys. Rev. Lett.* **101**, 107004 (2008).
- [118] M. M. Parish, J. Hu, and B. A. Bernevig, *Phys. Rev. B* **78**, 144514 (2008).
- [119] B. Kalisky, J. R. Kirtley, J. G. Analytis, J.-H. Chu, A. Vailionis, I. R. Fisher, and K. A. Moler, *Phys. Rev. B* **81**, 184513 (2010).
- [120] M. A. Tanatar, N. Ni, C. Martin, R. T. Gordon, H. Kim, V. G. Kogan, G. D. Samolyuk, S. L. Bud'ko, P. C. Canfield, and R. Prozorov, *Phys. Rev. B* **79**, 094507 (2009).

- [121] T. J. Williams, A. A. Aczel, E. Baggio-Saitovitch, S. L. Budko, P. C. Canfield, J. P. Carlo, T. Goko, J. Munevar, N. Ni, Y. J. Uemura, et al., *Phys. Rev. B* **80**, 094501 (2009).
- [122] A. B. Vorontsov, M. G. Vavilov, and A. V. Chubukov, *Phys. Rev. B* **79**, 060508 (2009).
- [123] S. Nandi, M. G. Kim, A. Kreyssig, R. M. Fernandes, D. K. Pratt, A. Thaler, N. Ni, S. L. Bud'ko, P. C. Canfield, J. Schmalian, et al., *Phys. Rev. Lett.* **104**, 057006 (2010).
- [124] C. Lester, J.-H. Chu, J. G. Analytis, S. C. Capelli, A. S. Erickson, C. L. Condron, M. F. Toney, I. R. Fisher, and S. M. Hayden, *Phys. Rev. B* **79**, 144523 (2009).
- [125] D. K. Pratt, W. Tian, A. Kreyssig, J. L. Zarestky, S. Nandi, N. Ni, S. L. Bud'ko, P. C. Canfield, A. I. Goldman, and R. J. McQueeney, *Phys. Rev. Lett.* **103**, 087001 (2009).
- [126] M. A. Tanatar, J.-P. Reid, H. Shakeripour, X. G. Luo, N. Doiron-Leyraud, N. Ni, S. L. Bud'ko, P. C. Canfield, R. Prozorov, and L. Taillefer, *Phys. Rev. Lett.* **104**, 067002 (2010).
- [127] J.-P. Reid, M. A. Tanatar, X. G. Luo, H. Shakeripour, N. Doiron-Leyraud, N. Ni, S. L. Bud'ko, P. C. Canfield, R. Prozorov, and L. Taillefer, *Phys. Rev. B* **82**, 064501 (2010).
- [128] B. Muschler, W. Prestel, R. Hackl, T. P. Devereaux, J. G. Analytis, J.-H. Chu, and I. R. Fisher, *Phys. Rev. B* **80**, 180510 (2009).
- [129] T. J. Williams, A. A. Aczel, E. Baggio-Saitovitch, S. L. Bud'ko, P. C. Canfield, J. P. Carlo, T. Goko, H. Kageyama, A. Kitada, J. Munevar, et al., *Phys. Rev. B* **82**, 094512 (2010).
- [130] J. D. Fletcher, A. Carrington, O. J. Taylor, S. M. Kazakov, and J. Karpinski, *Phys. Rev. Lett.* **95**, 097005 (2005).

- [131] C. Liu, T. Kondo, R. M. Fernandes, A. D. Palczewski, E. D. Mun, N. Ni, A. N. Thaler, A. Bostwick, E. Rotenberg, J. Schmalian, et al., *Nat. Phys.* **6**, 419 (2010).
- [132] R. T. Gordon, H. Kim, M. A. Tanatar, R. Prozorov, and V. G. Kogan, *Phys. Rev. B* **81**, 180501 (2010).
- [133] D. S. Inosov, J. T. Park, P. Bourges, D. L. Sun, Y. Sidis, A. Schneidewind, K. Hradil, D. Haug, C. T. Lin, B. Keimer, et al., *Nat. Phys.* **6**, 178 (2010).
- [134] J. G. Analytis, R. D. McDonald, J.-H. Chu, S. C. Riggs, A. F. Bangura, C. Kucharczyk, M. Johannes, and I. R. Fisher, *Phys. Rev. B* **80**, 064507 (2009).
- [135] Y. J. Uemura, G. M. Luke, B. J. Sternlieb, J. H. Brewer, J. F. Carolan, W. N. Hardy, R. Kadono, J. R. Kempton, R. F. Kiefl, S. R. Kreitzman, et al., *Phys. Rev. Lett.* **62**, 2317 (1989).
- [136] D. Parker, M. G. Vavilov, A. V. Chubukov, and I. I. Mazin, *Phys. Rev. B* **80**, 100508 (2009).
- [137] P. Ghaemi and A. Vishwanath, arXiv.1002.4638v2 (2010).
- [138] P. Monthoux and D. J. Scalapino, *Phys. Rev. B* **50**, 10339 (1994).
- [139] K. Gofryk, V. A. B., V. I., A. S. Sefat, I. T., B. E. D., J. D. Thompson, and F. Ronning, arXiv.1009.1091 (2010).
- [140] J. E. Sonier, S. A. Sabok-Sayr, F. D. Callaghan, C. V. Kaiser, V. Pacradouni, J. H. Brewer, S. L. Stubbs, W. N. Hardy, D. A. Bonn, R. Liang, et al., *Phys. Rev. B* **76**, 134518 (2007).
- [141] J. L. Tallon, J. W. Loram, J. R. Cooper, C. Panagopoulos, and C. Bernhard, *Phys. Rev. B* **68**, 180501 (2003).
- [142] H. Kim, R. T. Gordon, M. A. Tanatar, J. Hua, U. Welp, W. K. Kwok, N. Ni, S. L. Bud'ko, P. C. Canfield, A. B. Vorontsov, et al., *Phys. Rev. B* **82**, 060518 (2010).